© 2016 by Yanbin Wu. All rights reserved.

DEVELOPING FORCE FIELD PARAMETERS FOR WATER INTERACTING WITH GRAPHENE AND GRAPHENE-LIKE MATERIALS

BY

YANBIN WU

DISSERTATION

Submitted in partial fulfillment of the requirements
for the degree of Doctor of Philosophy in Mechanical Engineering
in the Graduate College of the
University of Illinois at Urbana-Champaign, 2016

Urbana, Illinois

Doctoral Committee:

Professor Narayana R. Aluru, Chair
Professor David Ceperley
Assistant Professor Lucas K. Wagner
Assistant Professor Sungwoo Nam

Abstract

Confined water can have properties dramatically different from bulk water, and these properties can be used to develop unique functionality at the nanoscale. For example, fast water transport, rotation-translation coupling, and fast rotational motion have been observed in graphitic carbon-based nano structures, which enables various applications like energy storage and seawater desalination. The explosive studies on graphene have sparked new interests towards graphene-analogous materials including hexagonal boron nitride (hBN) and molybdenum disulfide (MoS_2). Compared to graphene, the graphene-analogous materials possess non-zero bandgap, chemical inertness, and biological compatibility. The graphene-analogous materials are promising materials, complementary to graphene, for high-temperature, biomedical and nanofluidic applications. We would like to understand and optimize graphene and graphene-analogous materials in these applications.

The study of graphene and graphene-analogous materials at the atomic level requires accurate force field parameters to describe the water-surface interaction. We begin with benchmark quality first principles quantum Monte Carlo (QMC) calculations on the interaction energy between water and surface, which are used to validate random phase approximation (RPA) calculations. We then proceed with RPA to derive force field parameters, which are used to simulate properties like water contact angle on the surface, attaining a value within the experimental uncertainties. This work demonstrates that end-to-end multiscale modeling, starting at detailed many-body quantum mechanics, and ending with macroscopic properties, with the approximations controlled along the way, is feasible for these systems.

To Father and Mother, and Mozi.

Acknowledgments

This work would not have been possible without the support of many people. Many thanks to my adviser, Dr. Narayana R. Aluru, who provided guidance and financial support throughout this endeavor with great patience. I would also like to thank Lucas K. Wagner, who treated me as if I were his own student and worked with me on papers, slides, and this dissertation. I owe a great debt to Dr. David Ceperley for teaching me the quantum Monte Carlo method, which is the base of my work, back in 2014 during summer school. Thanks to Dr. Sungwoo Nam, who taught me the insights from an experimentalist point of view during our collaborations. I deeply appreciate Dr. Yuhang Jing, who is always the first person I go to for a brain-storming whenever I encountere questions in my research. Thanks to Dr. Xiaobing Mi, Dr. Xiaozhong Jin, Dr. Joseph Sony, and Dr. Chang Won, for being my mentors during the early years when I started this endeavor. And finally, thanks to my wife, parents, and numerous friends who endured this long process with me, always offering support and love.

Table of Contents

List of Tables

List of Figures

List of Abbreviations

QMC	Quantum Monte Carlo
DMC	Diffusion Monte Carlo
RPA	Random Phase Approximations
CCSD(T)	Coupled Cluster calculations with Single and Double excitations and perturbative Triples
CBS	Complete Basis Set
MP2	Second-order Møller-Plesset perturbation theory
DFT	Density Functional Theory
DFT-D	Density Functional Theory with Dispersion correction
RBM	Radial Breathing Mode
aVDZ	aug-cc-pVDZ
aVTZ	aug-cc-pVTZ
aVQZ	aug-cc-pVQZ
MD	Molecular Dynamics
CNT	Carbon NanoTube
hBN	hexagonal boron nitride
MoS_2	Molybdenum disulfide

List of Symbols

ε, σ	Force field parameters for Lennard-Jones interatomic potential
$\hat{H}$	Hamiltonian operator
Ψ	Wave function of time-dependent Schrödinger equation
ψ_n	Eigen function of time-independent Schrödinger equation
ψ_0	Ground state wave function of time-independent Schrödinger equation
E_0	Ground state energy of time-independent Schrödinger equation
θ	Contact angle
Δf_{RBM}	The frequency shift in radial breathing mode of carbon nanotube

Chapter 1

Introduction

1.1 Graphene and Graphene-like Materials

Graphene is a two-dimensional material composed of carbon atoms. In graphene, each carbon atom has a sp2 hybridization and forms three sigma bonds and one pi bond with the neighboring atoms, as shown in Fig. 1.1(b). Graphene is one-atom thick, stronger than steel, harder than diamond, and excellent in conducting heat and electricity. It is such a promising material that its discoverers were awarded the Nobel prize in physics.

Graphene can also be considered as a building block for structures of other dimensions. We can stack graphene to form three-dimensional graphite, shown in Fig. 1.1(d), and roll it into one-dimensional carbon nanotube (CNT), shown in Fig. 1.1(e), or 0-dimensional bucky ball shown in Fig. 1.1(f).

The explosive studies on graphitic carbon based structure have sparked new interests towards materials structurally similar to graphene, e.g., hexagonal boron nitride (hBN) and molybdenum disulfide (MoS_2). Compared to graphene, hBN replaces carbon-carbon bond with boron-nitrogen bond. hBN is also one-atom thick. MoS_2 is composed of the transition metal molybdenum with an atomic number of 46, and sulfur. The top view of MoS_2 is hexagonal like graphene. Yet from side view, the Mo atoms and the S atoms are not on the same plane: The Mo atoms are sandwiched by two layers of S atoms.

In this study, we are interested in confined water by these novel materials at the nanoscale.

1.2 Confined Water by Graphene/Graphene-like Materials

We are interested in confined water because confined water can have properties dramatically different from bulk water. For example, fast water transport [23, 24], rotation-translation coupling [25], and fast rotational motion [26, 27] have been observed in graphitic carbon-based nano structures. Graphene-confined water has unique responses to local electric field that can be manipulated using scanning tunneling microscope tips [28]. These properties can be used to develop unique functionality at the nanoscale and have direct

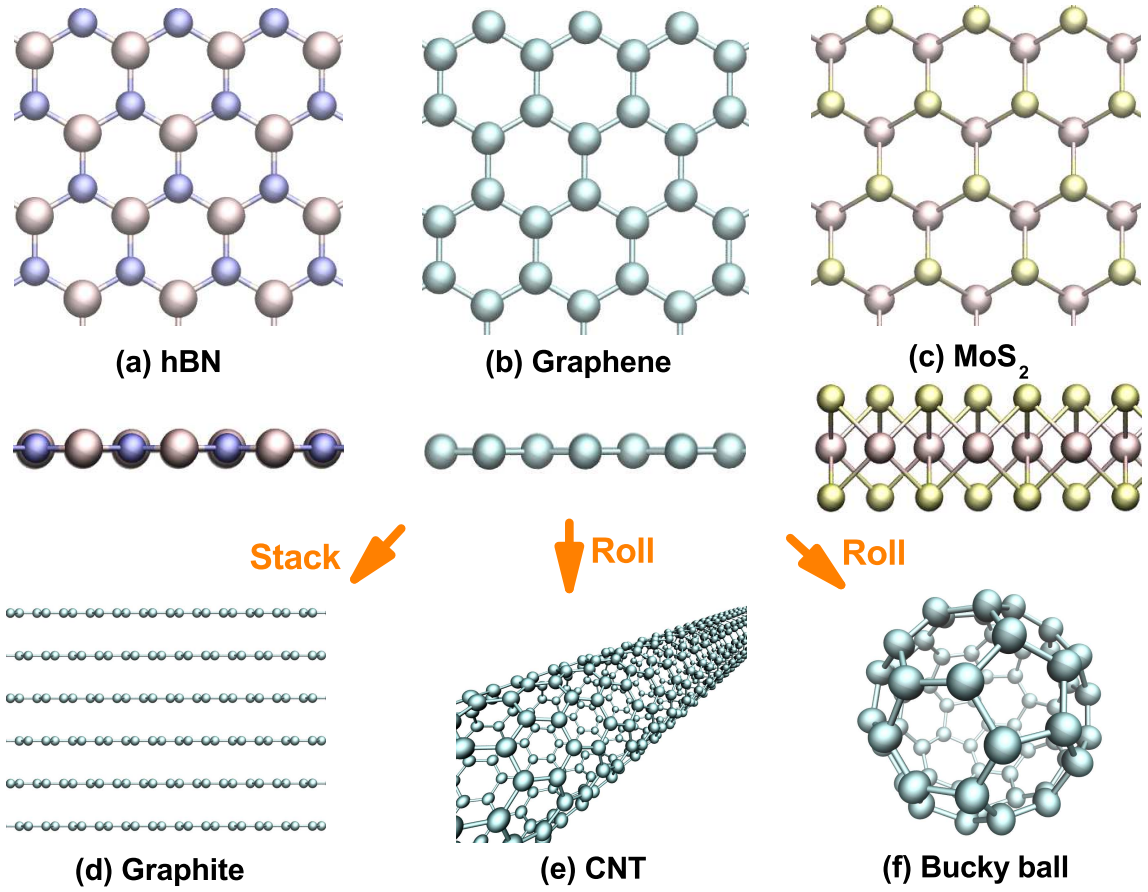

Figure 1.1: Graphene and graphene-like materials considered in this work: (a) hexagonal boron nitride (hBN); (b) Graphene; ; (c) Molybdenum disulfide (MoS_2); (d) graphite; (e) carbon nanotube (CNT); (f) bucky ball. The top view and the side view for (a)-(c) are shown.

applications in sensing, molecular memories, and high-frequency resonators.

Understanding the behavior of confined water is also important because many applications of graphene and graphene-like materials involve water. For example, Graphene is one-atom thick, which has been proposed as the membrane for energy-efficient seawater desalination [29, 30, 31] since the energy consumption of the reverse osmosis reduces as the membrane thickness decreases. Graphene is also transparent, flexible, and robust, and has been used as an electrode for *in vivo* tests in biological systems [32]. The electronic property of graphene is tunable by charged molecules like DNA, and therefore graphene has been proposed for DNA sequencing [33].

Compared to graphene, hBN and MoS_2 are superior in some applications: (1) Graphene has a zero band gap and MoS_2 has a non-zero band gap. In the application of field effect transistors which requires a gap, MoS_2 outperforms graphene [34]. (2) Graphene is one-atom thick and MoS_2 is 3-atom thick which is about the size a DNA base. As a result, DNA sequencing based on MoS_2 nanopore outperforms graphene. (3) BN

and MoS_2 have better biocompatibility than graphene and they don't affect the growth of cells [35] or induce biomolecule adsorption. (4) hBN possess good electrical insulation [36], chemical inertness [37]. (5) Large surface charge can be induced for BN nanotube [38] or MoS_2 nanopore [22], which leads to a giant current through the tube or pore when there is an ionic gradient. This can be applied to harvesting electricity from sea water. So hBN and MoS_2 are also promising materials, complementary to graphene in some aspects. All these applications perform in aqueous environments. Understanding behaviors of the confined water helps in design and optimization of these applications.

1.3 Molecular Dynamics Simulations to Study Confined Water

Molecular dynamics (MD) simulation has been an important tool in studying confined water at the nanoscale. The role of MD in studying confined water can be illustrated by the example of water contact angle on defective graphite: Experimentally it was found that a graphite surface becomes superhydrophilic when the surface is treated by argon plasma [11]. The contact angle changes from 50° to close to 0°, as shown in Fig. 1.2(a). Defects that may exist on the surface and contribute to the change in contact angle include single vacancy defect, double vacancy defect, Stone-Wales defect, C-H adsorption, and C-OH adsorption. MD is capable of isolating individual effects by considering one defect at a time in the simulations to see the change angle change, as shown in Fig. 1.2(b). It shows that the C-OH adsorption changes contact angle significantly, while other defects barely change contact angle. The XPS experiment also confirms that the defect density used in MD is reliable, as shown in Fig. 1.2(c). The simulations not only reproduced the experimental measurements, as shown in Fig. 1.2(d), but also explained that the OH adsorption is main contribution to the contact angle change. From this example, we see that MD is a powerful tool in providing insights to understand mechanisms of these complex systems.

MD simulations have been applied to study behavior of confined water behavior at the graphene/graphene-like surface, e.g. wetting behavior [39, 15], ion selectivity [29, 40, 41, 42], water transport [20, 24, 43], wettability [20]. In these simulations, the van der Waals (vdW) interaction between water and the surface, ΔE_{vdW}, is computed by a summation of the interaction between all atom pairs represented by the Lennard-Jones (LJ) 6-12 interatomic potential U_{ij}^{LJ}:

$$\begin{aligned} \Delta E_{\mathrm{vdW}} &= \sum_{i \in \mathrm{surface}} \sum_{j \in \mathrm{water}} U_{ij}^{\mathrm{LJ}}(r_{ij}) \\ U_{ij}^{\mathrm{LJ}}(r_{ij}) &= 4\epsilon_{ij}\left[\left(\frac{\sigma_{ij}}{r_{ij}}\right)^{12} - \left(\frac{\sigma_{ij}}{r_{ij}}\right)^{6}\right] \end{aligned} \tag{1.1}$$

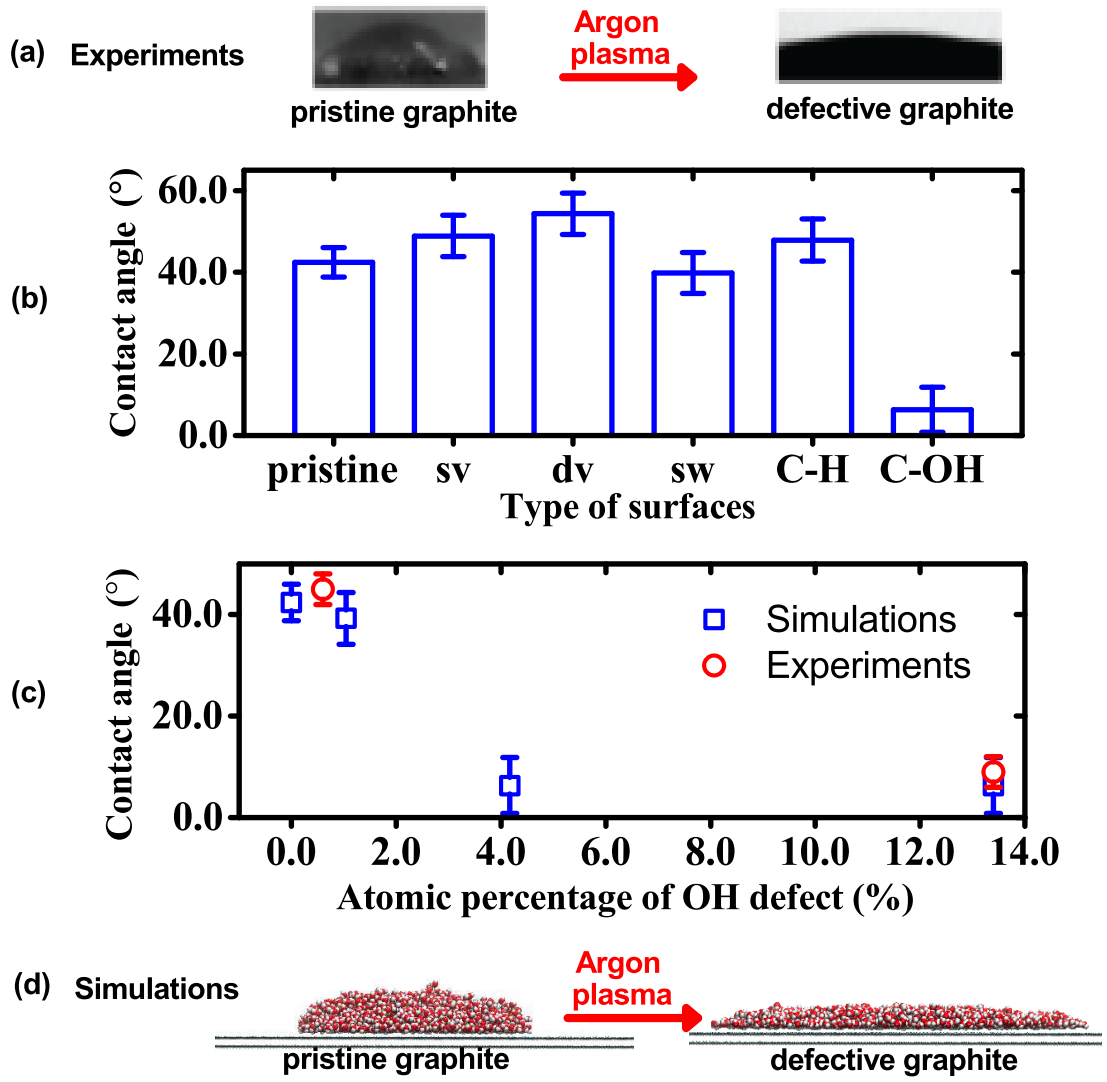

Figure 1.2: (a) Experimental measurements of water contact angles on pristine and defective graphite. The pristine graphite becomes defective after the argon plasma treatment. (b) Molecular dynamics simulations of the water contact angle on pristine graphite, graphite with single vacancy defects (sv), graphite with double vacancy defects (dv), graphite with StoneWales defects (sw), graphite with single vacancy defects and hydrogen chemisorption (C-H), and graphite with single vacancy and hydroxyl chemisorption (C-OH). The atomic percentage of defects, defined by the number of defective sites over the number of carbon atoms on the top layer, is 4.2% for surfaces with defects in (b). (c) Contact angle on graphite with hydroxyl chemisorption of various atomic percentages, by both experiments and simulations. The error bars of the simulation results in (b) and (c) show the standard deviations of contact angle values from three simulation runs with different initial velocity configurations. (d) Molecular dynamics simulations of water contact angles on pristine and defective graphite.

where r_{ij} is the distance between atom i and atom j, ε_{ij} is the depth of the potential well of the atomic interaction, and $2^{1/6}\sigma_{ij}$ is the position of the potential well, as shown in Fig. 1.3. ε_{ij} and σ_{ij} are predefined sets of parameters depending on the atomic types of atom i and atom j. These parameters are called force

field parameters, which are input for MD simulations.

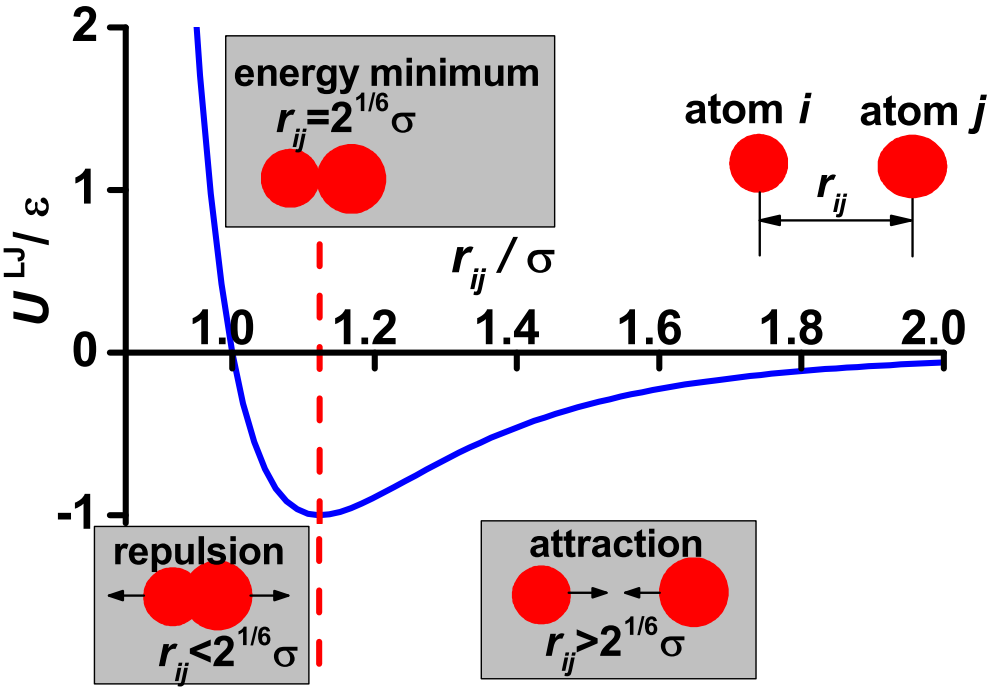

Figure 1.3: The Lennard-Jones (LJ) interatomic potential, U_{LJ}, between atom i and atom j. r_{ij} is the distance between the two atoms, ε is the depth of the potential well, and $2^{1/6}\sigma$ is the position of the potential well. The values in x axis are normalized by σ, and the values in y axis are normalized by ε.

It has been shown that predicted properties using MD depend on the force field parameters input. Hummer et al. [39, 44] showed that a small change in carbon-water interaction can lead to totally different predictions of whether a CNT can be filled by water. Similarly Werder et al. [20] found that by varying the carbon-water interaction, the predicted water contact angles on graphite can range from very hydrophobic (138.8°) to pretty hydrophilic (50.7°). So in order to describe the surface in a realistic way, accurate force field parameters are needed.

For the most part force field parameters have historically been developed using one of two approaches. The first approach is to combine the force field parameters for water-water interaction and surface-surface interaction, based on the Lorentz-Berthelot combinational rule:

$$\begin{aligned} \sigma_{\text{S-W}} &= \frac{\sigma_{\text{W-W}} + \sigma_{\text{S-S}}}{2} \\ \varepsilon_{\text{S-W}} &= \sqrt{\varepsilon_{\text{W-W}}\varepsilon_{\text{S-S}}} \end{aligned} \tag{1.2}$$

where $\sigma_{\text{S-W}}$ and $\varepsilon_{\text{S-W}}$ are the force field parameters for surface-water vdW interaction, $\sigma_{\text{W-W}}$ and $\varepsilon_{\text{W-W}}$ are the force field parameters for water-water vdW interaction obtained by studying the bulk water, and $\sigma_{\text{S-S}}$ and

$\varepsilon_{\text{S-S}}$ are the force field parameters for surface-surface vdW interaction obtained by studying the bulk material. This approach is simple and serves as a good starting point. The approach may work for cross-interaction between materials that are similar. Given that water is quite different from graphene/graphene-like materials, the accuracy of the parameters using this approach must be checked experimentally.

The second approach is based on experimental data. The idea is to adjust the force field parameters so that some properties measured in experiments can be reproduced. The properties are chosen following two criteria: (1) The property should sensitively depend on the water-surface interaction. A small change in parameters should have a distinguishable change in the property, so that the error bar in the parameters developed based on the property is small. (2) The property should be easy to measure, so that we can have data from independent measurements to benchmark each other. Our choice of properties is limited. Contact angle is one of the few properties people have been using. We will use the contact angle as an example to illustrate the challenges in experiments to measure these properties.

Fig. 1.4 gives a summary of the water contact angle values on graphite reported by different experimental groups [7, 8, 9, 10, 4, 5, 11, 12]. We see a scattering of results among different groups: Before 2013, graphite was widely accepted as hydrophobic. Li et al. [12] in 2013 and Ashraf et al. [11] in 2014 independently found that the ppb (parts per billion) level airborne hydrocarbon contaminates the graphene/graphite surface within minutes after the surface is exposed to air. If the surface were not properly cleaned, the graphite surface would be mistaken as hydrophobic. Ashraf et al. also showed that with defects, the surface may become more hydrophilic. Because contact angle sensitively depends on the surface-water interaction, as required by criteria (1), to measure contact angle accurately, the surface has to be in well-controlled condition, which makes the measurement challenging, contradictory with criteria (2). This may explain why there are limited properties we can choose from and the uncertainties in the reported values of these properties. Given the limited properties available and the uncertainties in reported values, developing force field parameters based on one experimental data point may not be reliable.

Using one of the two approaches, various water-surface interaction parameters have been proposed in the literature [39, 45, 46, 47, 20, 48, 49], as summarized in Table 1.1 or Table A.1 for grahene-water interaction, Table A.2 for hBN-water interaction, and Table A.3 for MoS_2-water interaction. The first four sets of parameters in Table 1.1 are based on combinational rule: The resulting values vary since the carbon-carbon and water-water parameters are from different sources. Some parameters put all the vdW interaction on oxygen atom, while others partitions the vdW interaction on both oxygen and hydrogen atoms to include water-orientation dependence. The remaining four sets of parameters are obtained by fitting to experiments: The values are different since different contact angle values were used in the fitting. It is not easy to get an

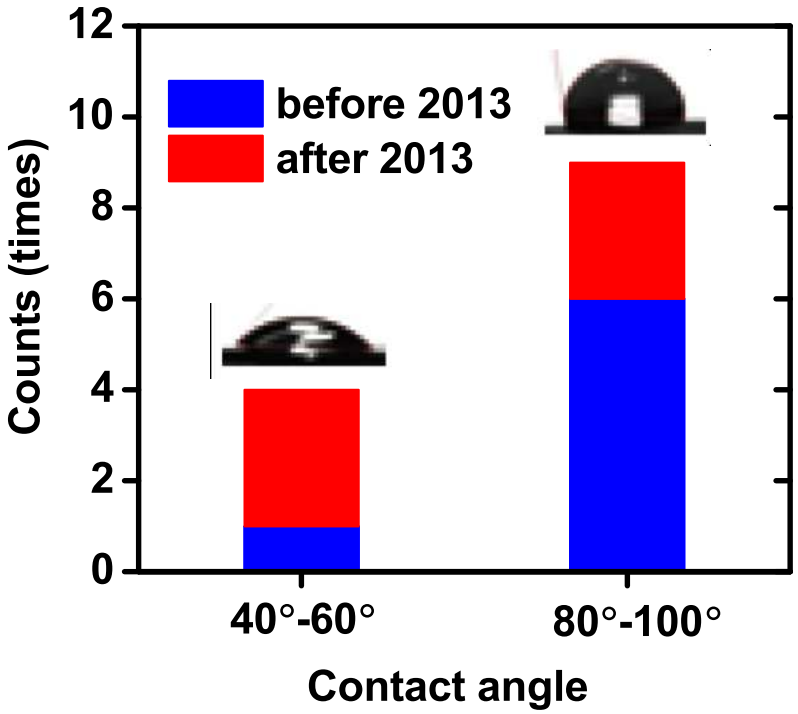

Figure 1.4: Contact angle values reported by experiments [7, 8, 9, 10, 4, 5, 11, 12]. The x-axis shows the ranges of contact angles, and y axis shows the count the values have been reported. The counts are divided before and after the year of 2013. For example, A count of "4" with the range of "40°-60°" means four different groups reported contact angle values in the range of 40°-60°. And out of the four groups, one of them reported values before the year of 2013, and three of them reported values after the year of 2013.

idea of the difference between these parameters by just looking at the values of these force field parameters. Instead, we can use the parameters to predict properties to show their difference. We use the parameters to predict CNT wetting behavior, which is quantified by the percentage of filled status over time, as shown in Fig. 1.5(a). The predicted values vary in a big range. We also use the parameters to predict water contact angle on graphite, as shown in Fig. 1.5(b). The graphite surface is predicted from superhydrophilic to hydrophobic, depending on the parameters. The properties predicted using these force field parameters show in a big range. We need approaches that can consistently produce accurate force field parameters.

1.4 Developing Force Field Parameters from First Principles

Developing force field parameters from first principles has the advantage of being non-empirical. This approach has been recently successfully applied to developing force field parameters for some systems. Bukowski et al. [50] developed force field parameters for water entirely from first principles, without any fitting to experimental data. The force field is able to predict the spectra, second-virial coefficient of dimer, radial dis-

Table 1.1: An incomplete list of LJ parameters in the literature. The LJ parameters include carbon-water oxygen parameters $\sigma_{\text{C-OW}}$ and $\epsilon_{\text{C-OW}}$, and carbon-water hydrogen parameters $\sigma_{\text{C-HW}}$ and $\epsilon_{\text{C-HW}}$. $\sigma_{\text{C-OW}}$ and $\sigma_{\text{C-HW}}$ are in Å, and $\epsilon_{\text{C-OW}}$ and $\epsilon_{\text{C-HW}}$ are in kcal/mol. More details about the force field parameters can be found in Table A.1.

Groups	Approach	$\sigma_{\text{C-OW}}$	$\epsilon_{\text{C-OW}}$	$\sigma_{\text{C-HW}}$	$\epsilon_{\text{C-HW}}$
Hummer et al. [39]	Combinational rule	3.275	0.1143	N/A	N/A
Won et al. [45]	Combinational rule	3.2779	0.1037	N/A	N/A
Noon et al. [46]	Combinational rule	3.296	0.1382	2.58	0.0772
Gordillo et al. [47]	Combinational rule	3.280	0.0930	2.81	0.0308
Werder et al. [20]	Fit to experiments	3.190	0.0937	N/A	N/A
Werder et al. [20]	Fit to experiments	3.190	0.1349	N/A	N/A
Scocchi [48]	Fit to experiments	3.190	0.0478	N/A	N/A
Markovic et al. [49]	Fit to experiments	3.190	0.0935	2.82	0.0605

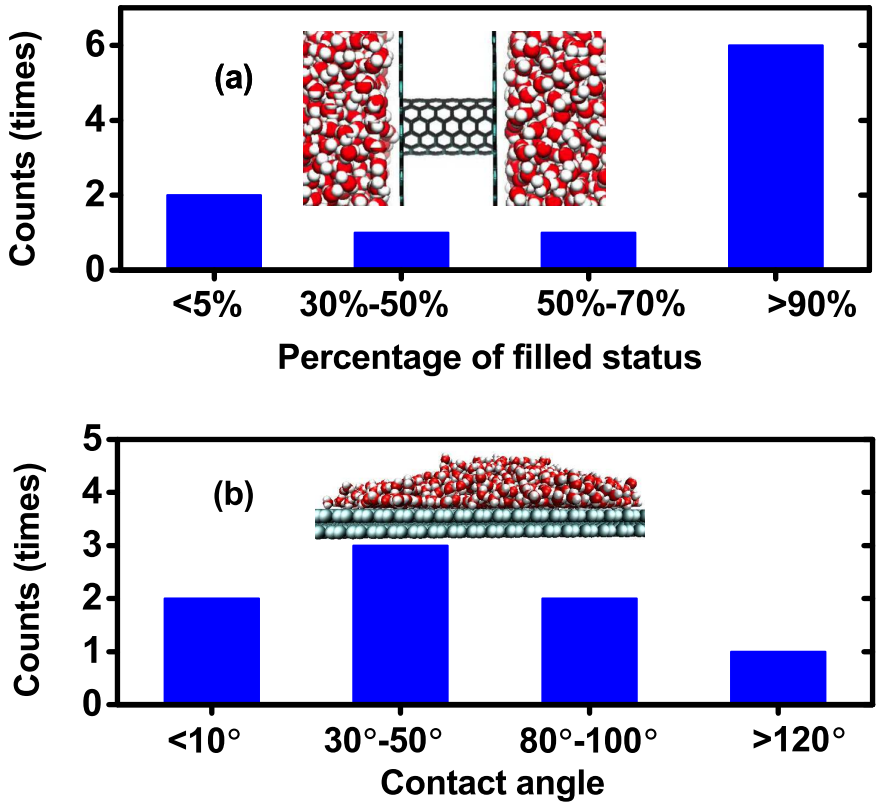

Figure 1.5: (a) carbon nanotube (CNT) wetting behavior predicted by simulations using parameters in Table 1.1. The x-axis shows the percentage of CNT filled status over time. (b) Contact angle values predicted by simulations using parameters in Table 1.1.

tribution function, internal energy, self-diffusion coefficient, and coordination number of liquid water. Pascal et al. [51] developed quantum mechanics based force field parameters at the M06-2X level and accurately predicted experimental lattice vibrations, elastic constant, Poisson ratios, lattice modes, phonon dispersion

curves, specific heat and thermal expansion of graphite. Chiu et al. [52] improved 43A1 lipid force field parameters using electronic structure computations and reproduced experimental X-ray form factors and NMR order parameters over a wide range of membrane compositions. These studies based on first-principle calculations are limited to molecular or bulk systems. We would like to extend this approach to developing force field parameters between a molecule and surfaces.

The force field parameters obtained using this approach depend on the accuracy of the *ab initio* calculations. In order to obtain accurate force field parameters, high-accuracy *ab initio* calculations are needed that can describe electron correlation, which mediates weak interactions like van der Waals (vdW). Density functional theory (DFT), on the contrary, tends to underestimate the interaction strength. It was found that DFT with correction cannot describe bulk water accurately [53]. We need methods beyond DFT.

Methods that describe electron correlation explicitly include: coupled cluster with single and double excitations and perturbative triples (CCSD(T)), diffusion Monte Carlo (DMC) [54, 55, 56], random phase approximation (RPA) [57, 58], and 2nd-order Møller-Plesset perturbation theory (MP2). The CCSD(T) method is called the "gold standard" in the literature for benchmarking other methods. Yet CCSD(T) method scales badly with the system size, which is computationally practical for molecular interactions. The DMC method has about the same accuracy as CCSD(T) and it also scales well with the system size. So DMC is considered as the most accurate method for large systems. Yet DMC is computationally demanding, and only a limited number of configurations can be considered. The RPA and MP2 methods are relatively computationally efficient. But both methods have more approximations and their accuracy has to be verified by comparing to DMC and CCSD(T).

1.5 Outline of the Dissertation

In this dissertation, we propose to develop force field parameters for water interacting with graphene and graphene-like materials from first-principles calculations. We start from many-body quantum mechanics. A combined approach is used in this level to compute the interaction between water and graphene/graphene-like surfaces: The CCSD(T) and DMC methods benchmark each other at the molecular level. Then the DMC method is used to validate RPA and MP2 calculations. If the accuracy of RPA and MP2 methods are acceptable, we will use the RPA or MP2 method to explore the potential energy surface between water and graphene/graphene-like materials. In the next level, we use classical models fitting to the potential energy surface to obtain force field parameters. Once we have the parameters, we would like to verify the parameters by comparing to the experiments. This is done by first performing molecular dynamics simulations with

the force field parameters to predict properties at the nanoscale. Then the properties predicted at the nanoscale are extrapolated to macroscopic scale, so that a direct comparison with experiments is possible. This approach is applied to three systems: hBN-water, graphene-water, and MoS_2-water. The outline of my dissertation is summarized in Fig. 1.6.

The quality of the force field parameters developed in this approach solely depends on the accuracy of first-principle calculation. As a result, the main focus of my PhD work is to obtain the interaction energies as accurate as possible. Chapter 2 explains the methods used in this work. Chapter 3-5 covers applying the approach to hBN, graphene, and MoS_2, respectively. Chapter 6 concludes the work.

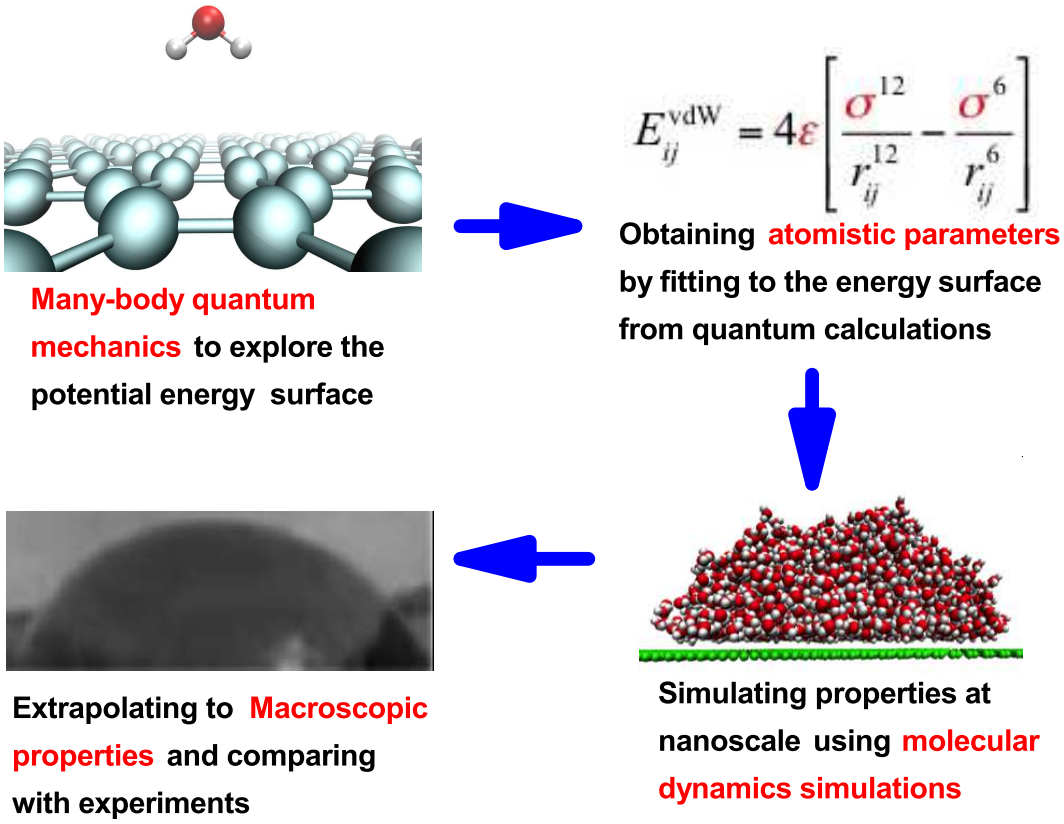

Figure 1.6: The outline of my dissertation. We propose to develop force field parameters for water interacting with graphene and graphene-like materials from first-principle calculations. Many-body quantum mechanics calculations are performed to explore the potential energy surface, which is used to develop force field parameters. We verify the parameters by predicting properties at the nanoscale which are extrapolated to macroscopic level and compared with experiments.

1.6 Accomplishments of My PhD Work

During my PhD study, I computed the interaction energies between hBN and water from first principles, and developed hBN-water force field parameters. I also computed the interaction energies between graphene and water from first principles, developed graphitic carbon-water force field parameters, and applied the force field parameters to water@C60, contact angle on defective graphite, and contact angle on doped graphene. I developed force field parameters for MoS_2-water interaction as well. A summary of the accomplishments achieved and publications in my PhD is summarized in Fig. 1.7.

Compute the interaction energies between hexagonal boron nitride and water from first principles

Y. Wu, L.K. Wagner, N.R. Aluru, The interaction between hexagonal boron nitride and water from first principles, *J. Chem. Phys.* **142**, 234702 (2015)

Develop hexagonal boron nitride-water force field parameters

Y. Wu, L.K. Wagner, N.R. Aluru, Hexagonal boron nitride-water interaction parameters, *J. Chem. Phys.* **144**, 164118 (2016)

Compute the interaction energies between graphene and water using DMC

Y. Wu, H. Zheng, L.K. Wagner, N.R. Aluru, The interaction between graphene and water from DMC, in preparation

Develop graphitic carbon-water force field parameters

Y. Wu, N. R. Aluru, Graphitic carbon-water nonbonded interaction parameters, *J. Chem. Phys. B* **117**, 8802-8813 (2013).

Apply graphitic carbon-water force field parameters to water@C60

A. B. Farimani, Y. Wu, N. R. Aluru, Rotational motion of a single water molecule in a buckyball , *Phys. Chem. Chem. Phys* . **15**, 17993-18000 (2013).

Apply graphitic carbon-water force field parameters to contact angle on defective graphite

A. Ashraf, Y. Wu, M. Wang, N.R. Aluru, S.A. Dastgheib, S. Nam, Spectroscopic Investigation of the Wettability of Multilayer Graphene Using Highly Ordered Pyrolytic Graphite as a Model Material, *Langmuir* **30**, 12827-12836 (2014).

Compute the interaction energies between doped graphene and water using RPA

A. Ashraf, Y. Wu, M.C. Wang, K.H. Yong, T. Sun, Y. Jing, R.T. Haasch, N.R. Aluru, S. Nam, Doping induced tunable wettability of graphene, *Nano Lett.* , DOI: 10.1021/acs.nanolett.6b02228 (2016).

Develop MoS_2-water force field parameters

Y. Wu, M. Heiranian, N.R. Aluru, MoS_2-water interaction parameters, in preparation

Figure 1.7: Accomplishments and publications in my PhD work.

Chapter 2

Methods

2.1 Quantum Methods

In many-body quantum calculations, we solve the time-independent Schrödinger equation to find the ground state:

$$\begin{aligned} \hat{H}\psi_0(\boldsymbol{X}) &= E_0\psi_0(\boldsymbol{X}) \\ \boldsymbol{X} &= (X_1, X_2, \ldots, X_n) \\ \hat{H} &= \hat{T} + \hat{V} \\ \hat{T} &= -\frac{1}{2}\nabla^2 \\ \hat{V} &= -\sum_i^n \sum_I^N \frac{Z_I}{r_{iI}} + \sum_{i<j}^n \frac{1}{r_{ij}} \end{aligned} \tag{2.1}$$

where $\hat{H}$ is the Hamiltonian operator, ψ_0 is the ground state wave function, E_0 is the ground state energy, $\boldsymbol{X}$ is the position of all electrons, $\hat{T}$ is the kinetic operator, $\hat{V}$ is the potential energy operator, Z_I is the charge of the nuclei indexed by I, r_{iI} is the distance between the electron indexed by i and the nuclei indexed by I, and r_{ij} is the distance between the electron indexed by i and the electron indexed by j.

The wave function depends the positions of all electrons in the system, which makes the problem high-dimensional. The electron correlation term r_{ij} couples the position of two electrons. As a result, the problem cannot be decoupled into n one-electron problems. Overall, the problem is high-dimensional, coupled, and very challenging to solve. Various schemes have been proposed to treat the electron correlation term with different levels of approximations. Here I will explain two methods used in this work covering their advantages and approximations.

2.1.1 Diffusion Monte Carolo

In diffusion Monte Carlo (DMC), instead of solving the Schrödinger equation, a different equation is solved

$$-\frac{\partial\varphi(\boldsymbol{X}, t)}{\partial t} = \big(\hat{H} - E\big)\varphi(\boldsymbol{X}, t) \tag{2.2}$$

The equation is called imaginary-time Schrodinger equation because of its similarity to the time-dependent Schrödinger equation except without i on the left:

$$-i\hbar\frac{\partial\Psi(\boldsymbol{X},t)}{\partial t}=\hat{H}\Psi(\boldsymbol{X},t) \tag{2.3}$$

It can be shown that the steady state of the imaginary-time Schrödinger equation is the ground state of the time-independent Schrödinger equation: The imaginary-time Schrödinger equation is first order in time, so the general solution has the form:

$$\varphi(\boldsymbol{X},t)=e^{-(\hat{H}-E)t}\varphi(\boldsymbol{X},0) \tag{2.4}$$

where the $\varphi(\boldsymbol{X},0)$ is the initial condition, which can be written as a linear composition of eigenstates $\psi_i(\boldsymbol{X})$ of $\hat{H}$, i.e., $\hat{H}\psi_i(\boldsymbol{X})=\varepsilon_i\psi_i(\boldsymbol{X})$:

$$\varphi(\boldsymbol{X},0)=\sum_i c_i\psi_i(\boldsymbol{X}) \tag{2.5}$$

Substitute Eq. 2.5 into Eq. 2.4:

$$\begin{aligned}\varphi(\boldsymbol{X},t)&=e^{-(\hat{H}-E)t}\sum_i c_i\psi_i(\boldsymbol{X})\\&=\sum_i e^{-(\varepsilon-E)t}c_i\psi_i(\boldsymbol{X})\end{aligned} \tag{2.6}$$

As $t\to\infty$,

$$e^{-(\varepsilon_0-E)t}c_0\gg e^{-(\varepsilon_i-E)t}c_i \tag{2.7}$$

The excited state components vanishes and the only remaining term is $\psi_0(\boldsymbol{X})$:

$$\varphi(\boldsymbol{X},t)\to\psi_0(\boldsymbol{X})\text{ when }t\to\infty \tag{2.8}$$

The DMC method uses the Monte Carlo technique to find the many-body ground state subject to the fixed node (FN) constraint that the approximate ground state has the same zeros as the trial function. We use as our trial function the Slater-Jastrow wave function

$$\Psi_T(r_1,r_2,\ldots)=\mathrm{Det}[\phi_i(r_j)]\exp\left(\sum_{i<j}u(r_{ij})\right), \tag{2.9}$$

where the one-particle orbitals ϕ_i are obtained from the density functional theory (DFT). The two-body Jastrow factor u is expanded as in Ref [59] and are variance optimized [60]. The DMC method scales well

with system size. So it is considered as the most accurate method for large systems.

2.1.2 Random Phase Approximations

The random phase approximations (RPA) method uses adiabatic connection fluctuation-dissipation (ACFD) theory to capture electron-electron correlation [61, 62]. The ACFD theory is a fairly efficient framework and allows in principle an exact evaluation of the exchange-correlation energy with DFT. Within the ACFD framework, the total energy of a system is reformulated as

$$E = T_{\mathrm{KS}} + E_{\text{ion-el}} + E_{\mathrm{Hxc}} \tag{2.10}$$

where T_{KS} is the kinetic energy of the noninteracting Kohn-Sham (KS) system, $E_{\text{ion-el}}$ is the interaction with the ionic background, and E_{Hxc} is the Hartree and exchange-correlation energy.

The E_{Hxc} equals the integral over the ground-state expectation value of the electron-electron interaction operator $\hat{V}_{\mathrm{ee}}$, when adiabatically switching from the KS system of noninteraction electrons ($\lambda = 0$) to the system of full Coulomb interacting electrons ($\lambda = 1$):

$$\begin{aligned} E_{\mathrm{Hxc}} &= \int_0^1 d\lambda \langle \Psi(\lambda) | \hat{V}_{\mathrm{ee}} | \Psi(\lambda) \rangle \\ \hat{V}_{\mathrm{ee}} &= \frac{1}{2} \sum_{i,j \neq i} \frac{e^2}{|\mathbf{r}_i - \mathbf{r}_j|} \doteq \frac{1}{2} \sum_{i,j \neq i} v(\mathbf{r}_i - \mathbf{r}_j) \end{aligned} \tag{2.11}$$

where $\Psi(\lambda)$ represents the ground state of the Hamiltonian $\hat{H} = \hat{T} + \sum_i v^\lambda(\mathbf{r}_i) + \lambda \hat{V}_{\mathrm{ee}}$, and the local potential v^λ is chosen to fix the electron density to the one of the fully interacting system. For the KS system ($\lambda = 0$), the ground-state wave function is single Slater determinant of one-electron orbitals $\Psi^{\mathrm{KS}} = S(\{\psi_i^{\mathrm{KS}}\})$.

Following the fluctuation-dissipation theorem, E_{Hxc} can be written as

$$E_{\mathrm{Hxc}} = E_{\mathrm{H}}[n] + E_{\mathrm{x}}[\{\psi_i^{\mathrm{KS}}\}] - \int_0^1 d\lambda \int_0^\infty \frac{d\omega}{2\pi} \mathrm{Tr}\{v[\chi^\lambda(i\omega) - \chi^{\mathrm{KS}}(i\omega)]\} \tag{2.12}$$

where $\chi^\lambda(i\omega)$ and $\chi^{\mathrm{KS}}(i\omega)$ are the response function of the interacting system and of the noninteracting system at imaginary frequencies. $E_{\mathrm{x}}[\{\psi_i^{\mathrm{KS}}\}]$ is the exact exchange energy evaluated at the KS orbitals.

The linear response function of the interacting system $\chi^\lambda(i\omega)$ is related to the $\chi^{\mathrm{KS}}(i\omega)$ by a Dyson-like equation:

$$\chi^\lambda(\mathbf{q}, i\omega)^{-1} = \chi^{\mathrm{KS}}(\mathbf{q}, i\omega)^{-1} - [\lambda v(\mathbf{q}) + f_{\mathrm{xc}}^\lambda(\mathbf{q}, i\omega)] \tag{2.13}$$

where $f_{\mathrm{xc}}^\lambda(\mathbf{q}, i\omega)$ is the exchange-correlation kernel, and neglected, an approximation generally referred to as

random phase approximation (RPA).

Then the correlation energy in RPA is written as [57]

$$E_c = \frac{1}{2\pi}\int_0^\infty d\omega \mathrm{Tr}\{\ln[1-\chi^{\mathrm{KS}}(i\omega)\upsilon] + \chi^{\mathrm{KS}}(i\omega)\upsilon\} \tag{2.14}$$

where Tr is the trace, χ^{KS} is the independent particle Kohn-Sham (KS) response function, ω is the frequency, and υ is the Coulomb kernel. The exchange energy, E_{exx}, is calculated exactly using the Hartree-Fock expression. All energies are evaluated using KS orbitals of an initial calculation using the GGA-PBE functional [63].

2.2 Atomistic Simulations

2.2.1 Simulating Water Contact Angle

The bulk graphitic/graphitic-like surface is represented by four layers with an interlayer distance of obtained from experiments. The dimension of each mono layer is about 20 nm × 20 nm, or 30 nm × 30 nm, depending on the droplet size to effectively remove the interaction between the droplet and its periodic images. The surface is fixed throughout the simulation [20]. The simulation box size perpendicular to the surface plane is 20 nm. The MD simulations were performed with GROMACS 4.5.3 package [64]. Time integration is performed using the leap-frog algorithm [65] with a time step of 2.0 fs. The short-range vdW interactions are computed using a cutoff scheme (cutoff distance, 1.4 nm). The long-range electrostatic interactions are computed by using a particle mesh Ewald method (real space cutoff, 1.4 nm; FFT grid spacing, 0.12 nm, fourth-order interpolation). The Nosé-Hoover thermostat [66, 67] with a time constant of 0.5 ps is used to maintain the temperature at 300K. A water cubic box is initially placed on top of the surface. The system is equilibrated for 6 ns using NVT ensemble, during which the water cubic box evolves into a spherical shape. The energy and temperature of the system reach constant values during this equilibration process. The resulting configuration is used as the starting point for further simulations on data collection. For collecting sufficient statistics to compute contact angles, the simulations were run for 4 ns.

2.2.2 Simulating Carbon Nanotube Radial Breathing Mode

The radial breathing mode (RBM) frequencies of an isolated carbon nanotube (CNT) and a CNT surrounded by water are computed by MD simulations. The adaptive intermolecular reactive empirical bond order (AIREBO) potential[68] is used to model the full dynamics of CNT. The water molecules are modeled

by the SPC/E water model [69]. The interactions between CNT atoms and water molecules use the LJ parameters proposed in this work. The CNT considered in this work is a (22,0) zigzag tube, consisting of 352 carbon atoms. The CNT is replicated by periodic boundary conditions along the axial direction to represent an infinite tube. MD simulations are performed with LAMMPS package [70]. Time integration is performed using the Verlet algorithm [71] with a time step of 0.5 fs. The short-range vdW interactions are computed using a cutoff scheme (cutoff distance, 1.2 nm). The long-range electrostatic interactions are computed by using a particle-particle particle-mesh algorithm. The Nosé-Hoover thermostat [72, 73] with a time constant of 0.5 ps is used to maintain the temperature at 300K. The CNT is first relaxed using the NPT ensemble for 200 ps. The pressure is maintained at 1 bar using the Parrinello-Rahman scheme [74]. Then the simulation is switched to the NVT ensemble to collect data for 500 ps. The position and velocity of each carbon atom are stored every 5 fs. The RBM frequency of CNT is calculated as follows [75, 76]: first, velocities of carbon atoms are projected to the radial direction and averaged over all carbon atoms to obtain the average radial velocity of CNT, v_r, for each time frame. Second, the autocorrelation of the average radial velocity, $C(t)$, is computed by:

$$C(t) = \frac{\langle v_r(t) v_r(0) \rangle}{\langle v_r(0) v_r(0) \rangle} \tag{2.15}$$

where $v_r(0)$ and $v_r(t)$ are the average radial velocity of CNT at time 0 and at time t. $\langle\rangle$ denotes average over 200 runs with different initial velocity profiles. Fourier transformation of the velocity autocorrelation gives the power spectra density, $S(\omega)$:

$$S(\omega) = \int_0^\infty dt C(t) cos\omega t \tag{2.16}$$

where $\omega = 2\pi f$ and f is the discrete frequency index. The RBM frequency of CNT corresponds to the peak position in the power spectra density. The least square fitting of a Gaussian function to the peak is done to obtain the frequency.

2.3 Fitting and Analysis

2.3.1 Function Forms Considered in Potential Fitting

The general LJ m-n potential form to describe van der Waals (vdW) interaction between atoms is given by:

$$V_{ij}^{m-n} = \frac{D_v}{n-m}\left[m\left(\frac{R_v}{R_{ij}}\right)^n - n\left(\frac{R_v}{R_{ij}}\right)^m\right] = \frac{C_n}{R_{ij}^n} - \frac{C_m}{R_{ij}^m} \;\; (m=6, n>m) \tag{2.17}$$

where D_v and R_v are the well depth and position, and R_{ij} is the separation distance between atom i and atom j. The force constant at the well position is $k_v = (\frac{\delta^2 E}{\delta R^2})|_{R_v} = mn\frac{D_v}{R_v^2}$. Here m is equal to 6 because the dispersion and induction energy vary as R_{ij}^{-6} [3]. The general LJm-n potential form is reduced to the commonly used LJ6-12 form when n=12:

$$V_{ij}^{6-12} = D_v\left[\left(\frac{R_v}{R_{ij}}\right)^{12} - 2\left(\frac{R_v}{R_{ij}}\right)^6\right] = 4\epsilon\left[\left(\frac{\sigma}{R_{ij}}\right)^{12} - \left(\frac{\sigma}{R_{ij}}\right)^6\right] \tag{2.18}$$

where $\epsilon = D_v$ and $\sigma = R_v/2^{\frac{1}{6}}$. Compared to the Buckingham and Morse potential, which have a third parameter [51] to control the force constant k_v, LJm-n potential form has a fixed force constant once m and n are chosen. To study the effects of varying the force constant, the LJ6-14 function form [77, 78] and LJ6-10 potential form [79, 80, 81] are used besides the commonly used LJ6-12 potential form [82, 83, 84, 85, 86].

2.3.2 Error Propagation in Least Square Fit

Following the procedure in Taylor's book [87], for the problem

$$y = A + Bx \tag{2.19}$$

A and B are represented by

$$\begin{aligned} A &= \frac{\sum x^2 \sum y - \sum x \sum xy}{\Delta} \\ B &= \frac{N\sum xy - \sum x \sum y}{\Delta} \\ \Delta &= N\sum x^2 - \left(\sum x\right)^2 \end{aligned} \tag{2.20}$$

The uncertainty in the measurement y_1, y_2, ..., y_N is

$$\sigma_y = \sqrt{\frac{1}{N-2}\sum_{i=1}^{N}(y_i - A - Bx_i)^2} \tag{2.21}$$

The error in y is propagated to A and B by

$$\begin{aligned} \sigma_A &= \sigma_y \sqrt{\frac{\sum x^2}{\Delta}} \\ \sigma_B &= \sigma_y \sqrt{\frac{N}{\Delta}} \end{aligned} \tag{2.22}$$

Suppose y_i has given uncertainty σ_i, we define the weight of the ith measurement as $w_i = 1/\sigma_i^2$. Then the best estimate of A and B are

$$\begin{aligned} A &= \frac{\sum wx^2 \sum wy - \sum wx \sum wxy}{\Delta} \\ B &= \frac{\sum w \sum wxy - \sum wx \sum wy}{\Delta} \\ \Delta &= \sum w \sum wx^2 - \left(\sum wx \right)^2 \end{aligned} \tag{2.23}$$

Accordingly, the uncertainty in A and B are given by

$$\begin{aligned} \sigma_A &= \sqrt{\frac{\sum wx^2}{\Delta}} \\ \sigma_B &= \sqrt{\frac{\sum w}{\Delta}} \end{aligned} \tag{2.24}$$

2.3.3 Charge-Quadruple Interaction

The electrostatic energy $E_{q\Theta}$ between a point charge q and a quadrupole Θ is [88]

$$E_{q\Theta} = \frac{1}{3} q \sum_{\alpha,\beta} \Theta_{\alpha\beta} \frac{3R_\alpha R_\beta - R^2 \delta_{\alpha\beta}}{R^5} \tag{2.25}$$

where α, β runs over all Cartesian coordinates x, y, and z, and R is distance between the charge and the quadrupole.

For graphene which only has non-zero Θ_{zz}, the electrostatic interaction energy between a carbon quadrupole Θ_{zz} and the partial charges in a molecule is [88, 3]

$$\begin{aligned} E_{q\Theta} &= \frac{1}{2} \Theta \sum_i q_i \left[\frac{3z_i^2}{R_i^5} - \frac{1}{R_i^3} \right] \\ &= \frac{1}{8\pi\epsilon_0} \Theta \sum_i q_i \left[\frac{3z_i^2}{R_i^5} - \frac{1}{R_i^3} \right] \end{aligned} \tag{2.26}$$

Chapter 3

Hexagonal Boron Nitride-Water Interaction Parameters

In this chapter, we use a combined approach to study the interaction between hBN and water: The CCSD(T) and DMC methods benchmark each other at the molecular level. Then the DMC method is used to validate RPA and MP2 calculations. For this system, both RPA and MP2 methods obtain indistinguishable results compared to DMC, so we use the RPA method to explore the potential energy surface between water and hBN. The potential energy surface is used to develop force field parameters with no fitting to experiments. The parameters are then validated by predicting water contact angle on hBN and comparing to experimental measurements. We show that the force field parameters developed based on the first-principle calculations are able to predict the contact angle of water in close agreement with experiments. This demonstrates a multiscale approach that extends from detailed high accuracy diffusion Monte Carlo to macroscopic properties of a molecular-solid interaction.

3.1 CCSD(T) Calculations

3.1.1 System Setup

The all-electron CCSD(T) calculations were performed with Dunning's correlation consistent basis set aug-cc-pVXZ (X=D,T,Q) [89]. The system is composed of a single water moelcule and a $B_3N_3H_6$ molecule, with oxygen atom on top of the center of the $B_3N_3H_6$ molecule and separated from the $B_3N_3H_6$ plane by 3.36 Å, and the water dipole perpendicular to the $B_3N_3H_6$ plane. The water monomer is set to the experimental gas phase geometry [90], and B-N bond length and B-N-B, N-B-N bond angles are set to the experimental values for h-BN [91]. The B-H and N-H bond lengths are obtained by optimizing the structure while fixing the B-N bond length and B-N-B, N-B-N, B-N-H, and N-B-H angles as 120° using DFT with PBE functional and aug-cc-pVTZ basis. The resulting B-H bond length is 1.1929 Åand N-H bond length is 1.0044 Å. Optimization using a B3LYP functional or aug-cc-pVDZ basis gives a difference of less than 1%. The CCSD(T) calculations were performed using Gaussian [92].

3.1.2 Error Control in CCSD(T)

The CCSD(T) procedure has one well-defined approximation: the basis set incompleteness error. The basis set incompleteness error is minimized by using Dunning's correlation consistent basis set aug-cc-pVXZ (X=D,T,Q) [89] and extrapolating to the complete basis set (CBS) limit, as shown in Fig. 3.1. The interaction energy evaluated at CCSD(T) is decomposed into three parts: the HF contribution, the MP2 contribution beyond HF, and the CCSD(T) contribution beyond MP2. Each of the three parts are extrapolated to CBS limit following a different empirical relation [93, 94, 95]:

$$\begin{aligned} E_{\mathrm{CBS}}^{\mathrm{CCSD(T)}} &= E_{\mathrm{CBS}}^{\mathrm{HF}} + \left(E_{\mathrm{CBS}}^{\mathrm{MP2}} - E_{\mathrm{CBS}}^{\mathrm{HF}}\right) + \left(E_{\mathrm{CBS}}^{\mathrm{CCSD(T)}} - E_{\mathrm{CBS}}^{\mathrm{MP2}}\right) \\ E_{\mathrm{CBS}}^{\mathrm{HF}} &= E_{X}^{\mathrm{HF}} + A\exp(-1.63X) \\ \left(E_{\mathrm{CBS}}^{\mathrm{MP2}} - E_{\mathrm{CBS}}^{\mathrm{HF}}\right) &= \left(E_{X}^{\mathrm{MP2}} - E_{X}^{\mathrm{HF}}\right) + BX^{-3} \\ \left(E_{\mathrm{CBS}}^{\mathrm{CCSD(T)}} - E_{\mathrm{CBS}}^{\mathrm{MP2}}\right) &= \left(E_{X}^{\mathrm{CCSD(T)}} - E_{X}^{\mathrm{MP2}}\right) \end{aligned} \tag{3.1}$$

where $E_{\mathrm{CBS}}^{\mathrm{CCSD(T)}}$, $E_{\mathrm{CBS}}^{\mathrm{MP2}}$, and $E_{\mathrm{CBS}}^{\mathrm{HF}}$ are the interaction energy evaluated using CCSD(T), MP2, and HF with CBS, $E_{X}^{\mathrm{CCSD(T)}}$, E_{X}^{MP2}, and E_{X}^{HF} are the interaction energy evaluated using CCSD(T), MP2, and HF with aug-cc-pVXZ (X=D,T,Q) basis. We used two basis sets (X=T,Q) in the extrapolation. To check the convergence of the extrapolated value with the two basis sets used, we considered a smaller basis set pair (X=D,T), and the difference in the extrapolated values is less than 1 meV. The error on the interaction energy by CCSD(T) by is less than 1 meV.

3.2 DMC Calculations

3.2.1 System Setup

The DFT calculations were performed with the PBE functional using the Crystal 2009 [96]. Energy-consistent pseudopotentials were used [97] with correction for hydrogen atoms [98]. A triple-zeta basis set with reduced diffuse coefficient was used to obtain convergence in DFT, and a k-point mesh equivalent to a 24×24×1 mesh on the primitive cell of h-BN was used. One water molecule per 2×2 BN supercell was considered. The water monomer is set to the experimental gas phase geometry [90], and B-N bond length and B-N-B, N-B-N bond angles are set to the experimental values for h-BN [91]. The variational Monte Carlo (VMC) and DMC calculations were performed using QWalk [99].

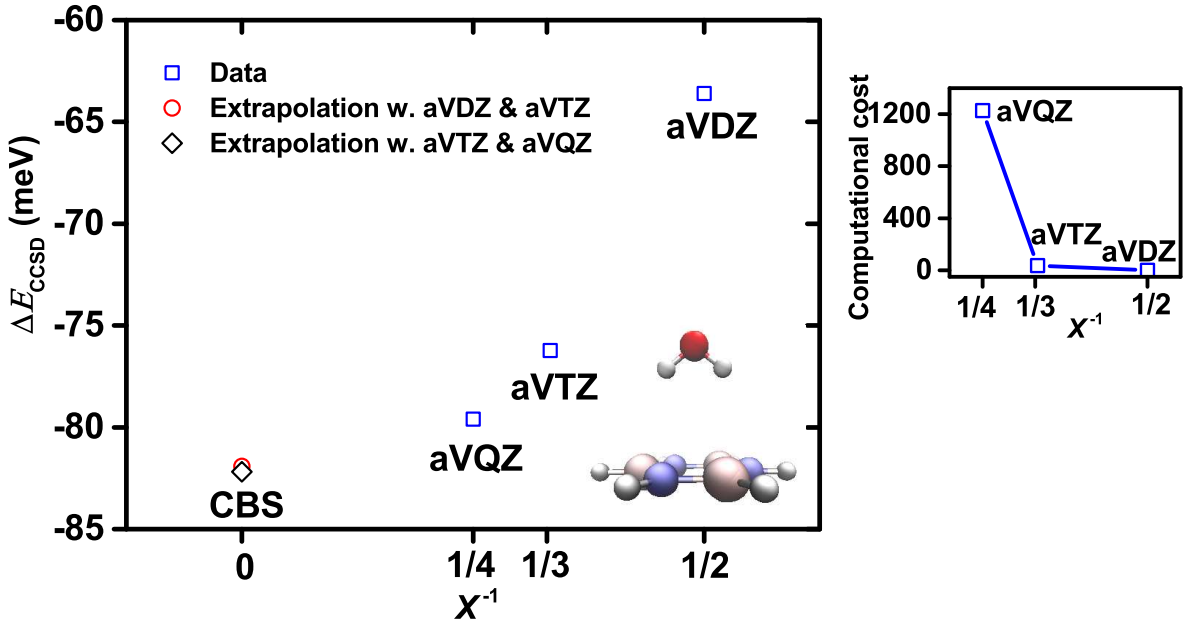

Figure 3.1: The interaction between $B_3N_3H_6$ computed at various basis sets and extrapolated to the complete basis set (CBS) limit. The oxygen of the water molecule is separated from the $B_3N_3H_6$ plane by 3.6 Å. The sum of the energy of isolated $B_3N_3H_6$ and the energy of isolated water is used as the zero energy reference. The basis sets used are Dunning's correlation consistence basis set, aug-cc-pVXZ (X=D,T,Q), shortened as aVXZ in the figure. The computational cost, normalized by that using the aVDZ basis, is shown in the inset figure.

3.2.2 Error Control in DMC and Compared to CCSD(T)

The DMC procedure has a few well-defined approximations. We categorize errors due to the approximations into methodological errors and systematic errors. The methodological errors include errors due to the fixed-node approximation and pseudo potential. The systematic errors include errors due to the finite time step, finite supercell size, incomplete basis sets, and non-zero water coverage density.

We checked the methodological approximations by comparing to coupled cluster calculations with single and double excitations and perturbative triples in the complete basis set limit (CCSD(T)/CBS) [94]. We used the $B_3N_3H_6$-water system as a proxy in which all errors could be controlled. The $B_3N_3H_6$-water interaction energies as a function of the separation distance h are summarized in Fig. 3.2. Both DMC and CCSD(T)/CBS predict that the energy minimum in the distance scan is when h = 3.36 Å. The binding energies calculated by DMC and CCSD(T)/CBS agree within stochastic uncertainty. The agreement between DMC and CCSD(T)/CBS is also good in the medium separation distance range (4-6 Å) and repulsive region ($<$ 3.2 Å). From these tests, it appears that the fixed node and pseudopotential approximations do not strongly affect the interaction energy of water with $B_3N_3H_6$. Assuming that these errors translate to the

water-h-BN system, we expect the errors due to these approximations to be minimal.

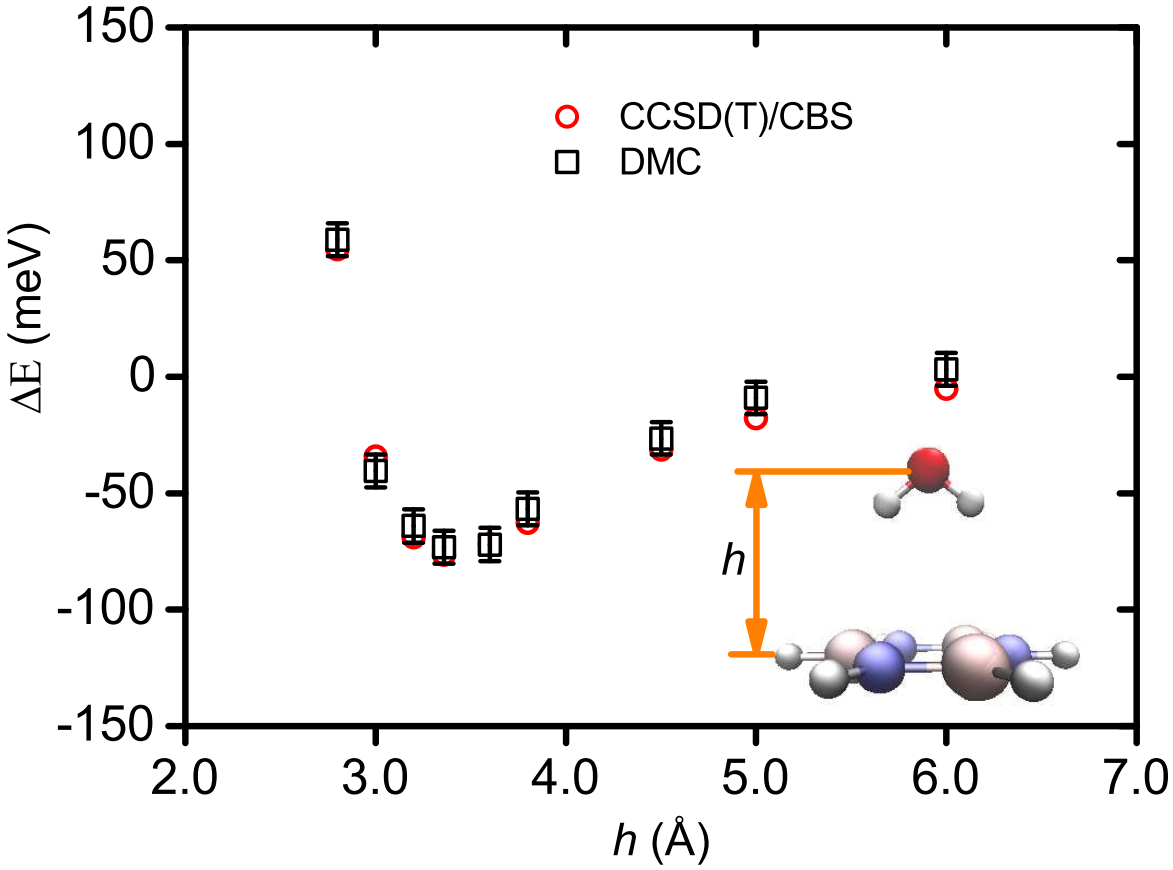

Figure 3.2: $B_3N_3H_6$-water interaction energies calculated by the diffusion Monte Carlo (DMC) and coupled cluster method with single and double excitations and perturbative triples at complete basis set limit (CCSD(T)/CBS). The configuration of $B_3N_3H_6$ and water separated by 7 Å is used as the zero-reference-energy configuration. The energies predicted using the DMC method are in good agreement with those calculated using the CCSD(T)/CBS within the error bars.

We also checked the error due to the fixed node approximation in h-BN by changing the DFT functional used to generate the orbitals. The DFT functional has the form: $E_{\rm xc} = \alpha E_{\rm x}^{\rm HF} + (1-\alpha)E_{\rm x}^{\rm PBE} + E_{\rm c}^{\rm PBE}$, where $E_{\rm x}^{\rm HF}$ is the Hartree-Fock (HF) exchange functional, $E_{\rm x}^{\rm PBE}$ is the PBE exchange functional, and $E_{\rm c}^{\rm PBE}$ is the PBE correlation functional. The DFT functional was changed by systematically varying α from 0 to 40%. The change in the DMC results using Slater determinants generated from DFT with different α is negligible within error bars, as shown in Fig. 3.3. Therefore, it appears that for reasonable changes in the Slater determinant, the results of the fixed node DMC procedure do not change.

We checked the basis set convergence by varying the diffuse function in the basis set. Doubling the diffuse coefficient, which changes the interaction energy from DFT by as much as 200%, has little effect on the interaction energy from DMC. We checked the k-point, time step and water coverage density convergence

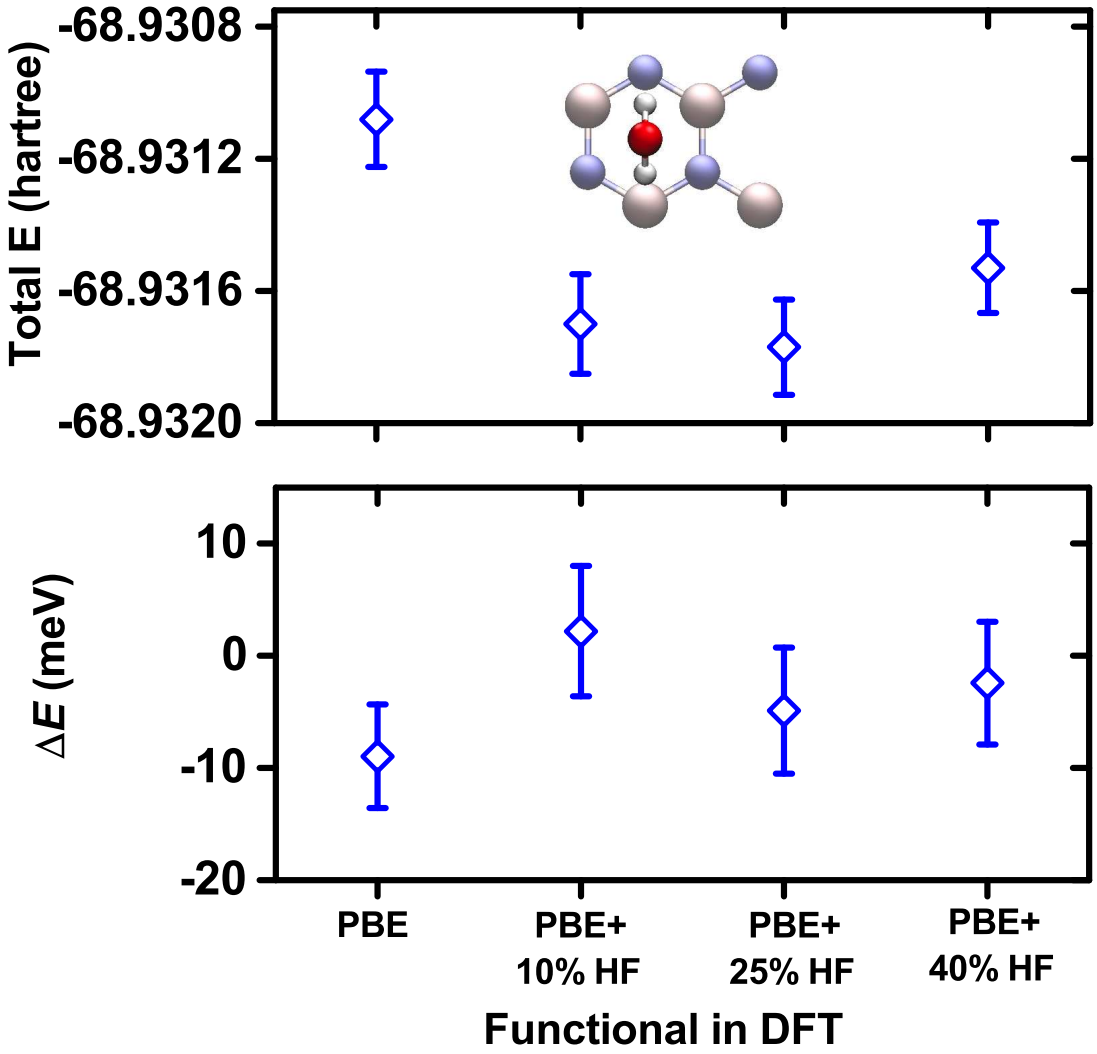

Figure 3.3: Dependence of the h-BN-water energy and interaction energy predicted by the diffusion Monte Carlo (DMC) on functional used in the density functional theory (DFT) to generate orbitals. The functional combines PBE with HF of varying percentage from 0 to 40%. The 2×2 supercell is used.

by halving each and finding that the interaction energies stay the same within the error bars.

The finite size error of water-h-BN interaction was controlled by considering h-BN systems represented by supercells of different size. The total energy and interaction energies for various supercells are plotted versus 1/N (N is the number of water molecules) and extrapolation by a linear fit, as shown in Fig. 3.4. The finite size error in the interaction energy calculated by DMC is not negligible. Extrapolation is necessary to estimate the finite size error and predict water-h-BN interaction energy at infinite size limit. Considering all the approximations, we estimated the error to be less than ±5 meV on the interaction energy. Thus, our FN-DMC calculations provide a binding energy between h-BN monolayer and water of 76 ± 6 ± 5

meV. The first error is the statistical error and the second error is the systematic error. After this work was submitted for review, we were made aware of the paper by Hamdani et al. [14], who performed a very similar calculation in FN-DMC. Their FN-DMC results are within statistical uncertainties of ours.

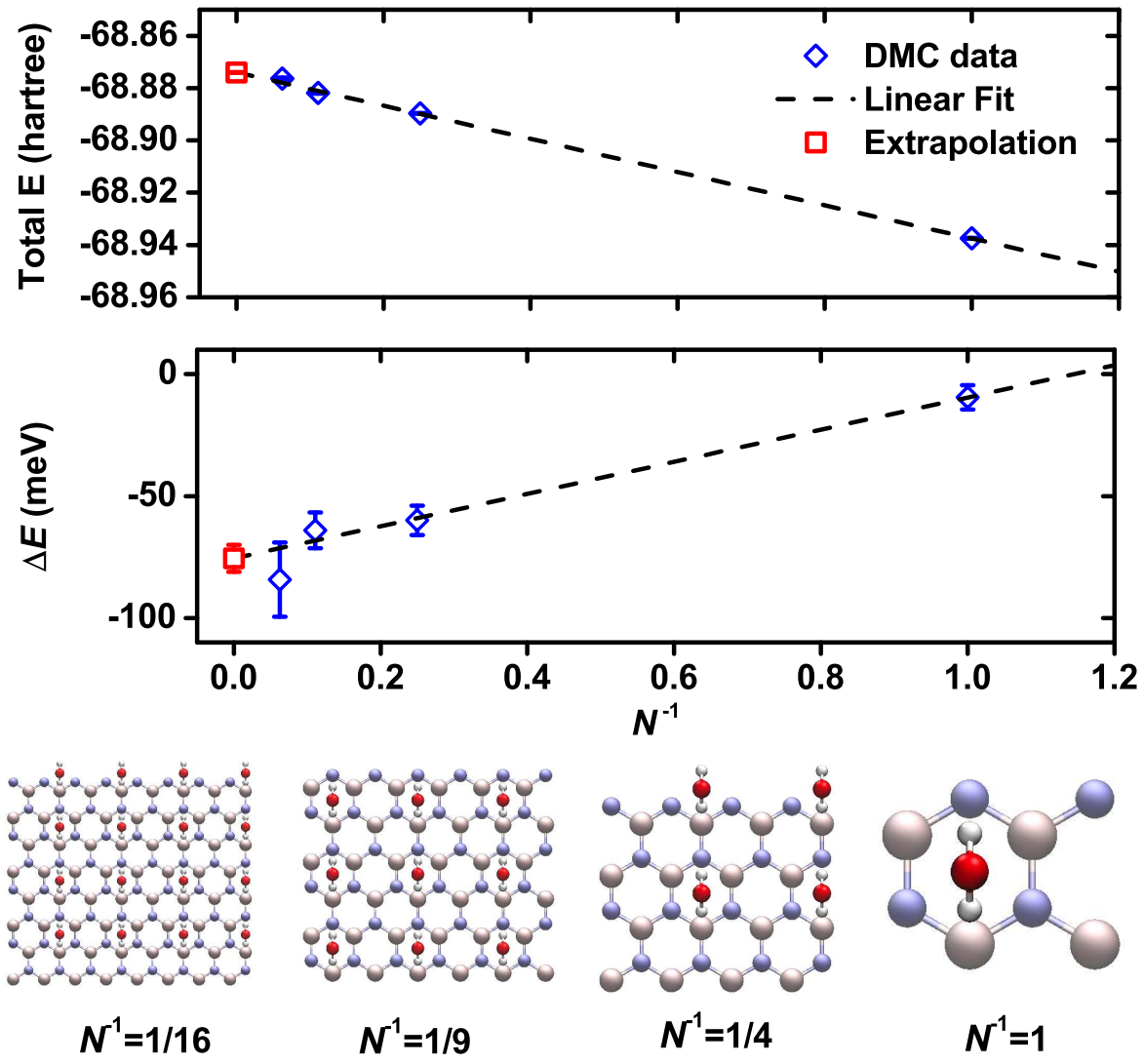

[!ht]

Figure 3.4: Finite size convergence of total energy and interaction energies in the diffusion Monte Carlo (DMC) calculations. N is the number of water molecules in the supercell. A linear fit is shown.

3.2.3 Use DMC to Evaluate DFT with Dispersion Correction

We can also use our DMC result to evaluate the performance of DFT with dispersion correction. Two correction schemes, PBE-D2 following Grimme's protocol [18] and PBE-TS following Tkatchenko and Scheffler's

protocol [19], were considered. The binding energy using PBE-D2 agrees with the result by Hilder et al. using BLYP-D2 [17]. Compared to the DMC result, both PBE-D2 and PBE-TS overestimate the magnitude of the water-h-BN interaction, as shown in Fig. 3.7.

3.3 RPA Calculations

3.3.1 System Setup

The RPA calculations were performed using the VASP package [100, 101], projector-augmented wave potentials, and an energy cutoff of 408 eV. The response function was expanded in plane waves up to an energy cutoff of 272 eV. The exchange energy and correlation energy are computed separately with different hBN supercell sizes and Brillouin zone sampling Monkhorst-Pack k-meshes [102]: A 8×8 supercell with a 2×2 k-mesh was used for the exchange energy, and a 2×2 supercell with a 4×4 k-mesh for the correlation energy. A lattice constant of 15 Å along the direction perpendicular to the hBN surface (z-axis) was used. The potential energy surface between hBN and water was computed using the RPA method by varying the separation distance and orientation of the water molecule with respect to the hBN surface. For simplicity, the hBN and the water molecule internal geometry were fixed while changing their relative position: The B-N bond length and B-N-B, N-B-N bond angles are set to the experimental values for hBN [91], and the water monomer is set to the experimental gas phase geometry [90]. The interaction energy between water and hBN, ΔE, is computed by $\Delta E = E(\text{hBN-water}) - E(\text{hBN}) - E(\text{water})$, where E(hBN-water), E(hBN), E(water) are the energies of the hBN-water dimer, the hBN, and the water molecule computed by the RPA method.

3.3.2 Error Control in RPA

The RPA procedure has a few well-defined approximations. The approximations include errors due to incomplete basis sets, finite lattice constant along the z-axis, the non-zero water coverage, finite supercell, and finite k-points.

We checked the basis set convergence by increasing the plane wave energy cutoff. Using an energy cutoff of 600 eV for the plane wave and 400eV for the response function leads to a difference of about 1 meV in the interaction energy. We checked the convergence of the lattice constant along the z-axis by increasing it to 20 Å and the change in interaction energy is less than 1 meV. We varied parameters like the Gaussian smearing width and self-consistent energy tolerance, and the change in interaction energy is less than 0.1 meV. The interaction energies computed varying the plane wave cutoff, lattice constance along the z-axis,

the Gaussian smearing width, and the self-consistent energy tolerance are summarized in Table 3.1.

We also checked the convergence of k-points by systematically computing the interaction using a series of k-grids. The convergence of exchange energy and the correlation energy is considered separately, as shown in Fig. 3.5. We found that the exchange energy has a weak dependence on k-grid, while the dependence of correlation energy is strong. The correlation energy converges at a 4×4 k-grid for a 2×2 supercell, and increasing the k-grid to 8×8 leads to a difference of less than 1 meV. We checked the convergence of the supercell and the water coverage density by increasing the supercell size while keeping the equivalent k-point mesh the same. The results are summarized in Fig. 3.5. We found that the exchange energy has a strong dependence on the supercell size and water coverage density, while the dependence of correlation energy is weak. The exchange energy converges at a 8×8 supercell, and increasing the k-grid to 16×16 leads to a difference of less than 1 meV. Considering all approximations, we estimate the error to be less than 2 meV on the interaction energy computed by the RPA method.

Table 3.1: The interaction energy between a single water molecule and hBN computed using plane wave cutoff ECUT, self-consistent loop break energy tolerance EDIFF, Gaussian smearing width SIGMA, and lattice constant perpendicular to the hBN plane ZBOX. The response function cutoff uses 2/3 of the plane wave cutoff. The hBN is represented by a 2×2 supercell with Brillouin zone sampled by a 2×2 k-mesh. The oxygen atom of the water molecule is separated from the hBN plane by 3.6 Å. The system with the water oxygen separated from the hBN plane by 7 Å is considered as the zero energy reference. The parameters ECUT, EDIFF, SIGMA, and ZBOX are changed one at a time. The exchange energy ΔE_{exx}, the correlation energy ΔE_{c}, and the total RPA energy ΔE_{rpa} are reported. The energy computed at the DFT-PBE level, ΔE_{pbe}, is included for comparison.

	ΔE_{pbe} (meV)	ΔE_{exx} (meV)	ΔE_{c} (meV)	ΔE_{rpa} (meV)
Default	-15.86	44.42	-86.97	-42.55
ECUT=600 eV	-14.71	44.32	-87.88	-43.56
EDIFF=10^{-7}	-15.86	44.43	-86.97	-42.54
EDIFF=10^{-6}	-15.86		-86.98	
SIGMA=0.2	-15.86	44.42	-86.97	-42.55
SIGMA=0.01	-15.86	44.42	-86.97	-42.55
ZBOX=20 Å	-15.53	45.38	-87.51	-42.13

3.3.3 Comparison with DMC

We then evaluate the performance of the RPA method in describing the interaction between hBN and water by comparing to the DMC method. Three different water orientations were considered for which the DMC calculations have been performed [13, 14]. Both the DMC and RPA results are summarized in Fig. 3.6. Close agreement between RPA and DMC is observed for all the three water orientations. The RPA method can predict both the potential well depth and the well position as accurately as the DMC calculations for this system. The RPA method is also able to capture the difference in the interaction energy when the water

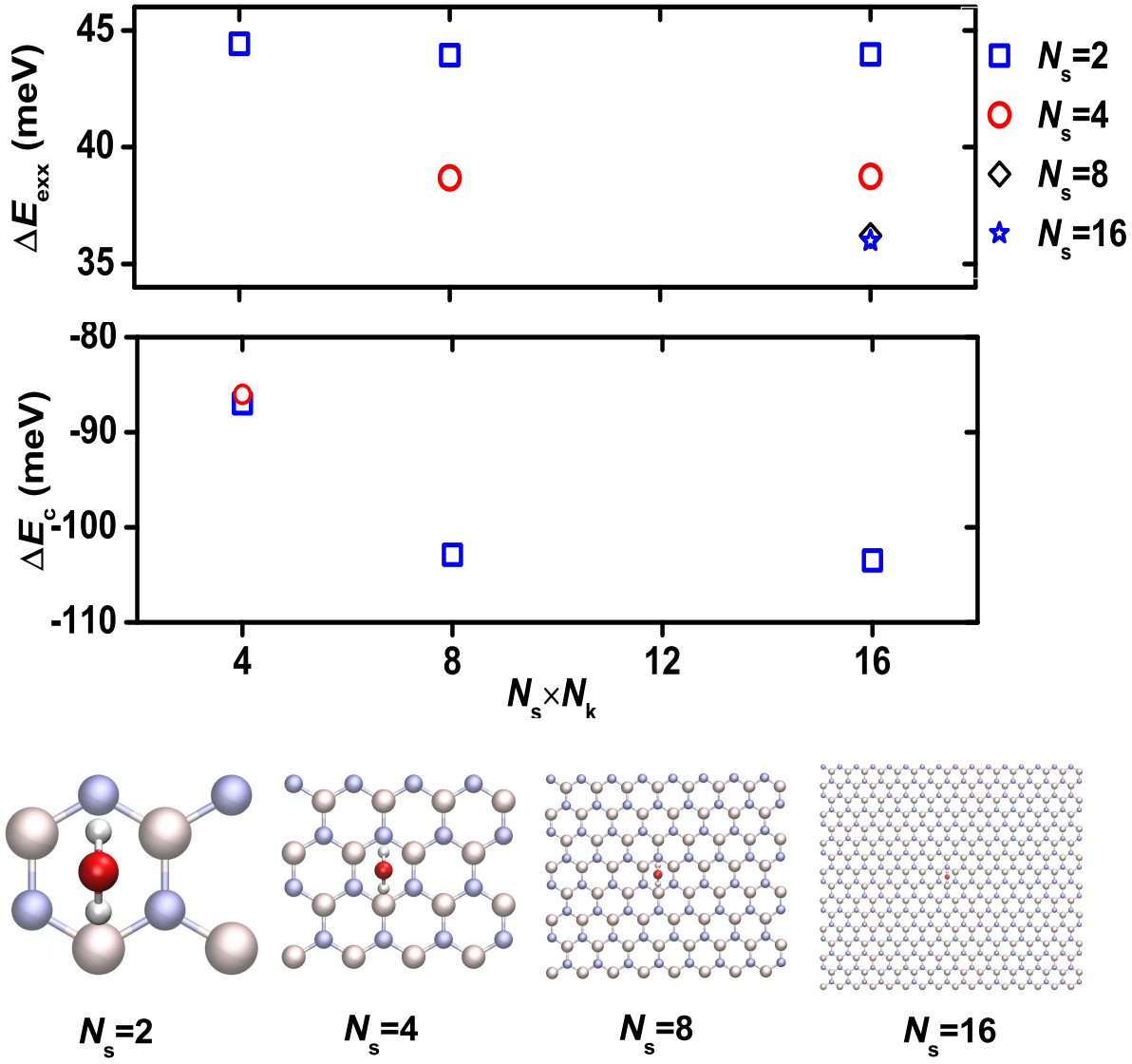

Figure 3.5: The interaction energy between a single water molecule and hBN represented by $N_\mathrm{s} \times N_\mathrm{s} \times 1$ supercell with Brillouin zone sampled by a $N_\mathrm{k} \times N_\mathrm{k} \times 1$ k-mesh. The energy is computed using the random phase approximation (RPA) method. The two components, the exchange energy, ΔE_exx, and the correlation energy, ΔE_c, are converged separately.

orientation changes. Since the accuracy of the RPA method is comparable to the DMC method, we use the RPA method to explore the potential energy surface between hBN and water in order to develop hBN-water non-bonded interaction models for use in MD simulations.

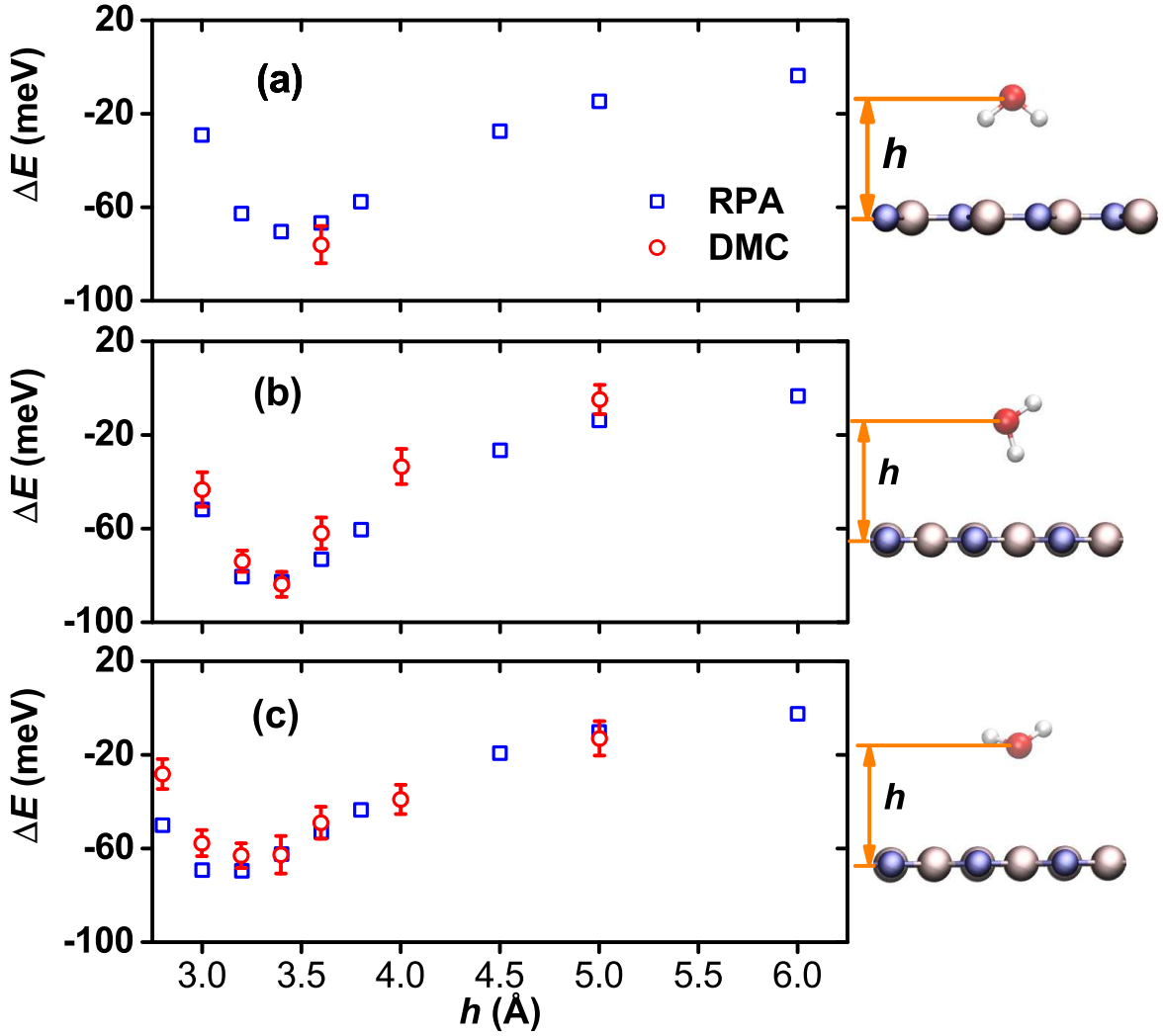

Figure 3.6: The interaction energies between hBN and water for three different water orientations. The results by diffusion Monte Carlo (DMC) [13, 14] are included for comparison.

3.4 MP2 Calculations

3.4.1 System Setup

The BN molecules considered in MP2 follow the formula $B_{3n^2}N_{3n^2}H_{6n}$ (n=1,2,3...). The B-N bond length and B-N-B, N-B-N bond angle are set to the experimental values for h-BN [91]. The B-H and N-H bond length are optimized by DFT with B3LYP functional for $B_3N_3H_6$ and the same values are used for larger BN molecules. The spin-component-scaled (SCS) technique [103] is used to correct the overestimation of the binding energy as computed from standard MP2 method. The MP2 calculations were performed with the Gaussian package [104]. For $B_3N_3H_6$ and water, the Dunning's correlation consistent basis set aug-cc-pVTZ

[89] is used. For BN molecules with $n > 1$, aug-cc-pVTZ basis set was used for water and B/N atoms in the hexagon ring beneath the water molecule, and aug-cc-pVDZ basis set was used for the rest of B/N atoms and termination H atoms. We checked larger basis sets and found negligible change in the results (see below).

In extrapolating from BN molecules to h-BN monolayer, the interacting energy is decomposed into two parts which are extrapolated separately. One part includes the electrostatic interaction component, which is extrapolated following the approach by Jenness et al. implemented for graphene [2]: The electrostatic component between water and BN molecules is represented by the interaction between electron multipole moments of BN molecules and water. The multipole moments, including atomic charge, dipole, and quadrupoles, on each atom in the BN molecule are computed using the Stone's Gaussian distributed multipole analysis (GDMA) tool [105] based on MP2/cc-pVDZ charge densities. The multipole moments of the central B/N atoms in $B_{48}N_{48}H_{24}$ are used as the moments for atoms in the h-BN monolayer. The moments of water are represented by the three point charges from the Dang-Chang model [106].

The remaining part includes dispersion, repulsion, and induction energy components. The dispersion, repulsion and induction energies are extrapolated together as one term E_{fast}. The E_{fast} of $B_{3n^2}N_{3n^2}H_{6n}$ is extrapolated from that of $B_{3m^2}N_{3m^2}H_{6m}$ $(m < n)$ following the formula:

$$E_{\text{fast}}(n) = E_{\text{fast}}(m) - C_6^{\text{O-B/N}} \sum_{\text{i=outer B/N}} 1/R_{i\text{O}}^6 + C_6^{\text{O-H}} \sum_{\text{j=H}} 1/R_{j\text{O}}^6(m) - C_6^{\text{O-H}} \sum_{\text{k=H}} 1/R_{k\text{O}}^6(n) \qquad (3.2)$$

where the first term on the right is computed by subtracting the electrostatic energy component from the interaction energy for $B_{3m^2}N_{3m^2}H_{6m}$, the second term accounts for interaction between water and the additional B/N atoms in $B_{3n^2}N_{3n^2}H_{6n}$ compared to $B_{3m^2}N_{3m^2}H_{6m}$, the third term is the dispersion energy between water and termination hydrogen atoms in $B_{3m^2}N_{3m^2}H_{6m}$, and the final term is the dispersion energy between water and termination hydrogen atoms in $B_{3n^2}N_{3n^2}H_{6n}$. For h-BN, the final term is zero. The $C_6^{\text{O-B/N}}$ parameters were taken from Ref [15] with the ϵ parameters scaled to reproduce $[E_{\text{fast}} + C_6^{\text{O-H}} \sum_{\text{j=H}} 1/R_{j\text{O}}^6(m)]$ for $B_{3m^2}N_{3m^2}H_{6m}$. The $C_6^{\text{O-H}}$ parameters were taken from Ref [107]. $m = 2$ was used in this work. $m = 3$ was done as well and shows the same results as $m = 2$.

The interaction energy between water and h-BN monolayer is then computed by summing the two parts.

3.4.2 Error Control in MP2

We categorize errors into approximations in the MP2 calculations and errors in the energy decomposition and extrapolation. The errors in the MP2 calculations include errors due to the incomplete basis set and neglecting the perturbative corrections higher than the 2nd order in the MP2 method. The errors in the

energy decomposition and extrapolation include the errors due to the incomplete basis set, C_6^{ij} values, finite molecule size, and neglecting the higher-order coupled interaction during energy decomposition.

We checked the error due to the incomplete basis set in MP2 calculations by comparing to results using a larger basis set. In computing interaction energies for $B_3N_3H_6$, aug-cc-pVQZ basis was used for $B_3N_3H_6$. The change is less than 4 meV. In computing interaction energies for $B_{12}N_{12}H_{12}$ (where $n = 2$), aug-cc-pVTZ basis was used for all B/N/O/H atoms. The change is around 1.6 meV. Considering that the contribution to interaction energy is less for B/N atoms away from water, we expect the error due to the incomplete basis set to be less than 2 meV for BN molecules with $n > 2$. We checked the error due to neglecting the perturbative corrections higher than the 2nd order in the MP2 method by comparing to CCST(D)/CBS in predicting $B_3N_3H_6$-water interaction energy. The energy predicted by MP2 differs from CCSD(T)/CBS by less than 7 meV. Considering all the errors in the MP2 calculations, the error in the interaction energy between water and BN molecules is around 4 meV. The interaction energies between water and BN molecules with $n < 4$ from MP2 are summarized in Fig. 3.7(a).

We also estimated the errors in the energy decomposition and extrapolation. We checked the error due to the incomplete basis set in computing the electrostatic energy component by using a larger basis, the aug-cc-pVTZ basis. The change is less than 5 meV. We checked the error in C_6^{ij} values by comparing to results using different C_6^{ij} values in the literature. For $C_6^{\text{O-B/N}}$, using a different value [17] leads to a difference of less than 4 meV. For $C_6^{\text{O-H}}$, using different values [108, 109] leads to a difference of less than 1 meV. We checked the convergence of atomic multipole moments of B/N atoms on molecular size by plotting the multipole moments on atoms in BN molecules against their number of bonds from hydrogen, as shown in Fig. 3.8. The atomic charge, dipole, and quadrupole moments all converge to a constant value for atoms several bonds aways from hydrogen. We checked the error due to neglecting the higher-order coupled interaction during energy decomposition by comparing the extrapolated result with MP2 calculation. The interaction energy between water and $B_{27}N_{27}H_{18}$ is extrapolated to -74 meV, which differs from direct MP2 calculations by less than 1 meV. We checked the convergence of extrapolated energies between water and h-BN monolayer on the size of the BN molecule used in extrapolation. The extrapolated interaction energy using $B_{27}N_{27}H_{18}$ ($n = 3$) differs by less than 1 meV from that using $B_{12}N_{12}H_{12}$ ($n = 2$), as shown in Fig. 3.7(b). Considering all the errors, the binding energy between a single water molecule and h-BN monolayer is estimated as -74$\pm$7 meV by MP2.

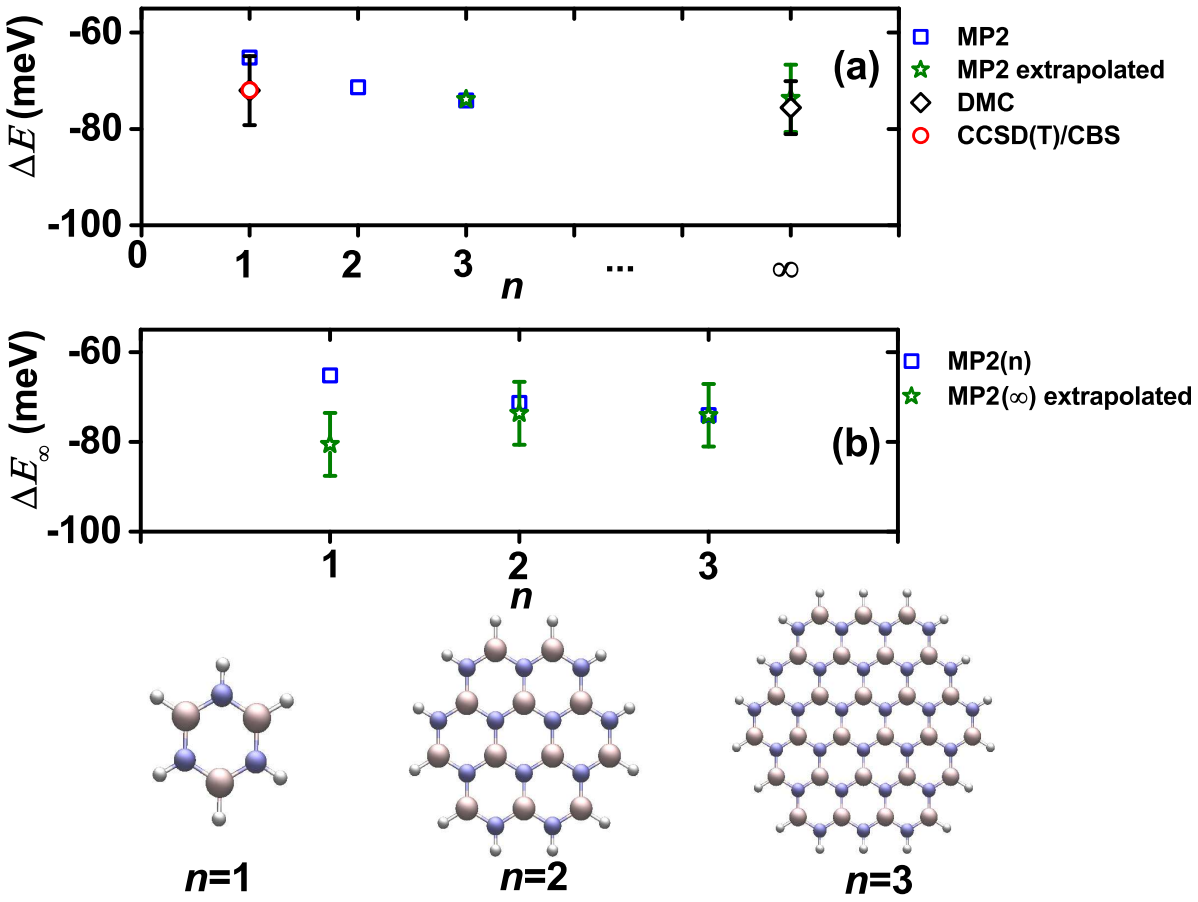

Figure 3.7: (a) Interaction energies, ΔE, between water and BN molecules computed by the second-order Møller-Plesset perturbation theory (MP2) method. The extrapolated MP2 energies at larger molecules and monolayer are included as well. The BN molecules follow the formula $B_{3n^2}N_{3n^2}H_{6n}$. The BN molecules approach h-BN monolayer when $n \to \infty$. The interaction energy computed by coupled cluster method with single and double excitations and perturbative triples at complete basis set limit (CCSD(T)/CBS), and diffusion Monte Carlo (DMC) are included as well for comparison. (b) The extrapolated interaction energies ΔE_∞ between water and the BN monolayer based on the MP2 energies of BN molecules of size n. The MP2 energies of BN molecules of size n are included for comparison.

3.4.3 Comparison with DMC

The binding energy estimated by MP2 is in good agreement with that of DMC for both the BN molecule and the h-BN monolayer. As a relatively efficient method to capture the non-bonded interaction, MP2 can be used to compute the interaction energy for multiple configurations. B/N-water force field parameters can be developed by fitting to the MP2 energies [110], which can be used in atomistic simulation to study larger systems [86].

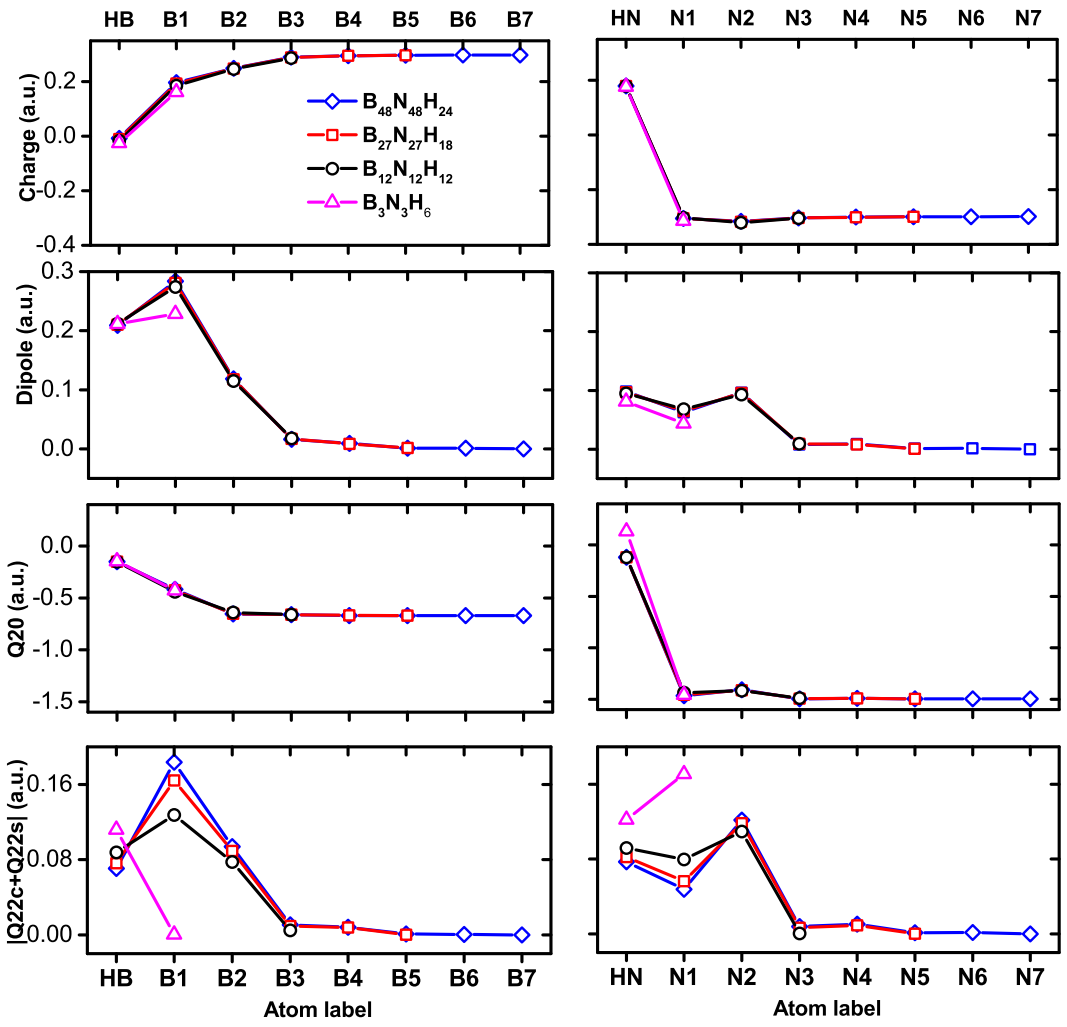

Figure 3.8: The multipole moments up to quadruple moments of atoms. The atoms are labeled according to their number of bonds from terminating hydrogen. The multipole moments are computed using the Stone's Gaussian distributed multipole analysis (GDMA) methods with electron density from the MP2/pVDZ.

3.5 Parameter Fitting

The interaction between water and hBN in MD is modeled by the electrostatic interaction ΔE_{el} and the vdW interaction ΔE_{vdW}:

$$\begin{aligned} \Delta E &= \Delta E_{\text{el}} + \Delta E_{\text{vdW}} \\ \Delta E_{\text{el}} &= \sum_{i \in \text{hBN}} \sum_{j \in \text{water}} \frac{q_i q_j}{r_{ij}} \\ \Delta E_{\text{vdW}} &= \sum_{i \in \text{hBN}} \sum_{j \in \text{water}} 4\epsilon_{ij} \left[\left(\frac{\sigma_{ij}}{r_{ij}} \right)^{12} - \left(\frac{\sigma_{ij}}{r_{ij}} \right)^{6} \right] \end{aligned} \tag{3.3}$$

where r_{ij} is the distance between atom i and atom j, q_i and q_j are the partial charges of atom i and atom j, ϵ_{ij} is the depth of the potential well of vdW interaction between the two atoms, and $2^{1/6}\sigma_{ij}$ is the position of the potential well. The atomic partial charges for water are taken from the TIP4P water model [111]. The partial charges for B/N atoms, $q_{\mathrm{B}}/q_{\mathrm{N}}$ are computed by fitting to the electrostatic potential from the 2nd-order Møller-Plesset perturbation (MP2) theory [13] calculation. The ϵ_{ij} and σ_{ij} are obtained by fitting to the RPA data. For the interaction between water (which has O and H atoms) and hBN (which has B and N atoms), there are four pairs of ϵ_{ij} and σ_{ij} parameters, in total eight parameters to fit. In practice, the number of the fitting parameters can be reduced.

One common approach to reduce the number of parameters is to make the vdW interaction between H and B/N zero and put the vdW center of the water molecule on the oxygen atom, assuming that the vdW interaction due to oxygen dominates over hydrogen. We test this assumption by plotting the vdW interaction energies (the RPA interaction energy with electrostatic interaction excluded) against the position of the oxygen atom in Fig. 3.9(a), considering various water orientations. Deviation in the vdW interaction energy is observed for water with the same oxygen position but different orientations. The deviation implies that putting the vdW center on the oxygen atom is not appropriate. The vdW center should be shifted from the oxygen atom to minimize the deviation.

We pick the vdW center located on the bisector of the $\angle$HOH and shifted by 0.15 Å away from the oxygen atom towards the hydrogen atoms (point M in Fig. 3.9). The vdW interaction energy is then plotted against the position of M in Fig. 3.9(b). We see that the deviation in the vdW interaction is minimized by choosing M as the vdW center for water. The deviation in the medium distance region (3.8 Å to 6 Å) and the repulsive region ($<$ 3 Å) is minimal. The positions of the potential wells for different water orientations are similar, while the depths of the potential well vary by less than 10 meV. So putting the vdW center at point M is appropriate, compared to putting the center at oxygen. Shifting the center from the oxygen atom is physical, given that the ratio between the valence electrons of the two hydrogen atoms and those of the oxygen atom is not close to zero. Shifting the vdW center by 0.15 Å reduces implementation difficulty, given that the virtual site of the TIP4P water model is located at the same position. Any simulation package that supports TIP4P water model supports the parameters proposed here with no or minor implementation effort (the example files for using the parameters in the GROMACS and the LAMMPS packages are provided in Ref [112]). With the deviation minimized, it is appropriate to consider one vdW site for water and simplify

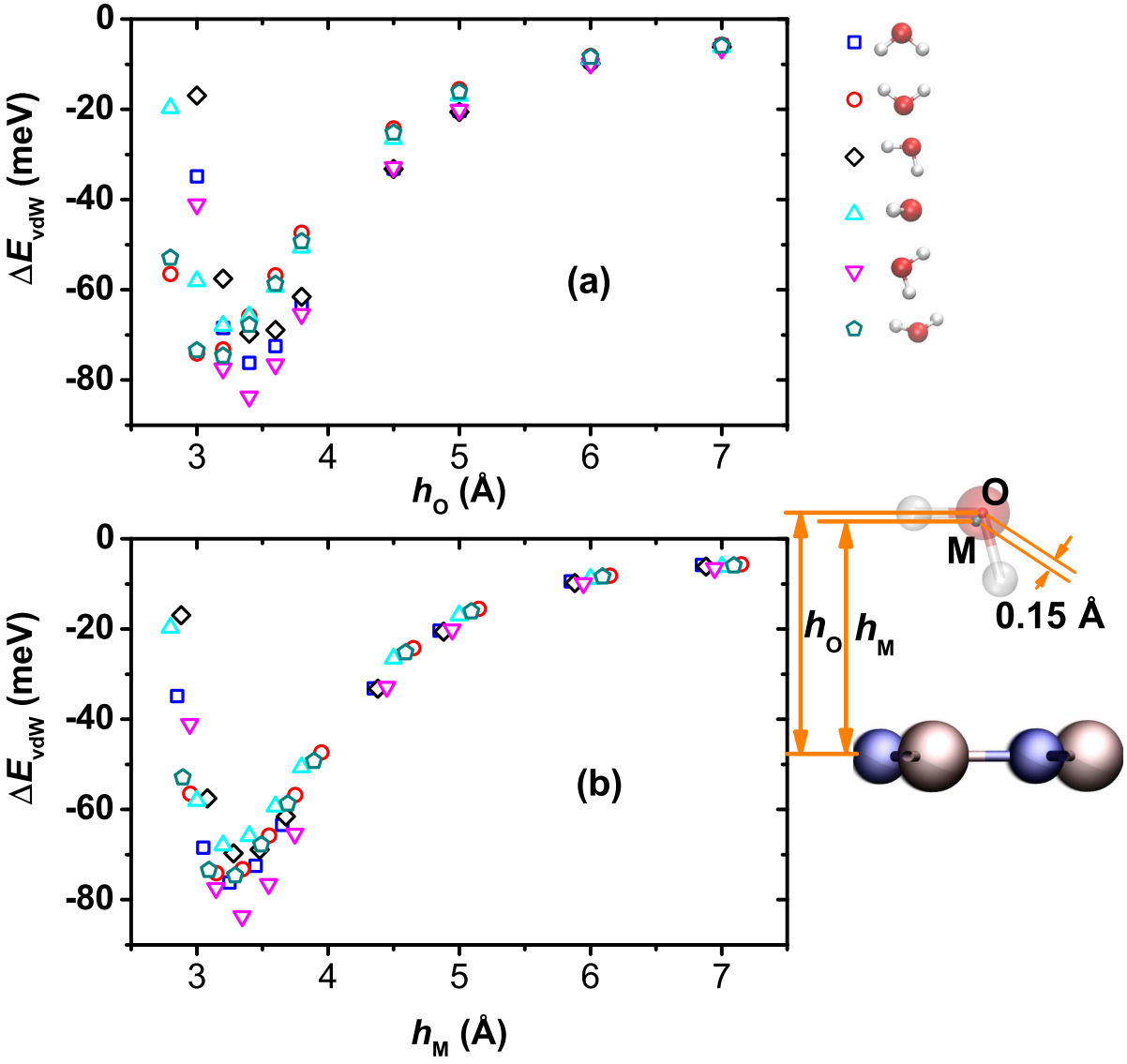

Figure 3.9: The vdW interaction energies between hBN and water for six different water orientations. The point M is located at the bisector of HOH angle, as shown in the inset figure.

the $\Delta E_{\rm vdW}$ as

$$\begin{aligned}\Delta E_{\rm vdW} = &\sum_{i\in \rm B} 4\epsilon_{\rm BM}\left[\left(\frac{\sigma_{\rm BM}}{r_{i\rm M}}\right)^{12} - \left(\frac{\sigma_{\rm BM}}{r_{i\rm M}}\right)^{6}\right] \\ &+ \sum_{i\in \rm N} 4\epsilon_{\rm NM}\left[\left(\frac{\sigma_{\rm NM}}{r_{i\rm M}}\right)^{12} - \left(\frac{\sigma_{\rm NM}}{r_{i\rm M}}\right)^{6}\right]\end{aligned} \tag{3.4}$$

where $\epsilon_{\rm BM}$, $\sigma_{\rm BM}$, $\epsilon_{\rm NM}$, and $\sigma_{\rm NM}$ are the four parameters to fit to the RPA data.

The parameters are obtained by fitting to the Boltzmann averaged vdW interaction energies among different water orientations, as shown in Fig. 3.10. The least squares fit was used. The parameters are

summarized in Table A.2. The TIP4P water model [111] should be used with the parameters. The TIP4P water model has been shown [110, 113, 114] to predict comparable water liquid-vapor surface tension as the SPC/E [115] and TIP5P [116] models. Also included in the table are force field parameters from the literature [15, 17, 16] and the water models used in their work. The accuracy of different parameters can be evaluated by predicting properties using MD simulations and comparing to experimental measurements.

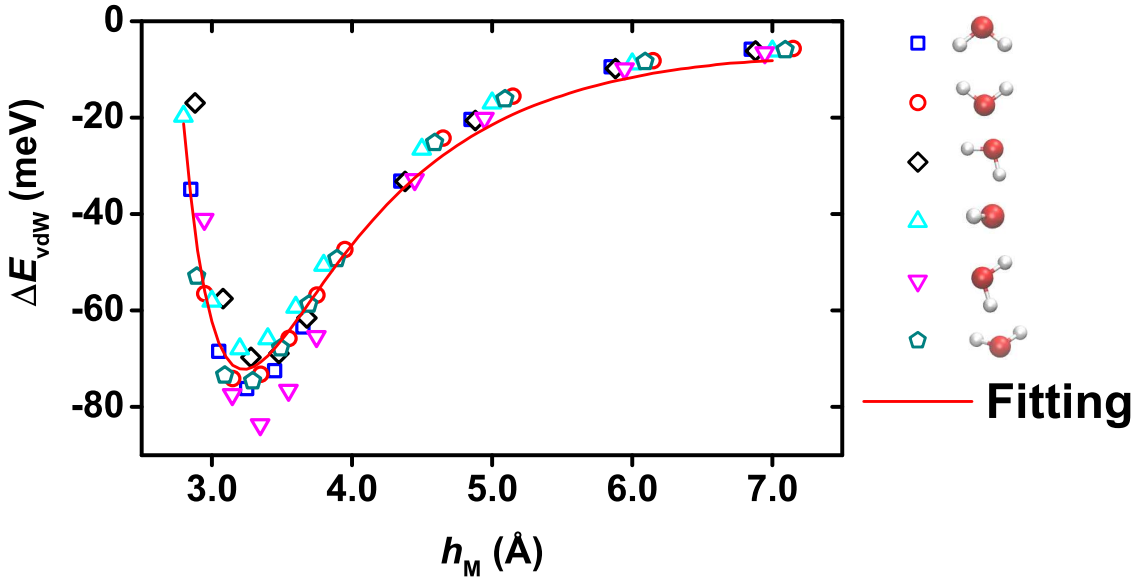

Figure 3.10: Fitting to the Boltzmann averaged RPA van der Waals (vdW) interaction among different water orientations using the Lennard-Jones 6-12 model.

3.6 Comparison with Experiments

Water contact angle on bulk hBN has been reported by multiple experimental groups [117, 118, 119] and rigorously studied with minimal surface contamination [117, 11]. The contact angle values reported in experiments are in the range of 40° to 55°. The contact angle is then simulated using MD following the procedure by Werder et al. [20, 110]. The bulk hBN surface is represented by four layers of hBN sheets with an interlayer distance of 3.33 Å. The dimension of each hBN layer is about 20 nm × 20 nm, or 30 nm × 30 nm, depending on the droplet size to effectively remove the interaction between the droplet and its periodic images. The bulk hBN surface is fixed throughout the simulation [20]. The simulation box size perpendicular to the hBN surface plane is 20 nm. The MD simulations were performed with GROMACS 4.5.3 package [64]. Time integration is performed using the leap-frog algorithm [65] with a time step of 2.0 fs. The short-range vdW interactions are computed using a cutoff scheme (cutoff distance, 1.4 nm). The

long-range electrostatic interactions are computed by using a particle mesh Ewald method (real space cutoff, 1.4 nm; FFT grid spacing, 0.12 nm, fourth-order interpolation). The Nosé-Hoover thermostat [66, 67] with a time constant of 0.5 ps is used to maintain the temperature at 300K. A water cubic box is initially placed on top of the hBN surface. The system is equilibrated for 6 ns using NVT ensemble, during which the water cubic box evolves into a spherical shape. The energy and temperature of the system reach constant values during this equilibration process. The resulting configuration is used as the starting point for further simulations on data collection. For collecting sufficient statistics to compute contact angles, the simulations were run for 4 ns.

The contact angle values for nano-droplets obtained from MD, θ, are extrapolated to that of macroscopic droplet, θ_∞, as shown in Fig. 3.11(a), following the modified Young's equation, so that a direct comparison between MD and experiments is possible:

$$\cos\theta = \cos\theta_\infty - \frac{\tau}{\gamma_{\mathrm{LV}}} r_{\mathrm{B}}^{-1} \tag{3.5}$$

where γ_{LV} is the water liquid-vapor surface tension, r_{B} is the droplet base radius, and τ is the line tension. The comparison of contact angle values between MD and experiments is shown in Fig. 3.11(b). The parameters obtained using combinational rule by Won and Aluru [15] slightly underestimate the contact angle, while the parameters obtained using combinational rule by Gordillo and Martí [16] strongly underestimate the contact angle. The parameters developed by fitting to the DFT-D data by Hilder et al. [17] strongly underestimate the contact angle since the DFT-D method overestimates the hBN-water binding energy [13]. The parameters obtained by fitting to the RPA data in this work, with no adjustable parameter or no fit from experimental data, are able to predict the water contact angle in excellent agreement with experimental measurements. The agreement shows that the multiscale approach in describing weak interactions between molecules and solid, all the way from DMC and coupled cluster, with approximations well controlled in each level up, to accurately predicting macroscopic properties, is a feasible path.

3.7 Summary

In summary, a combination of high-level theoretical electronic structure approaches was used to study the interaction between hBN and water, as shown in Fig. 3.12. The DMC and CCSD(T) methods benchmark each other at the molecular level. DMC was used to validate RPA and MP2 calculations. Then we used the RPA method to compute the potential energy surface between hBN and water. We developed force field parameters based on the RPA data with no fitting to experiments. The parameters are able to predict water

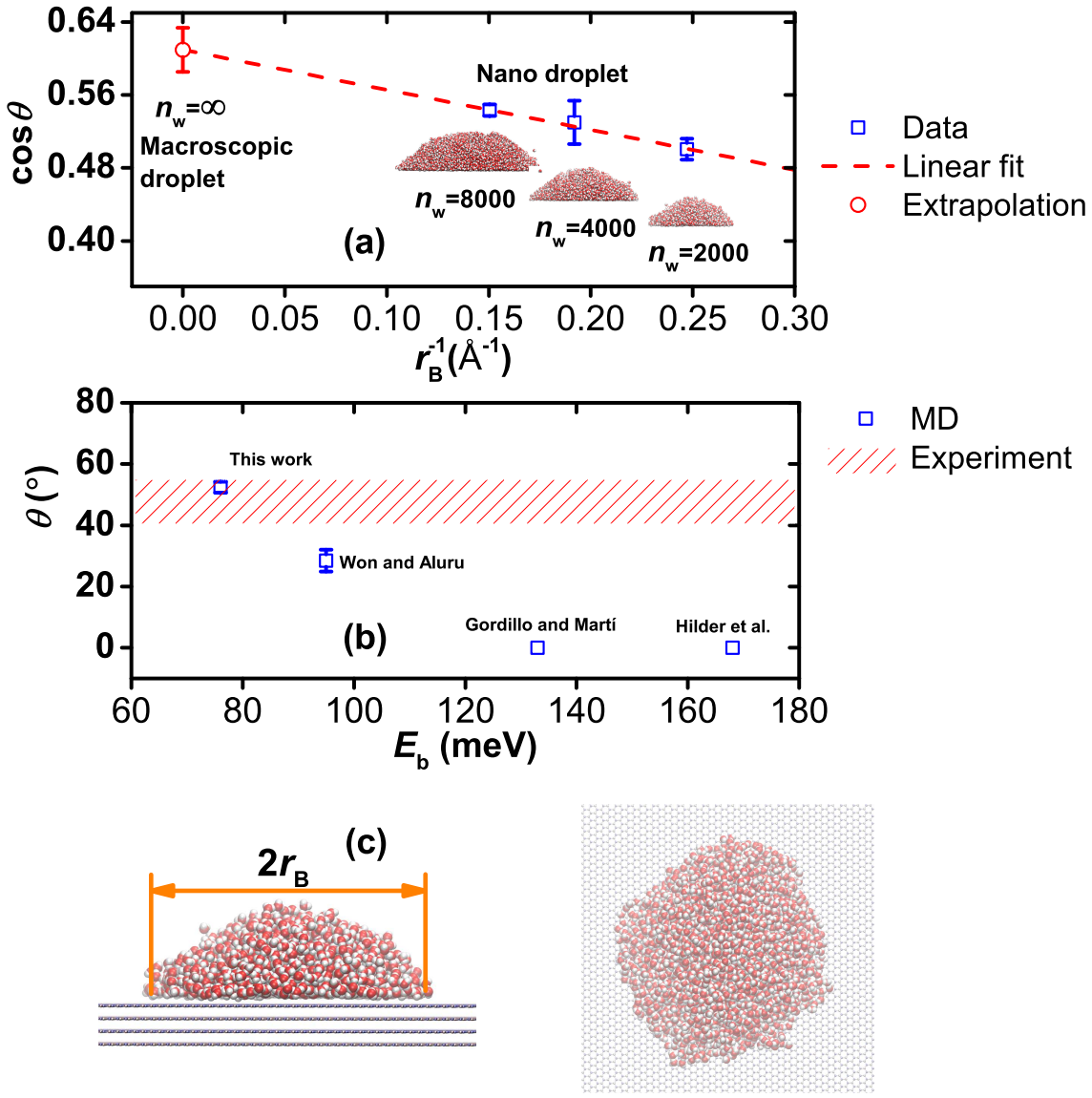

Figure 3.11: (a) The contact angle, θ, of nano water droplets on bulk hBN predicted by molecular dynamics (MD) simulations. Three nano droplets composed of n_w=2000, 4000, or 8000 water molecules are considered. An extrapolation of θ to the contact angle of the macroscopic droplet ($n_w = \infty$), θ_∞, is performed. (b) The binding energy between water and hBN monolayer, E_b, and contact angle values predicted using water-hBN force field parameters developed by Won and Aluru [15], Gordillo and Martí [16], Hilder et al. [17] and from this work. (c) The side and top view of the configuration used in the simulations.

contact angle on hBN in excellent agreement with experimental measurements. The agreement shows that it is feasible to develop accurate force field parameters for the hBN-water interaction entirely from first-principle calculations. The multiscale approach all the way from diffusion Monte Carlo or coupled cluster to predicting macroscopic properties is extended from molecular interactions [120] to molecule-solid interaction in this work. For future work, we would like to apply this approach to water interaction with other two

dimensional materials like graphene and molybdenum disulfide. Also we would like to apply this approach to BNNT to see whether the curvature in the tube leads to different force field parameters.

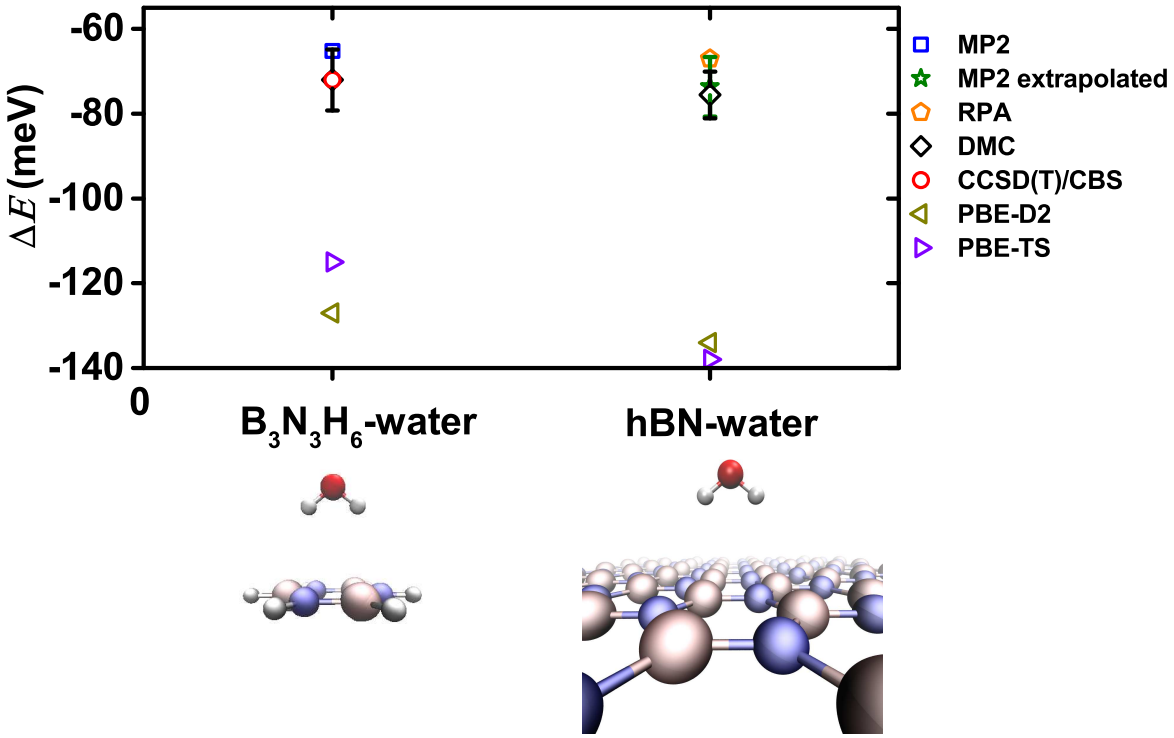

Figure 3.12: Interaction energies, ΔE, between a single water molecule and $B_3N_3H_6$ or hBN monolayer computed by the second-order Møller-Plesset perturbation theory (MP2), random phase approximation (RPA), diffusion Monte Carlo (DMC), coupled cluster method with single and double excitations and perturbative triples at complete basis set limit (CCSD(T)/CBS), and the density functional theory with dispersion correction (DFT-D). Two DFT-D schemes, PBE-D2 following Grimme's protocol [18] and PBE-TS following Tkatchenko and Scheffler's protocol [19], are considered.

Chapter 4

Graphitic Carbon and Water Interaction Parameters

In this chapter, we extend the combined approach to the study of the interaction between graphene and water: The DMC and CCSD(T) methods benchmark each other at the molecular level. DMC is used to validate RPA calculations, then we use the RPA method to compute the potential energy surface between graphene and water. For graphene and water system, we also observe that DMC and RPA obtain indistinguishable results, so we develop force field parameters based on the RPA data with no fitting to experiments. The parameters are then validated by predicting water contact angle on graphite and comparing to experimental measurements. We show that the force field parameters developed based on the first-principle calculations are able to predict the contact angle of water in close agreement with experiments. This again demonstrates a multiscale approach that extends from detailed high accuracy diffusion Monte Carlo to macroscopic properties of a molecular-solid interaction. The parameters obtained by fitting to MP2 calculations and *ab initio* data from the literature are also included for comparison.

4.1 CCSD(T) Calculations

The CCSD(T) method with complete basis set (CBS) [93, 94] is computed by:

$$\begin{aligned} \Delta E^{\mathrm{CCSD(T)/CBS}} &= \Delta E^{\mathrm{MP2/CBS}} + (\Delta E^{\mathrm{CCSD(T)}} - \Delta E^{\mathrm{MP2}})_{\text{small basis}} \\ \Delta E^{\mathrm{MP2/CBS}} &= E^{\mathrm{HF}}_{\mathrm{CBS}} + E^{\mathrm{corr}}_{\mathrm{CBS}} \end{aligned} \tag{4.1}$$

where $\Delta E^{\mathrm{CCSD(T)/CBS}}$ and $\Delta E^{\mathrm{MP2/CBS}}$ are the interaction energy evaluated using CCSD(T) and MP2 with complete basis set, $(\Delta E^{\mathrm{CCSD(T)}} - \Delta E^{\mathrm{MP2}})_{\text{small basis}}$ is the difference of the interaction energies evaluated using CCSD(T) and MP2 with a small basis set, E^{HF} and E^{corr} are Hartree-Fork and 2nd-order correction component of standard MP2 calculations, and $E^{\mathrm{HF}}_{\mathrm{CBS}}$ and $E^{\mathrm{corr}}_{\mathrm{CBS}}$ are the CBS extrapolation based on $E^{\mathrm{HF}}_{X} = E^{\mathrm{HF}}_{\mathrm{CBS}} + A\exp(-1.63X)$ and $E^{\mathrm{corr}}_{X} = E^{\mathrm{corr}}_{\mathrm{CBS}} + BX^{-3}$ using Dunning's correlation consistent basis set aug-cc-pVXZ (X=T,Q) [89]. The small basis set used in Eq. 4.1 is 6-31G(d=0.25) [95]. All MP2 and CCSD(T) calculations are done using Gaussian [92]. The results for CCSD(T) calculations are summarized in Fig. 4.1.

4.2 DMC Calculations

4.2.1 System Setup

The DFT calculations were performed with the PBE functional using the Crystal 2009 [96]. Energy-consistent pseudopotentials were used [97] with correction for hydrogen atoms [98]. A triple-zeta basis set with reduced diffuse coefficient was used to obtain convergence in DFT, and a k-point mesh equivalent to a 24×24×1 mesh on the primitive cell of graphene was used. One water molecule per 2×2 graphene supercell was considered. The water monomer is set to the experimental gas phase geometry [90], and C-C bond length and C-C-C bond angles are set to the experimental values for graphene [121]. The variational Monte Carlo (VMC) and DMC calculations were performed using QWalk [99].

4.2.2 Error Control in DMC and Comparison to CCSD(T)

The DMC procedure has a few well-defined approximations. We categorize errors due to the approximations into methodological errors and systematic errors. The methodological errors include errors due to the fixed-node approximation and pseudo potential.

We checked the methodological approximations by comparing to coupled cluster calculations with single and double excitations and perturbative triples in the complete basis set limit (CCSD(T)/CBS) [94]. We used the C_6H_6-water system as a proxy in which all errors could be controlled. The C_6H_6-water interaction energies as a function of the separation distance h are summarized in Fig. 4.1. Both DMC and CCSD(T)/CBS predict that the energy minimum in the distance scan is when $h = 3.36$ Å. The binding energies calculated by DMC and CCSD(T)/CBS agree within stochastic uncertainty. The agreement between DMC and CCSD(T)/CBS is also good in the medium separation distance range (4-6 Å) and repulsive region (< 3.2 Å). From these tests, it appears that the fixed node and pseudopotential approximations do not strongly affect the interaction energy of water with C_6H_6. Assuming that these errors translate to the water-graphene system, we expect the errors due to these approximations to be minimal.

The DMC calculations of graphene-water interaction are still in progress. For the purpose of verifying other methods in calculating graphene-water interaction energies, the DMC results by Ma et al. [55] will be used.

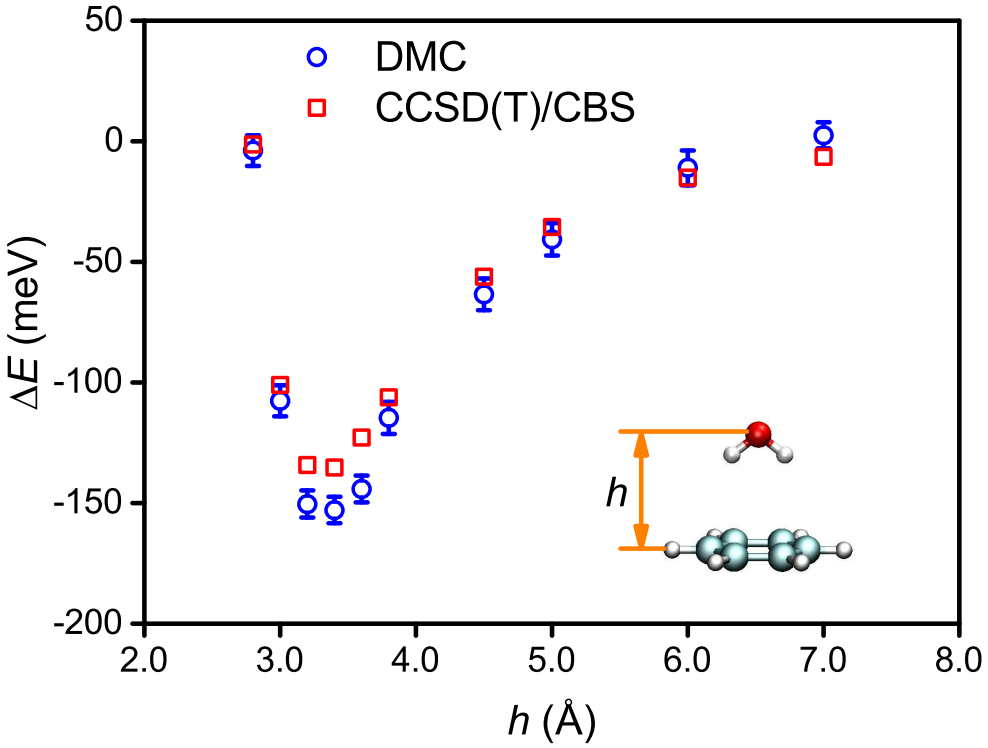

Figure 4.1: C_6H_6-water interaction energies calculated by the diffusion Monte Carlo (DMC) and coupled cluster method with single and double excitations and perturbative triples at complete basis set limit (CCSD(T)/CBS). The configuration of C_6H_6 and water separated by 7 Å is used as the zero-reference-energy configuration. The energies predicted using the DMC method are in good agreement with those calculated using the CCSD(T)/CBS within the error bars.

4.3 RPA Calculations

4.3.1 System Setup

The RPA calculations were performed using the VASP package [100, 101], projector-augmented wave potentials, and an energy cutoff of 408 eV. The response function was expanded in plane waves up to an energy cutoff of 272 eV. The exchange energy and correlation energy are computed separately with different graphene supercell sizes and Brillouin zone sampling Monkhorst-Pack k-meshes [102]: A 8×8 supercell with a 2×2 k-mesh was used for the exchange energy, and a 2×2 supercell with a 8×8 k-mesh for the correlation energy. A lattice constant of 20 Å along the direction perpendicular to the graphene surface (z-axis) was used. The potential energy surface between graphene and water was computed using the RPA method by varying the separation distance and orientation of the water molecule with respect to the graphene surface. For simplicity, the graphene and the water molecule internal geometry were fixed while changing their rela-

tive position: The C-C bond length and C-C-C bond angle are set to the experimental values for graphene [121], and the water monomer is set to the experimental gas phase geometry [90]. The interaction energy between water and graphene, ΔE, is computed by $\Delta E = E(\text{graphene-water}) - E(\text{graphene}) - E(\text{water})$, where E(graphene-water), E(graphene), E(water) are the energies of the graphene-water dimer, the graphene, and the water molecule computed by the RPA method.

4.3.2 Error Control in RPA

The RPA procedure has a few well-defined approximations. The approximations include errors due to incomplete basis sets, finite lattice constant along the z-axis, the non-zero water coverage, finite supercell, and finite k-points.

We checked the basis set convergence by increasing the plane wave energy cutoff. Using an energy cutoff of 600 eV for the plane wave and 400eV for the response function leads to a difference of about 1 meV in the interaction energy. We checked the convergence of the lattice constant along the z-axis by increasing it to 25 Å and the change in interaction energy is less than 1 meV. We varied parameters like the Gaussian smearing width and self-consistent energy tolerance, and the change in interaction energy is less than 0.2 meV.

We also checked the convergence of k-points by systematically computing the interaction using a series of k-grids. The convergence of exchange energy and the correlation energy is considered separately, as shown in Fig. 4.2. We found that the exchange energy has a weak dependence on k-grid, while the dependence of correlation energy is strong. The correlation energy converges at a 4×4 k-grid for a 2×2 supercell, and increasing the k-grid to 8×8 leads to a difference of less than 1 meV. We checked the convergence of the supercell and the water coverage density by increasing the supercell size while keeping the equivalent k-point mesh the same. The results are summarized in Fig. 4.2. We found that the exchange energy has a strong dependence on the supercell size and water coverage density, while the dependence of correlation energy is weak. The exchange energy converges at a 8×8 supercell, and increasing the k-grid to 16×16 leads to a difference of less than 1 meV. Considering all approximations, we estimate the error to be less than 2 meV on the interaction energy computed by the RPA method.

4.3.3 Comparison with DMC

We then evaluate the performance of the RPA method in describing the interaction between graphene and water by comparing to the DMC method. The binding energy between graphene and water for the water orientation in Fig. 4.2 is computed by RPA as -93 meV. The binding energy computed by DMC for the

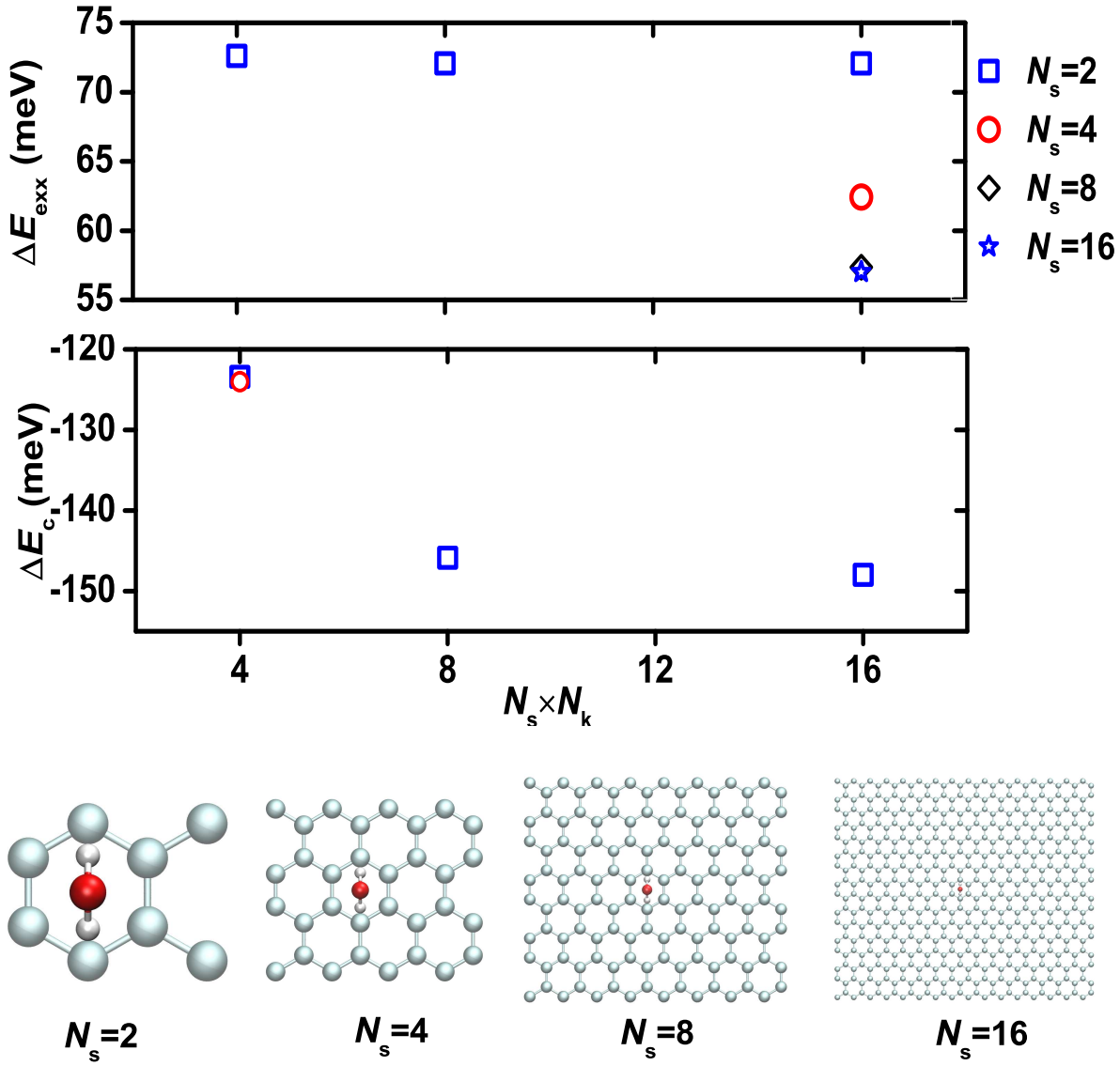

Figure 4.2: The interaction energy between a single water molecule and graphene represented by $N_\mathrm{s} \times N_\mathrm{s} \times 1$ supercell with Brillouin zone sampled by a $N_\mathrm{k} \times N_\mathrm{k} \times 1$ k-mesh. The energy is computed using the random phase approximation (RPA) method. The two components, the exchange energy, ΔE_exx, and the correlation energy, ΔE_c, are converged separately.

same configuration is -90 ± 10 meV [55]. Close agreement between RPA and DMC is observed for this water orientation. Since the accuracy of the RPA method is comparable to the DMC method, we use the RPA method to explore the potential energy surface between graphene and water in order to develop graphene-water non-bonded interaction models for use in MD simulations.

4.4 MP2 Calculations

MP2 investigation of graphene-water systems have been performed in the literature. MP2 method has been shown to be adequate to capture inter-molecular binding energies for small molecules [122]. This method was used by Sudiarta et al. [3] and Lago [1] to compute the graphene-water interaction energy. The results of Sudiarta et al. [3] were questioned [123] due to the use of a small basis set (6-31G(d=0.25)), which is inadequate to describe polarization and dispersion interactions. Lago [1] extrapolated the graphene-water interaction energies based on the energies obtained for polycyclic aromatic hydrocarbons (with the number of carbons considered less than or equal to 54) by assuming an exponential decay. It has been shown [3, 2] that due to the long-range electrostatic multipole interaction, the convergence of the interaction energy for a cluster of 54 carbons is not adequate for an exponential decay. Proper decomposition of the interaction energy has to be done before the extrapolation. We will re-do the MP2 calculations with proper consideration of these effects.

4.4.1 System Setup

The infinite graphene is represented by the extrapolation of a series of increasing-size polycyclic aromatic hydrocarbon (PAH) clusters, as shown in Fig. 4.3(a)-1(e). The C-C bond length and C-C-C bond angle (1.42 Å and 120°) in all clusters follow the experimental values for graphite [124]. The dangling bonds at the edge are terminated by hydrogen atoms, with C-H bond length of 1.09 Å and C-C-H bond angle of 120°. The water monomer follows the experimental gas phase geometry, with O-H bond length of 0.9572 Å and H-O-H angle of 104.52° [90]. Three water orientations with respect to PAH clusters are considered: (a) Downwards orientation: the water molecule is located above the center of the PAH cluster, with two hydrogens pointing to the PAH and dipole perpendicular to PAH molecular plane, as shown in Fig. 4.3(f). (b) Upwards orientation: the water molecule is located above the center of the PAH cluster, with two hydrogens pointing away from the PAH and dipole perpendicular to PAH molecular plane, as shown in Fig. 4.3(f). (c) Pointing orientation: one O-H bond is pointing towards one carbon atom of the PAH cluster, and the other O-H bond is almost parallel to the PAH plane [55], as shown in Fig. 4.3(f). The distance between water oxygen and PAH plane is defined as h.

4.4.2 MP2 Results and Error Control

The interaction energies for C_6H_6-water and $C_{14}H_{10}$-water system for a separation distance of 3.36 Å with the downwards water orientation are computed as -3.06 kcal/mol and -3.05 kcal/mol by MP2/6-311+G(3d,3p),

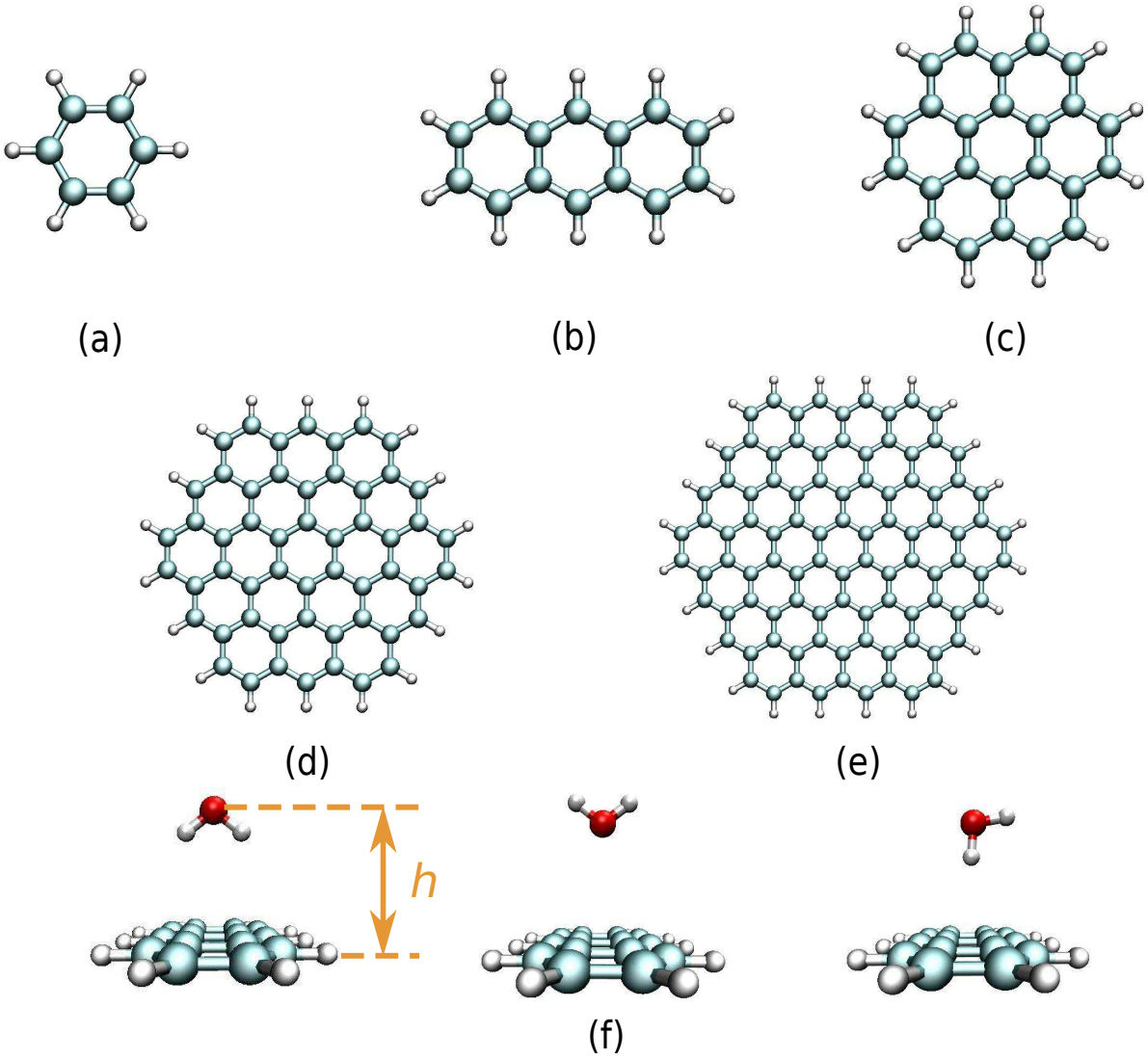

Figure 4.3: (a)-(e) polycyclic aromatic hydrocarbon (PAH) considered in ab initio calculations. (a) C_6H_6, benzene; (b) $C_{14}H_{10}$, anthracene; (c) $C_{24}H_{12}$, coronene; (d) $C_{54}H_{18}$, circumcoronene; (e) $C_{96}H_{24}$, dicircumcoronene. (f) Three water configurations with respect to PAH considered in ab initio calculations. From left to right: downwards, upwards and pointing. Detailed description of each configuration can be found in the methods section. The distance between water oxygen and PAH plane is defined as h.

compared to -3.24 kcal/mol and -3.18 kcal/mol by CCSD(T)/CBS method. This shows that MP2/6-311+G(3d,3p) method can give a good estimate of the interaction between PAH and water with accuracy comparable to CCSD(T) method. So MP2/6-311+G(3d,3p) is used to compute interaction energies on bigger clusters $C_{24}H_{12}$, $C_{54}H_{18}$ and $C_{96}H_{24}$.

The values computed in this work and their comparison to values reported in the literature are summarized in Table 4.1. The interaction energies computed by MP2/6-311+G(3d,3p) agree with those reported by Lago et al. [1] using MP2/pVTZ method and compare well with those reported using other methods in

the literature.

Table 4.1: Interaction energies between polycyclic aromatic hydrocarbon (PAH) and water. All energies are in kcal/mol. The water molecule is located above the center of the PAH cluster, with two hydrogens pointing to the PAH and dipole perpendicular to PAH molecular plane. The water oxygen atom is 3.36 Å from the PAH plane. a: CCSD(T) with complete basis set (CBS). b: The value is corrected from original −3.098 kcal/mol [1] by excluding electrostatic multipole interaction before extrapolation. c: spin-component-scaled MP2 (SCS-MP2). d: Density-functional/coupled-cluster (DFT/CC) theory. e: The value is obtained from original −3.18 kcal/mol [2] by considering that the graphene carbon quadrupole-water interaction is negligible [3]. f: DFT-based symmetry-adapted perturbation theory (DFT-SAPT). g: Random-phase approximation (RPA). h: Diffusion Monte Carlo (DMC).

Reference	C_6H_6	$C_{14}H_{10}$	$C_{24}H_{12}$	$C_{54}H_{18}$	$C_{96}H_{24}$	Graphene	Approach
This work	-3.24	-3.18					CCSD(T)/CBS[a]
This work	-3.06	-3.05	-3.22	-3.11	-3.05	-2.51	MP2/6-311+G(3d,3p)
Lago et al. [1]	-2.72	-3.11	-3.15	-3.05		-2.50[b]	SCS-MP2/pVTZ[c]
Rubes et al. [125]	-3.15		-3.54	-3.51		-3.18	DFT/CC(aVQZ)[d]
Jenness et al. [2]	-3.16		-3.05	-2.93		-2.27[e]	DFT-SAPT/aVTZ[f]
Sudiarta et al. [3]	-2.55		-2.81	-2.80		-2.39	MP2/6-31G(d=0.25)
Voloshina et al. [126]						-2.84	CCSD(T)/pVDZ
Ma et al. [55]						-2.26	RPA[g]
Ma et al. [55]						-2.08±0.23	DMC[h]

4.4.3 MP2 Interaction Energy Decomposition and Extrapolation

Before extrapolating the interaction energies between PAH and water to infinite graphene limit, the effects of PAH cluster boundary have to be considered: the C-H dipole created by termination hydrogen atoms contributes to electrostatic interaction between PAH and water. So the total interaction energy is decomposed into the following components [3, 2]

$$\Delta E = \Delta E_{\mathrm{ES}} + \Delta E_{\mathrm{R}} + \Delta E_{\mathrm{CORR}} + \Delta E_{\mathrm{I}} \tag{4.2}$$

where ΔE_{ES}, ΔE_{R}, ΔE_{CORR} and ΔE_{I} are the electrostatic, repulsion, correlation and induction energy components, respectively. The electrostatic energy component can be further decomposed into contributions from charge penetration [127] and from interactions between atom-centered multipole moments [2]. The electrostatic energy component between multipole moments of PAH and water is long-ranged and it includes the extra electrostatic interaction mentioned above. Since the electrostatic energy component between multipole moments of graphene and water is negligible [3], the electrostatic energy component between multipole moments of PAH and water are subtracted from the total interaction energy before the extrapolation is done.

The atomic charges, dipoles, and quadrupoles on each PAH atom are computed using Stone's Gaussian distributed multipole analysis (GDMA) tool [105] based on MP2/cc-pVDZ charge densities. The small basis

set cc-pVDZ is used here since the calculated multipole moments by GDMA converge rapidly to stable values at small basis sets [105, 2]. The contribution from the electron moments higher than quadrupole is negligible and thus not considered in the multipole analysis. The three point charges from Dang-Chang model [106] are used to represent the electron moments of water. The use of the Dang-Chang model was well justified by comparing to distributed multipole analysis results [2]. The computed electrostatic multipole energy components for different PAH-water dimer are summarized in Table 4.2. These values agree with those reported by Jenness et al. [2]

Table 4.2: Electrostatic multipole component is subtracted from the total interaction energy before extrapolation. All the energies are in kcal/mol. The water molecule is located above the center of the polycyclic aromatic hydrocarbon (PAH) cluster, with two hydrogens pointing to the PAH and dipole perpendicular to PAH molecular plane. The water oxygen atom is 3.36 Å from the PAH plane.

	C_6H_6	$C_{24}H_{12}$	$C_{54}H_{18}$	$C_{96}H_{24}$	Graphene
Total interaction energy	-3.06	-3.22	-3.11	-3.05	-2.51
Electrostatic multipole component	-1.80	-1.11	-0.71	-0.57	0.00
Remaining energy component	-1.26	-2.12	-2.40	-2.48	-2.51

The electrostatic component due to charge penetration is short-ranged and converges when the cluster is larger than $C_{24}H_{12}$ molecule. The repulsion component is also short-ranged and it converges when the size of the cluster is larger than the $C_{54}H_{18}$ molecule [2]. The addition of the repulsion and charge-penetration electrostatic components can be represented by the C_n/R_{ij}^n term in Eq. 2.17. The induction energy represents the non-negligible polarization [128] of water and PAH when they approach each other. Both the induction and correlation components vary as $1/R^6$, where R is the separation distance between PAH atoms and water atoms [3]. The addition of the induction and correlation components can be represented by the $-C_6/R_{ij}^6$ term in Eq. 2.17. The C_n and C_6 coefficients are obtained by fitting to $C_{54}H_{18}$-water energy profiles. The interaction energy for clusters larger than $C_{54}H_{18}$ is then extrapolated using the obtained fitting parameters.

4.4.4 Graphene-water Interaction Energy Calculated using Fitted Parameters

Using the fitting parameters from $C_{54}H_{18}$-water MP2 energy profile, the interaction energy between larger cluster and water can be extrapolated. The extrapolated interaction energy between $C_{96}H_{24}$ and water, with the electrostatic multipole component excluded, is -2.487 kcal/mol, compared to -2.478 kcal/mol computed by MP2 and GDMA technique. This confirms that the extrapolation based on $C_{54}H_{18}$-water energy profile is capable of capturing larger cluster and water interaction. The graphene-water interaction is extrapolated as -2.51 kcal/mol and this compares well with the literature values. Also the electrostatic multipole component between $C_{96}H_{24}$ and water is -0.57 kcal/mol, which is far from the converged value of close to zero for

graphene-water dimer. The electrostatic multipole component using only atomic quadropoles on carbon atoms is −0.29 kcal/mol for $C_{216}H_{36}$, and −0.14 kcal/mol for $C_{600}H_{60}$. So the energy decomposition for clusters smaller than $C_{96}H_{24}$ is necessary before extrapolation. If the same energy decomposition is done for the MP2 energy reported by Lago et al. [1], the resulting graphene-water interaction energy is −2.50 kcal/mol, which agrees with the value from this work.

4.5 Parameter Fitting

4.5.1 Fitting to RPA Potential Surface

Similar to hBN, shifting the vdW center by 0.15 Å also minimizes the deviation of interaction energy with water orientation. It seems that shifting the vdW center from oxygen is universal. The fitted values are $\sigma_{\text{C-M}} = 3.2678$ Å and $\epsilon_{\text{C-M}}$=0.1249 kcal/mol.

4.5.2 Fitting to MP2 Data and Ab Initio Data from the Literature

The interaction energy between graphene and water depends on water orientation. Voloshina et al. [126] found that the lowest interaction energy for upwards orientation is 0.35 kcal/mol higher than that for downwards orientation using CCSD(T)/pVDZ, while Rubes et al. [125] reported 1.10 kcal/mol energy difference using DFT/CC(aVQZ). Such water-orientation dependence can be included in the fitting potential by having non-zero carbon-water hydrogen interaction parameters $\epsilon_{\text{C-HW}}$ and $\sigma_{\text{C-HW}}$. $\sigma_{\text{C-OW}}$ and $\sigma_{\text{C-HW}}$ are reduced to one fitting parameter α by $\sigma_{\text{C-OW}} = \alpha\sigma^0_{\text{C-OW}}$ and $\sigma_{\text{C-HW}} = \alpha\sigma^0_{\text{C-HW}}$. The initial guess of $\sigma^0_{\text{C-OW}} = 3.296$ Å and $\sigma^0_{\text{C-HW}} = 2.584$ Å is directly taken from Neria et al. [129]. The *ab initio* data considered here include the data from the MP2/6-311+G(3d,3p) and the data from DFT-SAPT [2], CCSD(T)/pVDZ [126], and RPA [55] available in the literature. The MP2/6-311+G(3d,3p) data set includes the $C_{54}H_{18}$-water interaction energies for downwards orientation at a series of h, with electrostatic multipole component excluded. The DFT-SAPT data set includes the $C_{42}H_{18}$-water interaction energies for downwards orientation at a series of h, with electrostatic multipole component excluded[2]. Since spin-scaled-MP2 methods are only optimized close to the equilibrated geometries, the methods tend to predict energies having appreciable difference compared to CCSD/CBS method for configurations far away from equilibrated geometry [1]. So the energy difference of 0.35 kcal/mol between downwards and upwards orientations and equilibrated separation distance of 3.06 Å for upwards orientation obtained from CCSD(T) calculation [126] are included in the MP2 data series to capture the water-orientation-dependence effects. The same treatment is done for DFT-SAPT data series as well. The CCSD data set consists of the graphene-water interaction energies at a

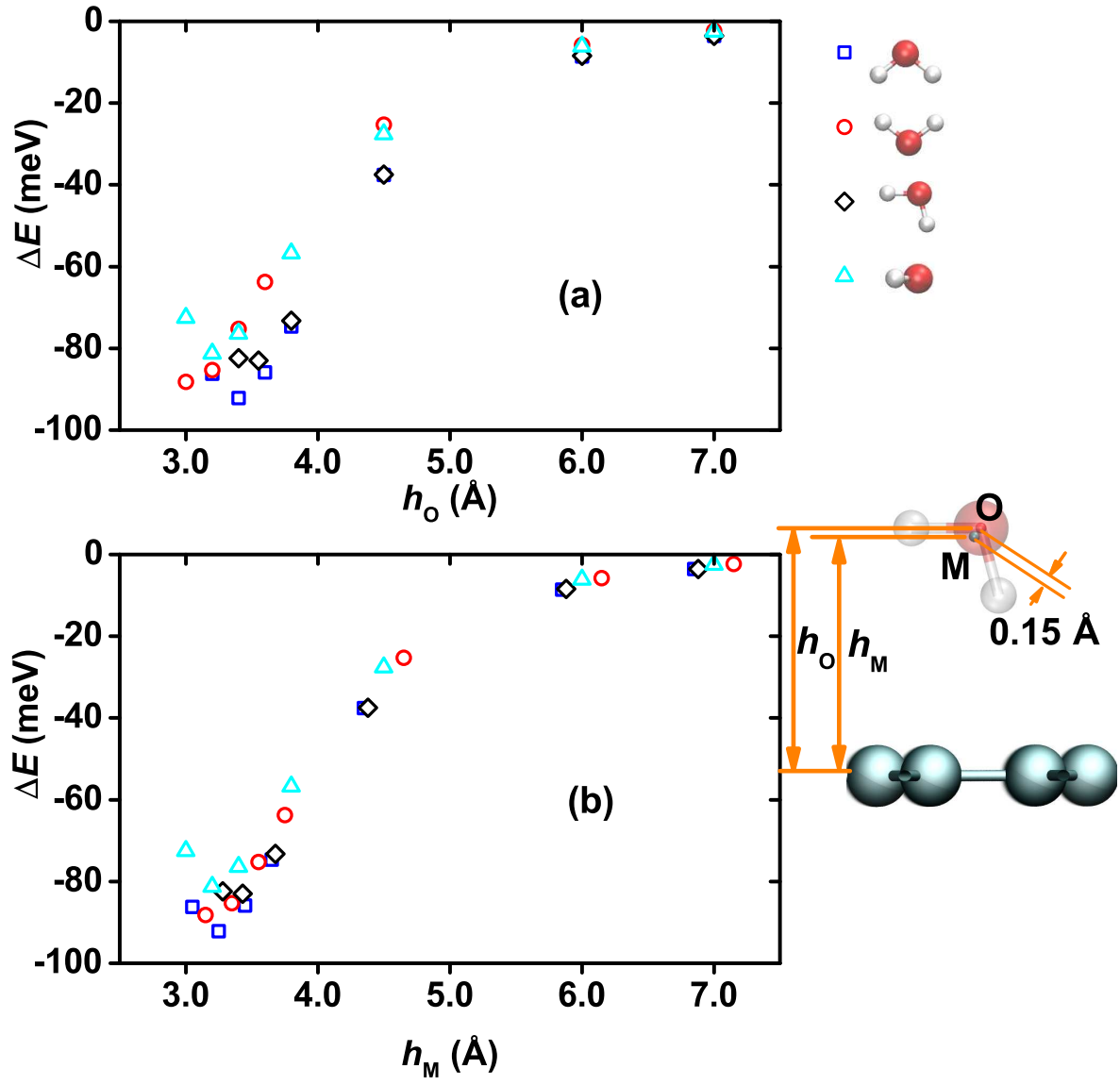

Figure 4.4: The vdW interaction energies between graphene and water for six different water orientations. The point M is located at the bisector of HOH angle, as shown in the inset figure.

series of h for upwards orientation, the binding energy of 2.84 kcal/mol and equilibrated separation distance of 3.2 Å for downwards orientation [55]. The RPA data set contains the graphene-water interaction energies at a series of h for both downwards and pointing orientation [55]. We didn't do the fitting to the DMC data [55] since the DMC data have big error bars and are not converged on k-points.

The fitting is done using nonlinear least square fitting technique using trust-region-reflective algorithm in Matlab®(2007a, The MathWorks, Natick, MA.). The fitted parameters for each *ab initio* data are summarized in Table A.1. The function form used is the LJ6-12 form. Fig. 4.5 shows the *ab initio* data

and the fitted curve on the same plot. All the interaction parameters based on *ab initio* data tend to predict stronger carbon-water interaction. The same trend has been reported by DFT-Born-Oppenheimer MD simulation of water confined between graphene sheets and in CNT [130] and vdW density functional study of water-CNT systems [131].

Three different function forms, namely LJ6-10, LJ6-12 and LJ6-14, are considered. These functions are fitted to the RPA *ab initio* data, as shown in Fig. 4.5(b). The resulting fitting parameters are summarized in Table A.1. All the three function forms give a good representation of the RPA *ab initio* data. The effect of various fitting function forms will be further investigated by predicting contact angle using the three sets of parameters.

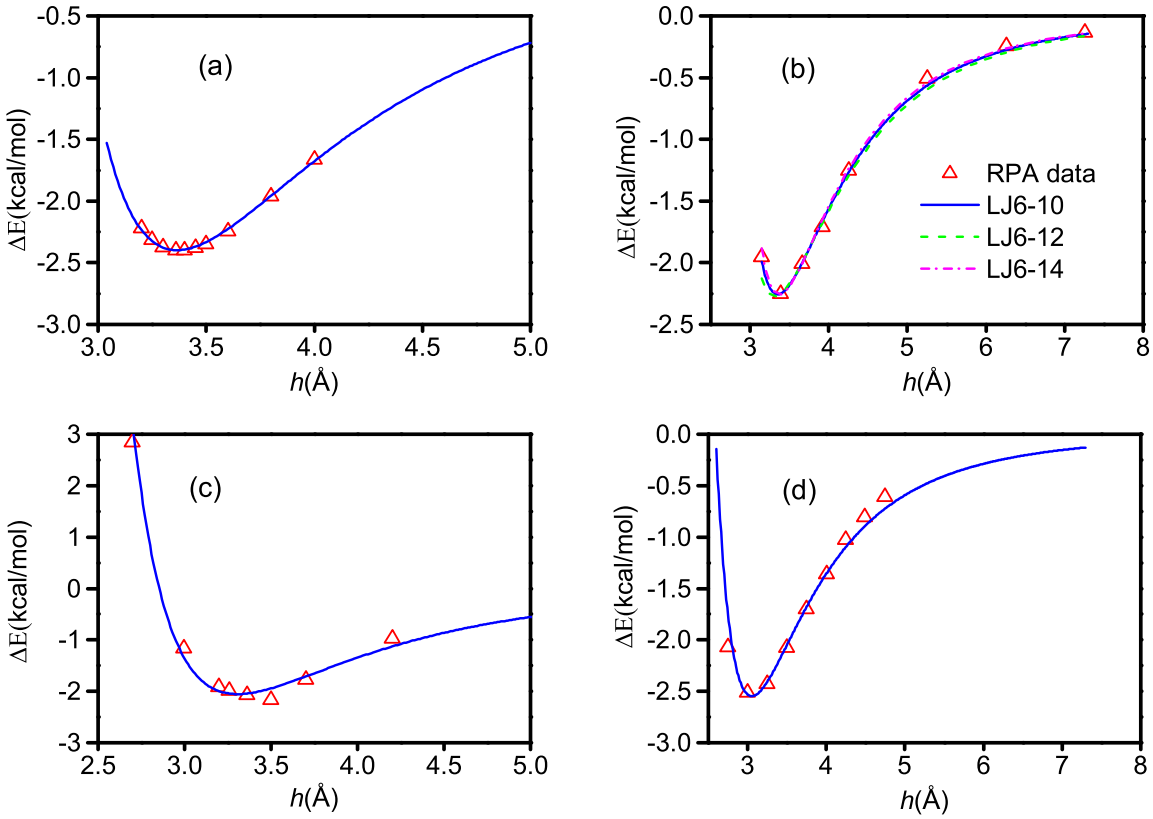

Figure 4.5: LJ function forms fit to (a) MP2 (b) RPA (c) DFT-SAPT (d) CCSD(T). The *ab initio* data are represented by triangles and the LJ6-n fitting curves are represented by lines in each plot. h is the distance between water oxygen and PAH plane. In (b), three LJ6-n function forms are fitted to the RPA data.

4.6 Comparison with Experiments

4.6.1 Contact Angle Calculations using MD

The graphite is represented by two layers of graphene sheets with an interlayer distance of 3.4 Å. The dimension of each graphene layer is about 20 nm × 20 nm, or 30 nm × 30 nm, depending on the droplet size to effectively remove the interaction between the droplet and its periodic images. The graphite surface is fixed throughout the simulation [20]. The simulation box size perpendicular to the graphite surface plane is 20 nm. The MD simulations were performed with GROMACS 4.5.3 package [64]. Time integration is performed using the leap-frog algorithm [65] with a time step of 2.0 fs. The short-range vdW interactions are computed using a cutoff scheme (cutoff distance, 1.4 nm). The long-range electrostatic interactions are computed by using a particle mesh Ewald method (real space cutoff, 1.4 nm; FFT grid spacing, 0.12 nm, fourth-order interpolation). The Nosé-Hoover thermostat [66, 67] with a time constant of 0.5 ps is used to maintain the temperature at 300K. A water cubic box is initially placed on top of the graphite surface. The system is equilibrated for 6 ns using NVT ensemble, during which the water cubic box evolves into a spherical shape. The energy and temperature of the system reach constant values during this equilibration process. The resulting configuration is used as the starting point for further simulations on data collection. For collecting sufficient statistics to compute contact angles, the simulations were run for 4 ns.

Water contact angles on graphite surface are predicted using the carbon-water interaction parameters developed in this work and compared with experimental measurements. Various procedures [20, 132, 133, 134] exist to measure contact angles using MD. It has been shown that the contact angle values measured by the nano-droplet procedure [20] agree with those by the cylindrical filament procedure [48] or by measuring individual surface tensions and computing contact angles using Young's equation [134]. We follow the most commonly used nano-droplet procedure as outlined in Werder et al. [20] to compute the nano-droplet contact angles from water density profile. 60,000 time frames are used to get the density profile of the equilibrated water droplet. The macroscopic contact angle θ_∞ is related to the nano-droplet contact angle θ (measured using MD) using the modified Young's equation [135], $\cos\theta = \cos\theta_\infty - \frac{\tau}{\gamma_{\mathrm{LV}}}\frac{1}{r_{\mathrm{B}}}$, where r_{B} is the radius of the contact area of water on graphite, τ is the line tension and γ_{LV} is the surface energy of liquid water. Such dependence of contact angles on water droplet size has been verified recently by Scocchi et al. [48], on condition that the number of water molecules forming the nano-droplet is larger than 2000. The extrapolation of the nano-droplet contact angles to obtain the macroscopic contact angle is checked for the carbon-water interaction parameters used by Werder et al. [20] and for the interaction parameters obtained from the RPA data. The mean and standard deviation of contact angles are obtained from three simulation

runs with different initial velocity configurations. $\cos\theta$ values are plotted against the reciprocal of r_B in Fig. 4.6 and Fig. 4.7. We note that, $\cos\theta$ has a linear relation with $1/r_B$. The linear least square fitting is done to compute θ_∞, and the contact angle error bar associated with each nano-droplet size is propagated to θ_∞ following the procedure by Taylor [87]. The contact angle difference between the macroscopic droplet and the nano-droplet consisting of 2000 water molecules is 4.3±1.0° for the parameters used by Werder et al. [20], and 6.0±3.6° for the parameters obtained from the RPA *ab initio* data. From these results, we can infer that the contact angle value of a nano-droplet consisting of 2000 water molecules is a good representation of macroscopic contact angle. Since this observation is valid for both carbon-water interaction parameter sets, and for the contact angle ranges of 30-40° and 80-90°, we believe that this holds for other carbon-water interaction parameters considered in this work. In order to reduce the computational cost, except for the force fields obtained from the MP2 and CCSD(T) energies, we use the contact angle values of the droplet consisting of 2000 water molecules to represent the macroscopic contact angle. The same simplification has been used by Scocchi et al. [48] for graphene-water systems, Zangi et al. [136] for graphite-water systems, and Cruz-Chu et al. [137] for silica-water systems. For the force fields obtained from the MP2 and CCSD(T) energies, which predict contact angles less than 20°, droplets consisting of 16000 water molecules are used.

The dependence of contact angle on simulation parameters, e.g. LJ cutoff length, is studied. Sendner et al. [134] computed water contact angle on carbon diamond-like surface by measuring individual surface tensions using MD and LJ cutoff length was found to influence the contact angle, especially for small contact angles. The LJ cutoff length used was in the range of 0.8 nm to 1.4 nm. So proper contact angle dependence on LJ cutoff length has to be studied. Here we measure the contact angle of the droplet consisting of 2000 water molecules for carbon-water interaction parameters used by Werder et al. [20] and obtained from the RPA *ab initio* data, using LJ cutoff length of 1.0 nm, 1.4 nm and 1.8 nm. The resulting contact angle values are summarized in Fig. 4.6(b). The contact angle difference between cutoff length of 1.4 nm and 1.8 nm is 3.3±1.0° for parameters by Werder et al. [20], and 2.8±3.6° for parameters obtained from the RPA data. For both cases, the difference is comparable to the error bar, implying that the contact angle is reasonably accurate for a cutoff length of 1.4 nm.

We also study various fitting function forms by considering three different functions, LJ6-10, LJ6-12 and LJ6-14. These functions are fitted to the RPA *ab initio* data. The resulting fitting parameters are summarized in Table 4.3. The corresponding contact angles in Fig. 4.6(c). The error bar of 3.5° is used for all three data points. We note that the function form doesn't influence the predicted contact angles as long as the fitted potential can represent the *ab initio* data well. Hence, the LJ6-12 function form is used since LJ6-12 form is the function form that is commonly used in the literature for molecular dynamics simulations.

Table 4.3: Fitting to RPA ab initio data with three LJ function forms following Eq. 2.17. $R_{v\text{C-OW}}$ and $D_{v\text{C-OW}}$ are the LJ parameters for carbon-water oxygen interactions, $R_{v\text{C-HW}}$ and $D_{v\text{C-HW}}$ are the LJ parameters for carbon-water hydrogen interactions. $R_{v\text{C-OW}}$ and $R_{v\text{C-HW}}$ are in nm, and $D_{v\text{C-OW}}$ and $D_{v\text{C-HW}}$ are in kcal/mol.

m-n	$R_{v\text{C-OW}}$	$D_{v\text{C-OW}}$	$R_{v\text{C-HW}}$	$D_{v\text{C-HW}}$
6-10	3.875	0.0633	3.033	0.0471
6-12	3.857	0.0850	3.019	0.0383
6-14	3.832	0.1056	2.999	0.0295

.

In the current study, two carbon layers are used to represent the graphite surface. We also investigate if adding extra carbon layers would affect the contact angle. For the interaction parameters obtained from the RPA *ab initio* data, we change the number of carbon layers from one to three, with everything else kept unchanged. The resulting contact angles are summarized in Fig. 4.6(d). The change in contact angle is negligible when the number of carbon layers is increased from two to three. But the mono-layer graphene gives an appreciably bigger contact angle than the double-layer graphite. Hence, we use two carbon layers as a good representation of the graphite surface.

The effects of different water models on the contact angle are also investigated. SPC/E water model was found [20] to predict 17.4° larger contact angle than TIP3P [111] water model for the carbon-water interaction parameters used by Hummer et al. [39]. We compute contact angles using TIP5P water model [116] for interaction parameters used by Werder et al. [20]. The resulting contact angle is 82.8°, which compares well to 86.9° by the SPC/E water model with the same carbon-water interaction parameters. As a result, we use the SPC/E water model for all our contact angle simulations except for the interaction parameters used by Hummer et al. [39]. The TIP3P water model is utilized for the interaction parameters used by Hummer et al., to be consistent with the work by Hummer et al. [39]. The contact angles for all the carbon-water parameters are summarized in Table A.1.

4.6.2 Comparing Predicted Contact Angles in MD with Experiments

The experimental water contact angles on graphite surface available in the literature fall into two ranges: 80-90°, which is measured directly in air [7, 8, 9, 10], and 30-40°, which is measured using ultra-high vacuum technique [4, 5]. In the latter work, Schrader [4] was able to reproduce the 80-90° if the experiments were done in air for the same graphite surface. Hydrocarbon contamination of the high-energy graphite surface from the air was suspected to be the cause of the high contact angle. MD simulations are done to confirm this by using ethane molecules as the hydrocarbon contamination. The force field for ethane molecules is taken from Ref [138]. Three contaminant surface coverage number densities of 0, 1.0 nm^{-2} and 4.0 nm^{-2} are considered.

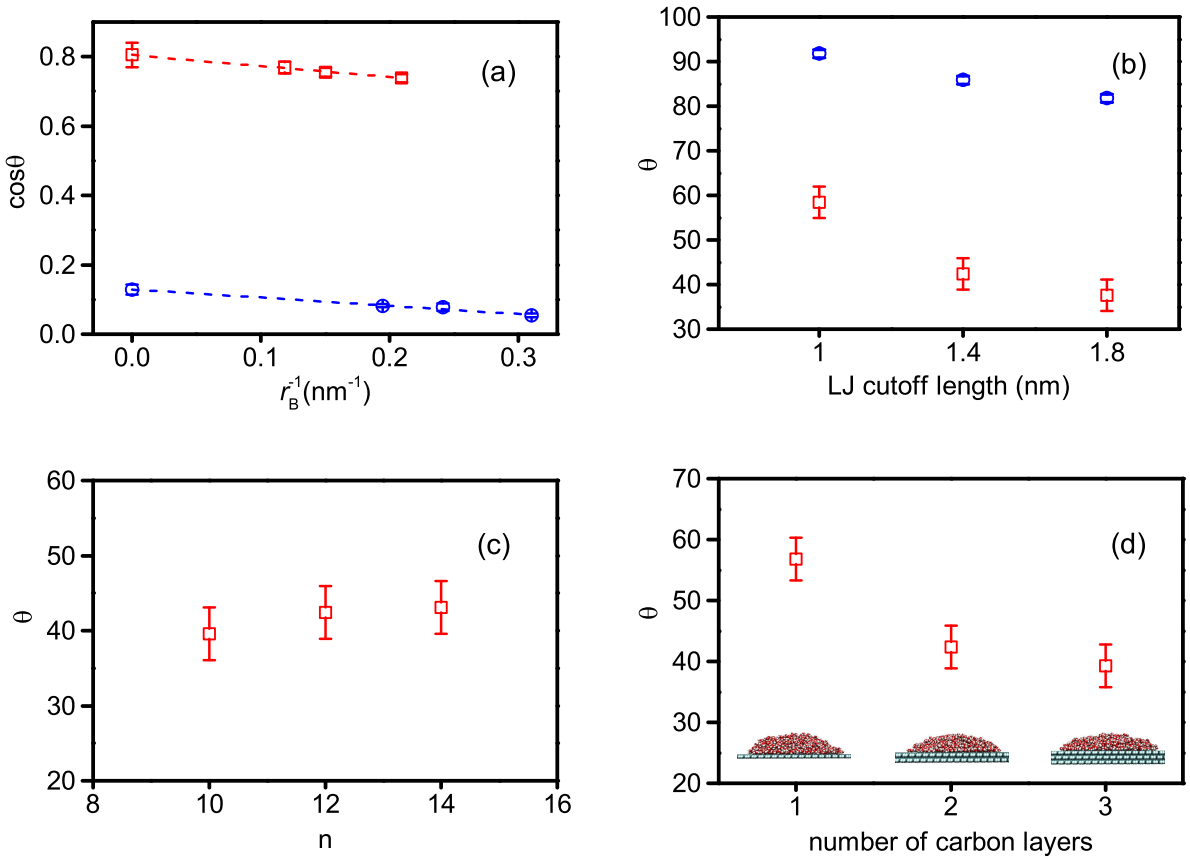

Figure 4.6: Water contact angles on clean graphite surface. (a) Extrapolation of nano-droplet contact angles θ to the macroscopic limit for C-water interaction parameters used by Werder et al. [20](represented by blue circles) and parameters obtained from RPA data (represented by red squares). (b) Dependence of contact angles on LJ cutoff length for the two C-water interaction parameters used in (a). (c) Dependence of contact angles on the choice of LJ6-n fitting function forms to the RPA data. The fitted parameters are summarized in Table A.1. (d) Dependence of contact angles on the number of carbon layers. The contact angle values are in the unit of degrees. The contact angle values are the mean of three simulation runs with different initial velocity configurations. The error bar of the contact angle is 1.0° for the interaction parameters used by Werder et al. [20] and 3.6° for the RPA data.

Three carbon-water interaction parameters with varying graphene-water interaction strength are used: the interaction parameters obtained from CCSD(T) data [126] have the strongest interaction strength (high-energy surface), the parameters used by Werder et al. [20] have the lowest interaction strength (low-energy surface), and the interaction parameters obtained from DFT-SAPT data [2] have the interaction strength in between. The contact angle of the water droplet on a clean surface is different from that on a contaminated surface. The contact angles for each combination of carbon-water interaction parameters and contaminant surface coverage number densities are summarized in Fig. 4.9. From Fig. 4.9, the contact angles increase with increasing contaminant surface coverage density for all the three carbon-water interaction parameters. The contact angles approach the same value when the surface coverage density is high, i.e. when the contaminants

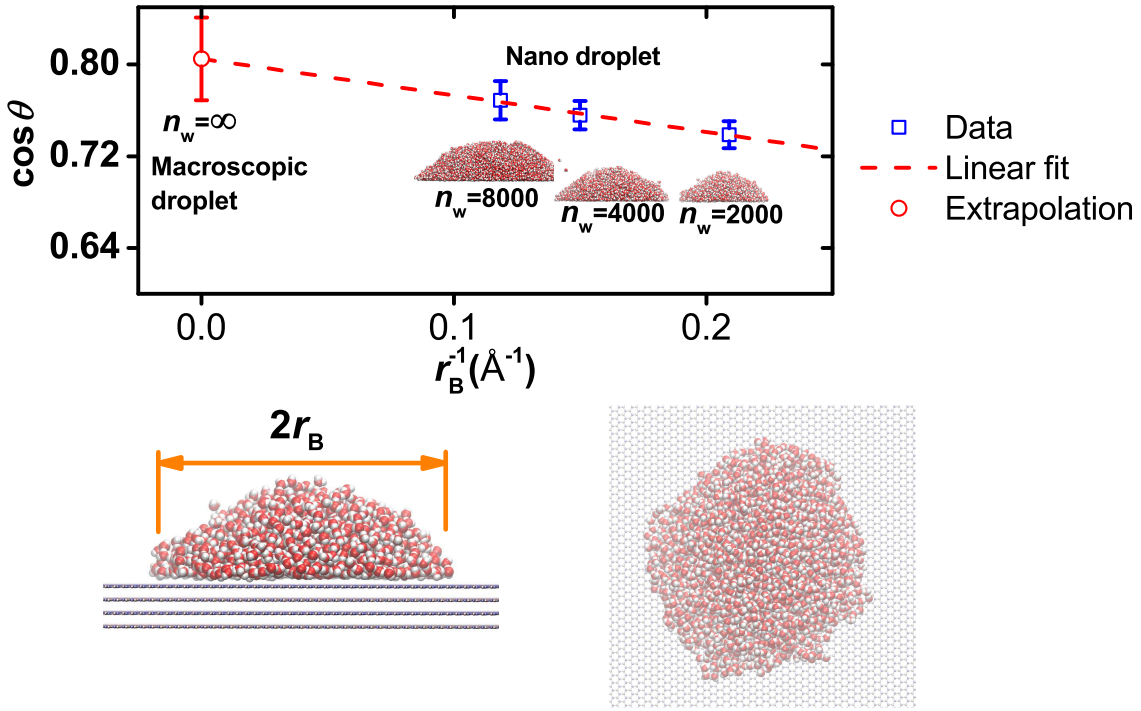

Figure 4.7: The contact angle, θ, of nano water droplets on graphite predicted by molecular dynamics (MD) simulations. Three nano droplets composed of n_{w}=2000, 4000, or 8000 water molecules are considered. An extrapolation of θ to the contact angle of the macroscopic droplet ($n_{\mathrm{w}} = \infty$), θ_∞, is performed. The side and top views of the configuration used in the simulations are shown in the inset figures.

are closely packed on the surface and the water droplet is sitting on top of the contaminant. The influence of surface contamination on contact angle is more sensitive for high-energy surface. These results suggest that to simulate experimental contact angles measured in air, surface contamination has to be considered.

Next, we perform simulations on the clean surface and compare the contact angles to the experimental values [4, 5] of 42±7°, as shown in Fig. 4.8. The contact angles predicted by carbon-water interaction parameters obtained from the DFT-SAPT and RPA data agree pretty well with experiments. The carbon-water interaction parameters obtained from MP2 data slightly over-estimate the carbon-water interaction strength. The interaction parameters obtained from CCSD(T) data tend to strongly overestimate the strength. Although the interaction parameters obtained from the DFT-SAPT and RPA data give the comparable graphene-water binding energy, the contact angles predicted by both methods deviate by around 8°. This shows that graphene-water binding energy alone may not be adequate in describing graphitic carbon-water interaction. The dependence of graphene-water interaction energies on separation distance and orientation needs to be included in the development of graphitic carbon-water interaction parameters.

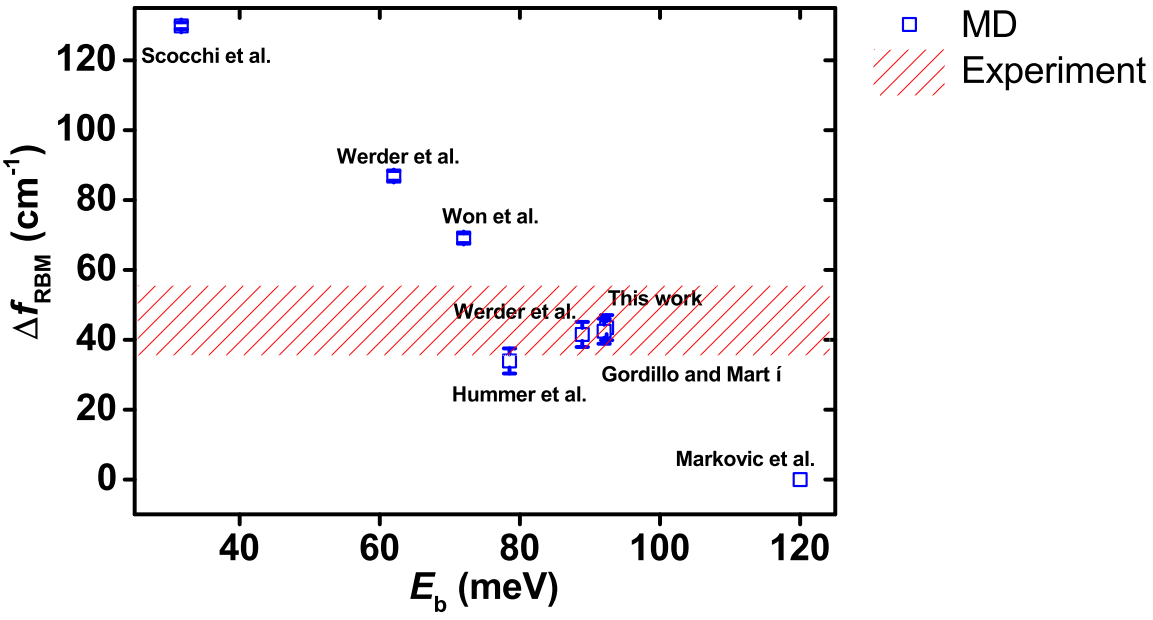

Figure 4.8: The binding energy between water and graphene, E_{b}, and values of contact angle on graphite predicted using water-graphitic carbon force field parameters developed by various force field parameters.

4.6.3 CNT RBM Frequency in MD and Comparison with Experiments

The RBM frequency of an isolated CNT, f_{RBM}, depends on the diameter of the CNT, d, by the formula [139] $f_{RBM} = C_1/d$, where the constant C_1=223.8 nm·cm^{-1} is obtained by comparing to Raman spectroscopy [140]. For a (22,0) CNT which has a diameter of 1.72 nm, the RBM frequency is 130.1 cm^{-1}. In MD, the AIREBO potential predicts the RBM frequency of a (22,0) CNT as 133.1±0.3 cm^{-1}. The good agreement between MD and experimental data validates the AIREBO potential as a good model to study the RBM frequency of CNT.

When a CNT is immersed in water, due to the interaction between CNT carbon atoms and water molecules, the internal vibrational motion of the CNT changes. This change can be quantified by the shift in the RBM frequency of CNT, Δf_{RBM}, as shown in Fig. 4.10. Longhurst and Quirke [76] showed that Δf_{RBM} depends sensitively on the carbon-water interaction parameters using MD. Experimentally Δf_{RBM} of a CNT immersed in water can be easily detected by modern Raman machines, which provides an opportunity to probe the intermolecular forces between CNT and water. Using Raman spectroscopy, Izard et al. [6] measured a frequency shift of 7.3 cm^{-1} for (22,0) CNT. The carbon-water interaction parameters obtained from MP2 data predicts a frequency shift of 8.8±0.6 cm^{-1}, which agrees well with experiments,

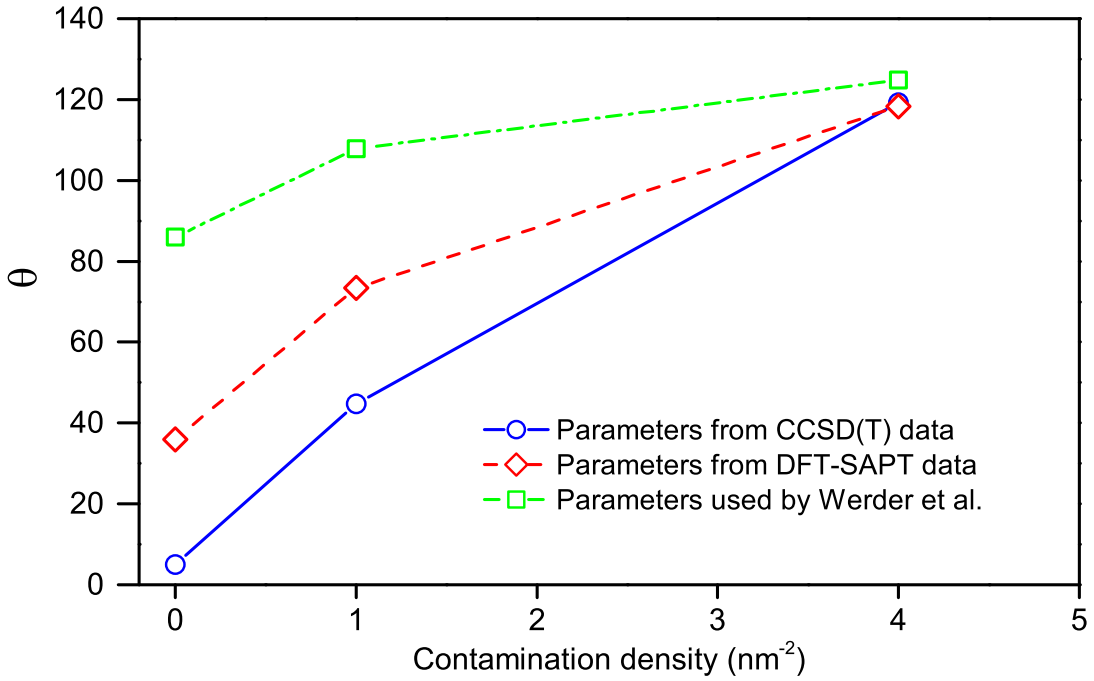

Figure 4.9: Effects of surface contamination on contact angle θ. Three graphitic carbon-water interaction parameters are considered: the interaction parameters used by Werder et al. [20], the interaction parameters obtained from DFT-SAPT data, and the interaction parameters obtained from CCSD(T) data.

as shown in Fig. 4.11. The RBM frequency of the (22,0) CNT immersed in water predicted by the carbon-water interaction parameters obtained from MP2 data is 141.9±0.5 cm^{-1}, in agreement with the Raman spectroscopy measurement of 142.4 cm^{-1} for CNT in aqueous surfactant solutions [141]. The error of the CNT RBM frequency mainly comes from the Gaussian function fitting. A summary of Δf_{RBM} predicted by the carbon-water interaction parameters is listed in Table A.1. The C-water interaction parameters obtained from RPA or DFT-SAPT data also predict a frequency shift that is in good agreement with experiments. The C-water interaction parameters obtained from CCSD(T) data overestimate the frequency shift probably due to the use of small basis set in the CCSD(T) calculations [126].

4.7 Summary

In summary, a combination of high-level theoretical electronic structure approaches was used to study the interaction between graphene and water. The DMC and CCSD(T) methods benchmark each other at the molecular level. DMC was used to validate RPA calculations. Then we used the RPA method to compute the potential energy surface between graphene and water. We developed force field parameters

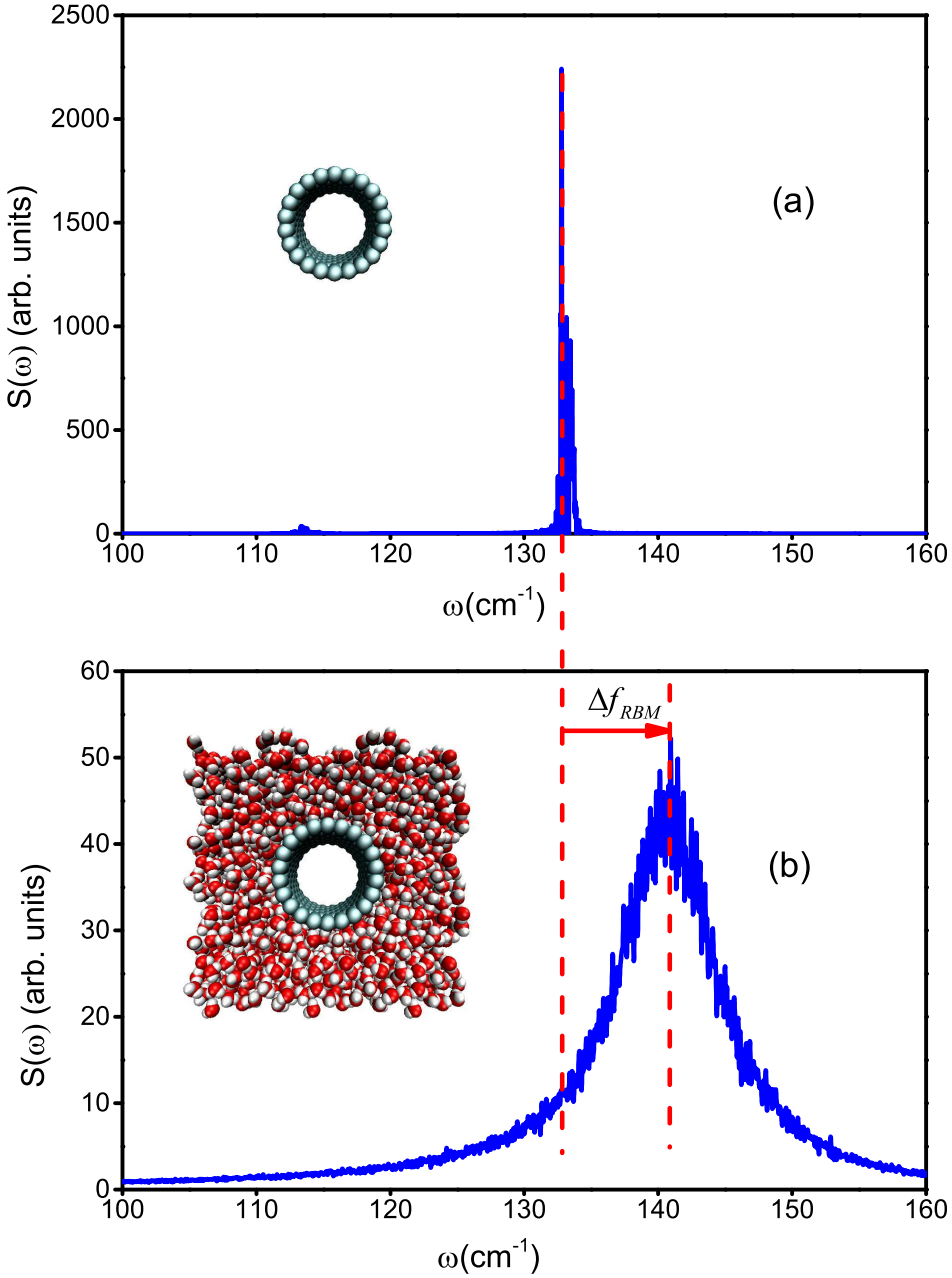

Figure 4.10: Power spectra obtained from MD for (a) an isolated (22,0) CNT (b) a (22,0) CNT immersed in water. The peak in each figure corresponds to the radial breathing mode. The C-water interaction parameters obtained from DFT-SAPT data are used for (b).

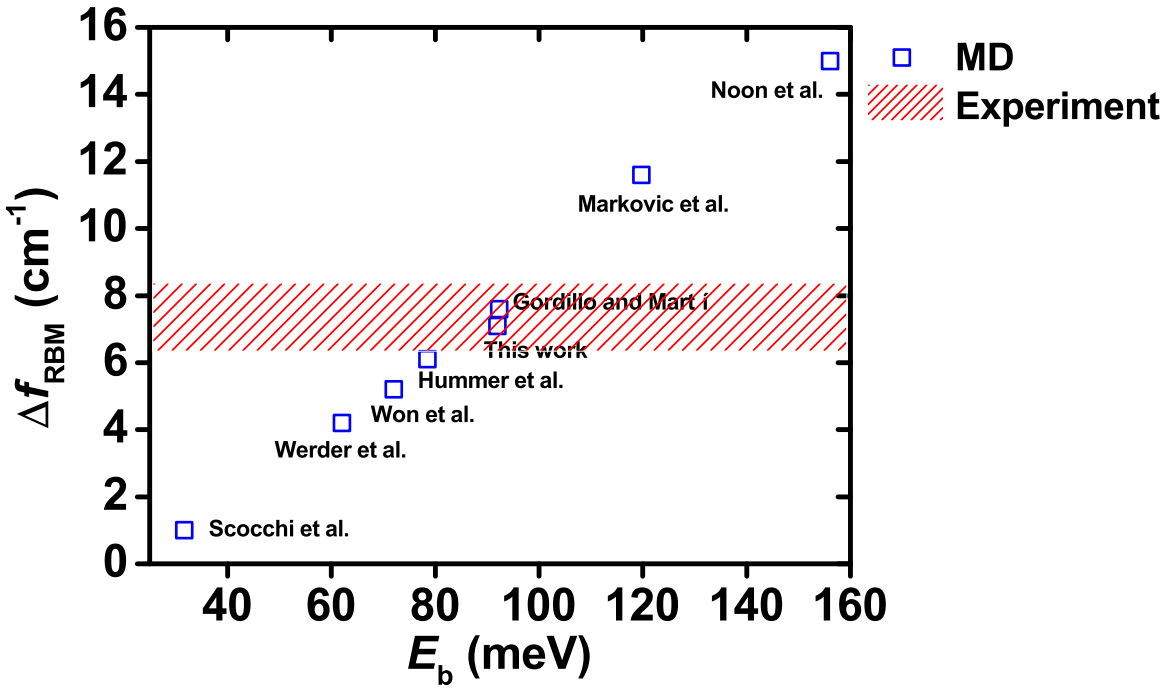

Figure 4.11: The binding energy between water and graphene, E_{b}, and values of carbon nanotube (CNT) radial breathing mode (RBM) frequency shift, Δf_{RBM}, predicted using water-graphitic carbon force field parameters developed by various force field parameters.

based on the RPA data with no fitting to experiments. The parameters are able to predict water contact angle on graphite and CNT radial breathing mode frequency shift in excellent agreement with experimental measurements. The agreement shows that it is feasible to develop accurate force field parameters for the graphene-water interaction entirely from first-principle calculations. The multiscale approach all the way from diffusion Monte Carlo or coupled cluster to predicting macroscopic properties is extended from the hBN-water interaction [120] to the graphitic-carbon-water interaction.

We also revisited the MP2 calculations, with proper consideration of the size of basis sets and energy component analysis to extrapolate to infinite-sized graphene limit. Then graphitic carbon-water interaction parameters are fitted to MP2 data from this work and the *ab initio* data from RPA, DFT-SAPT and CCSD(T) methods in the literature. The accuracy of the interaction parameters is evaluated also by predicting water contact angle on graphite and CNT RBM frequency shift and comparing them with experimental data. The carbon-water interaction parameters obtained from MP2 data predict the CNT RBM frequency shift that is in good agreement with experiments. The carbon-water interaction parameters obtained from DFT-SAPT or RPA data predict both water contact angles and CNT RBM frequency shift that agree well

with experiments. The carbon-water interaction parameters obtained from CCSD(T) data underestimate water contact angles and overestimate CNT RBM frequency shift probably due to the use of small basis sets in the CCSD(T) calculations [126]. The good agreement of the predictions by the carbon-water interaction parameters obtained from DFT-SAPT and RPA data with experiments suggests that the graphitic carbon-water strength is stronger than previously thought. A recent scanning tunneling microscopy study [28] observed a monolayer of water trapped between graphene and CNT. Water does not experience capillary evaporation when confined between two graphitic carbon surfaces down to a monolayer thickness. This indicates a strong graphitic carbon-water interaction.

Chapter 5

Molybdenum Disulfide and Water Interaction Parameters

5.1 RPA Calculations

The RPA calculations were performed using the VASP package [100, 101], projector-augmented wave potentials, and an energy cutoff of 408 eV. We expanded the response function in plane waves up to an energy cutoff of 272 eV. The exchange energy and correlation energy are computed separately with different MoS_2 supercell sizes and Brillouin zone sampling Monkhorst-Pack k-meshes: A 4×4 supercell with a 2×2 k-mesh was used for the exchange energy, and a 2×2 supercell with a 4×4 k-mesh for the correlation energy. A lattice constant of 18 Å along the direction perpendicular to the MoS_2 surface (z-axis) was used. The potential energy surface between MoS_2 and water was explored using the RPA method by varying the orientation and separation distance of the water molecule with respect to the MoS_2 surface. For simplicity, MoS_2 and the water molecule internal geometry were fixed while changing their relative position: The Mo-S bond length and S-Mo-S bond angles are set to the experimental values for MoS_2 [142], and the water monomer is set to the experimental gas phase geometry [90]. The interaction energy between water and MoS_2, ΔE, is computed by $\Delta E = E(\text{MoS}_2\text{-water}) - E(\text{MoS}_2) - E(\text{water})$, where $E(\text{MoS}_2\text{-water})$, $E(\text{MoS}_2)$, and $E(\text{water})$ are the energies of the MoS_2-water dimer, MoS_2, and the water molecule, respectively, computed by the RPA method.

The RPA procedure has a few well-defined approximations. The approximations include errors due to the the incomplete basis sets, the finite lattice constant along the z-axis, the non-zero water coverage, finite supercell, and finite k-points. We checked the basis set convergence by increasing the plane wave energy cutoff. Using an energy cutoff of 600 eV for the plane wave and 400eV for the response function leads to a difference of about 1 meV in the interaction energy. We checked the convergence of the lattice constant along the z-axis by increasing it to 22 Å and the change in the interaction energy is less than 1 meV. We also checked the convergence of k-points by systematically computing the interaction energy using a series of k-grids. The convergence of the exchange energy and the correlation energy is considered separately, as shown in Fig. 5.1. We found that the exchange energy has a weak dependence on the k-grid, while the

dependence of correlation energy is strong. Based on the results for hBN and graphene, we expect that the correlation energy converges at a 4×4 k-grid for a 2×2 supercell. We checked the convergence of supercell and water coverage density by increasing the supercell size while keeping the equivalent k-point mesh the same. The results are summarized in Fig. 5.1. We found that the exchange energy has a strong dependence on the supercell size and water coverage density, while the the dependence of correlation energy is weak. The exchange energy converges at a 4×4 supercell, and increasing the k-grid to 8×8 leads to a difference of less than 1 meV. Considering all the approximations, we estimate the error to be less than 2 meV on the interaction energy computed by the RPA method. With errors controlled, we use the RPA method to explore the potential energy surface between MoS_2 and water in order to develop MoS_2-water non-bonded interaction models for use in MD simulations.

5.2 Potential Fitting

The interaction between water and MoS_2 in MD is modeled by the electrostatic interaction ΔE_{el} and the vdW interaction ΔE_{vdW}:

$$\begin{aligned}
\Delta E &= \Delta E_{\mathrm{el}} + \Delta E_{\mathrm{vdW}} \\
\Delta E_{\mathrm{el}} &= \sum_{i \in \mathrm{MoS2}} \sum_{j \in \mathrm{water}} \frac{q_i q_j}{r_{ij}} \\
\Delta E_{\mathrm{vdW}} &= \sum_{i \in \mathrm{MoS2}} \sum_{j \in \mathrm{water}} 4\epsilon_{ij} \left[\left(\frac{\sigma_{ij}}{r_{ij}} \right)^{12} - \left(\frac{\sigma_{ij}}{r_{ij}} \right)^{6} \right]
\end{aligned} \tag{5.1}$$

where r_{ij} is the distance between atom i and atom j, q_i and q_j the partial charge of atom i and atom j, ϵ_{ij} the depth of the potential well of vdW interaction between the two atoms, and $2^{1/6}\sigma_{ij}$ the position of the potential well. The atomic partial charges for water are taken from the water model (e.g. SPC/E [115], TIP3P, TIP4P [111] or TIP5P [116]). The partial charges for Mo/S atoms, $q_{\mathrm{Mo}}/q_{\mathrm{S}}$ are computed by fitting to the electrostatic potential from 2nd-order Møller-Plesset perturbation (MP2) theory calculation. The ϵ_{ij} and σ_{ij} are obtained by fitting to the RPA data. For the interaction between water (which has O and H atoms) and MoS_2 (which has Mo and S atoms), there are four pairs of ϵ_{ij} and σ_{ij} parameters, in total four parameters to fit.

The parameters are obtained by fitting to the Boltzmann averaged vdW interaction energies among different water orientations. The least-squares fit was used. The parameters are summarized in Table A.3. Also included in the table are force field parameters from the literature [21, 22] and the water models used in their work. The quality of different parameters can be evaluated by predicting properties using MD

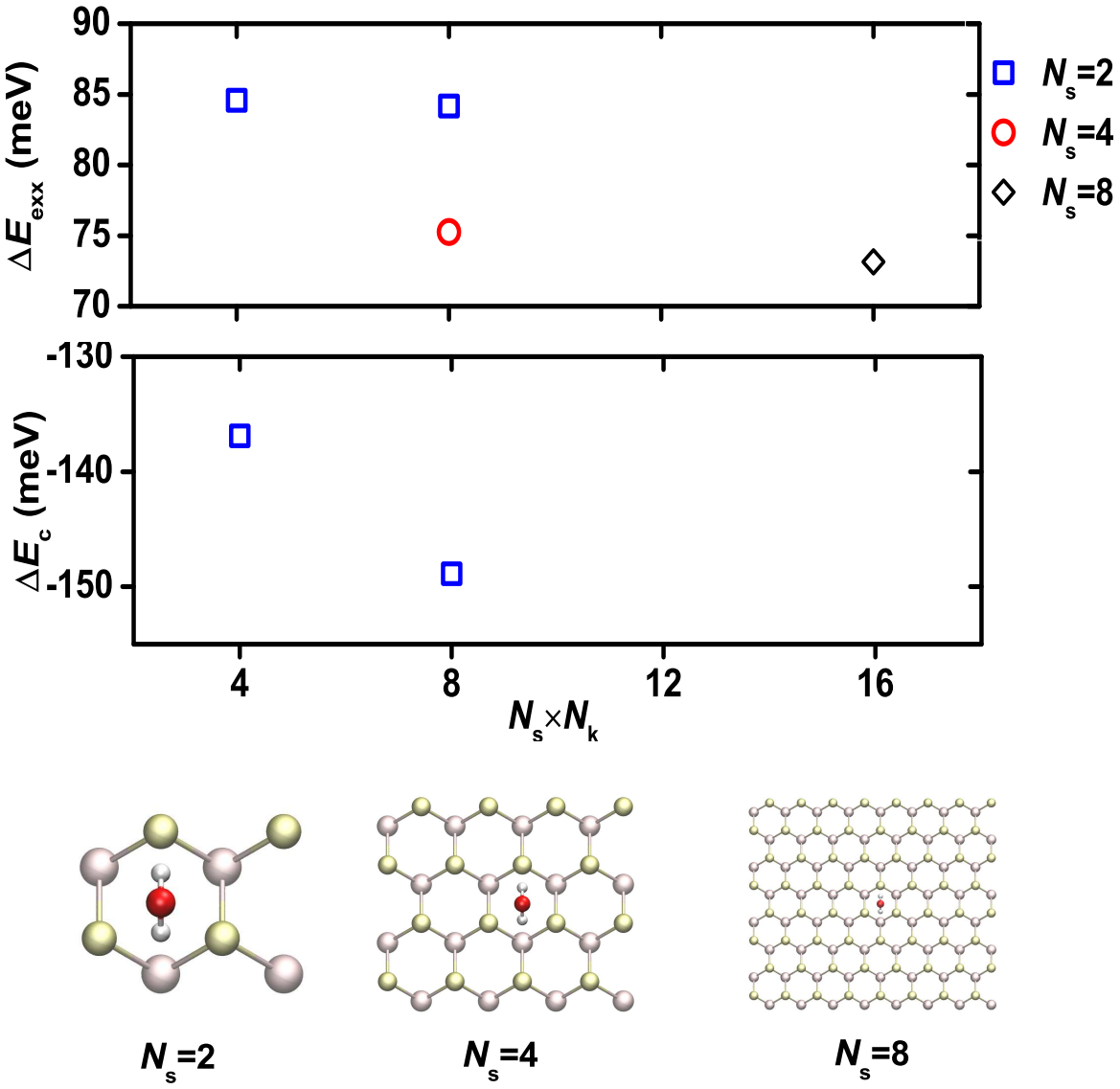

Figure 5.1: The interaction energy between a single water molecule and MoS_2 represented by $N_s \times N_s \times 1$ supercell with Brillouin zone sampled by a $N_k \times N_k \times 1$ k-mesh. The energy is computed using the random phase approximation (RPA) method. The two components, the exchange energy, ΔE_{exx}, and the correlation energy, ΔE_c, are converged separately.

simulations and comparing to experimental measurements.

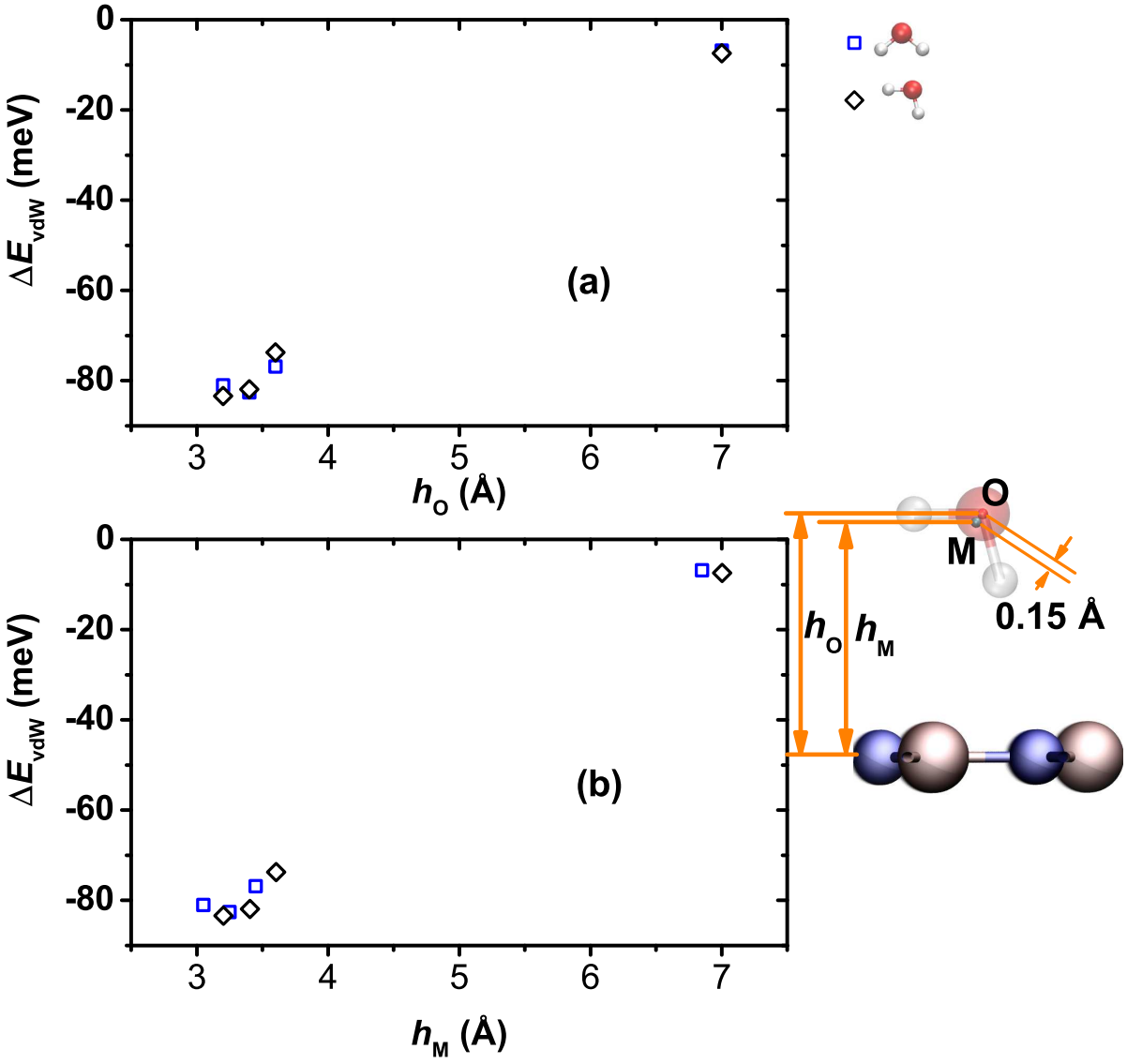

Figure 5.2: The vdW interaction energies between MoS_2 and water for six different water orientations. The point M is located at the bisector of HOH angle, as shown in the inset figure.

5.3 Comparison with Experiments

Water contact angle on bulk MoS_2 is a property that has been reported by multiple experimental groups [143, 144, 145, 146, 147, 148, 149] and rigorously studied with minimal surface contamination [143, 144]. The contact angle values reported by experiments are in the range of 70°. The contact angle is simulated

using MD following the procedure by Werder et al. [20, 110]. The contact angle values for nano-droplets obtained from MD, θ, are extrapolated to that of macroscopic droplet, θ_∞, following the modified Young's equation, so that a direct comparison between MD and experiments is possible:

$$\cos\theta = \cos\theta_\infty - \frac{\tau}{\gamma_{\mathrm{LV}}} r_{\mathrm{B}}^{-1} \tag{5.2}$$

where γ_{LV} is the water liquid-vapor surface tension, r_{B} the droplet base radius, and τ the line tension. The comparison of contact angle values between MD and experiments is shown in Fig.5.3. The parameters by Heiranian et al. [22] and Barati et al. [21] slightly overestimate the contact angle. The parameters obtained by fitting to the RPA data in this work, with no adjustable parameter or no fit from experimental data, are able to predict the water contact angle that is in excellent agreement with experimental measurements. The agreement shows that it is a feasible path to develop accurate force field parameters entirely from first-principle calculations, which has been shown for graphitic-carbon-water interactions [110] and hexagonal-boron-nitride-water interactions [150].

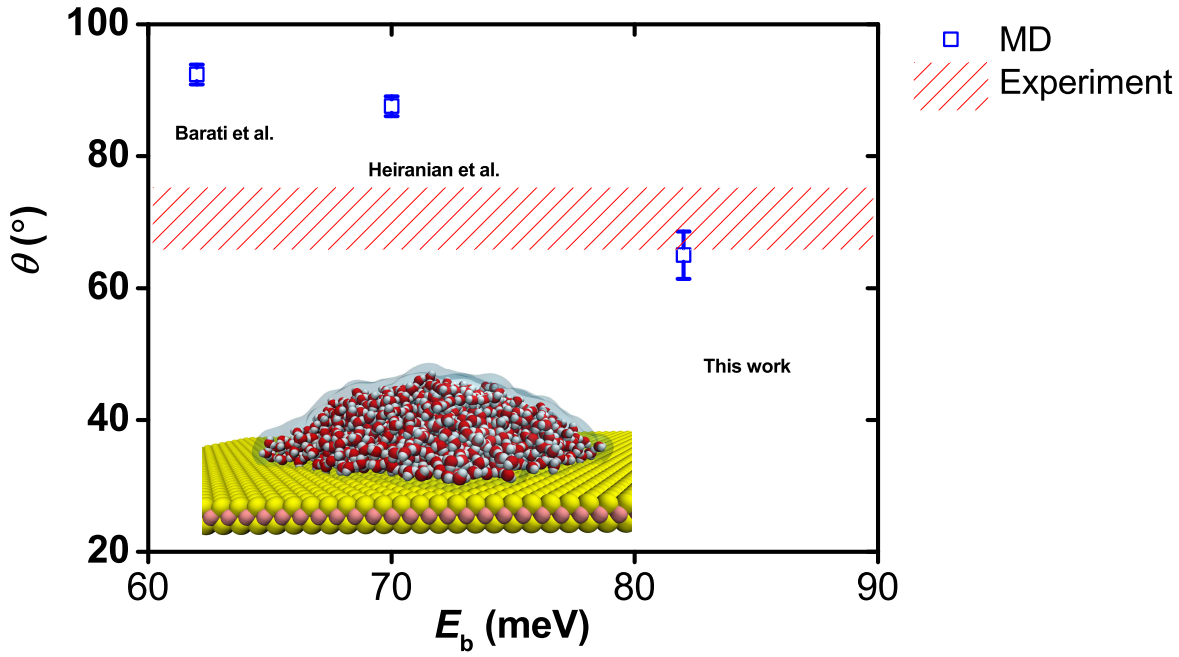

Figure 5.3: The binding energy between water and MoS_2 monolayer, E_{b}, and contact angle values, θ, predicted using MoS_2-water force field parameters developed by Barati et al. [21], Heiranian et al. [22], and from this work.

5.4 Summary

In summary, we use a multiscale approach to study the interaction between MoS_2 and water. we use the RPA method to compute the potential energy surface between MoS_2 and water. We develop force field parameters based on the RPA data with no fitting from experiments. The parameters are able to predict water contact angle on MoS_2 in excellent agreement with experimental measurements. The agreement shows that it is a feasible path to develop accurate force field parameters entirely from first-principle calculations. In current work, DMC calculations were not performed due to the computational cost. We assume that RPA can predict the energy as accurate as DMC for the MoS_2-water interaction, like for hBN-water and graphene-water. In future work, we would like to verify this assumption.

Chapter 6

Conclusions

In summary, a combination of high-level theoretical electronic structure approaches was used to study the interaction between graphene/graphene-like materials and water. The DMC and CCSD(T) methods benchmark each other at the molecular level. DMC was used to validate RPA and MP2 calculations. Then we used the RPA method to compute the potential energy surface between two-dimensional materials and water. We developed force field parameters based on the RPA data with no fitting to experiments. The parameters are able to predict properties in excellent agreement with experimental measurements. The agreement shows that it is feasible to develop accurate force field parameters entirely from first-principle calculations. The multiscale approach all the way from diffusion Monte Carlo or coupled cluster to predicting macroscopic properties is extended from molecular interactions [120] to molecule-solid interaction in this work. The scheme has been applied to hBN-water, graphene-water, and MoS_2-water systems.

Appendix

Force Field Parameters

Table A.1: A summary of LJ parameters in the literature and from this work, with corresponding graphene-water binding energy E_b, predicted water contact angle θ on graphite surface, and CNT RBM frequency shift Δf_{RBM}. The LJ parameters include carbon-water oxygen parameters $\sigma_{\text{C-OW}}$ and $\epsilon_{\text{C-OW}}$, and carbon-water hydrogen parameters $\sigma_{\text{C-HW}}$ and $\epsilon_{\text{C-HW}}$. $\sigma_{\text{C-OW}}$ and $\sigma_{\text{C-HW}}$ are in Å, $\epsilon_{\text{C-OW}}$ and $\epsilon_{\text{C-HW}}$ are in kcal/mol, E_b is in kcal/mol, θ is in degrees, and Δf_{RBM} is in cm^{-1}. The error bar for each contact angle value is 3.6°. The error bar for CNT RBM frequency shift is 0.6 cm^{-1}. The experimental value is 42±7° for water contact angle on graphite surface [4, 5], and 7.3 cm^{-1} for CNT RBM frequency shift [6].

Ref	C-water model	$\sigma_{\text{C-OW}}$	$\epsilon_{\text{C-OW}}$	$\sigma_{\text{C-HW}}$	$\epsilon_{\text{C-HW}}$	E_b	θ	Δf_{RBM}
Hummer et al. [39]	Combine C-C from AMBER [83] and O-O from TIP3P [111]	3.275	0.1143	N/A	N/A	1.81	33.9	6.1
Won et al. [45]	Combine C-C from Chen et al. [151] and O-O from SPC/E [69]	3.2779	0.1037	N/A	N/A	1.66	69.1	5.2
Noon et al. [46]	Combine C-C from CHARMM [82] and O-O,H-H from modified TIP3P [129]	3.296	0.1382	2.58	0.0772	3.60	0.0	15.0
Gordillo et al. [47]	Combine C-C, H-H from Steele et al.[152] and O-O from SPC-F2 [153]	3.280	0.0930	2.81	0.0308	2.13	43.5	7.6
Werder et al. [20]	Fits to an experimental water contact angle on graphite of 86° [7]	3.190	0.0937	N/A	N/A	1.43	86.9	4.2
Werder et al. [20]	Fits to an experimental water contact angle on graphite of 42° [4]	3.190	0.1349	N/A	N/A	2.05	41.5	7.6
Scocchi [48]	Fits to an experimental water contact angle on graphene of 127° [9]	3.190	0.0478	N/A	N/A	0.73	129.9	1.0
Markovic et al. [49]	C-OW by experimental oxygen gas adsorption on graphite [154], C-HW by combining C-C,H-H from Steele et al. [152, 108]	3.190	0.0935	2.82	0.0605	2.76	0.0	11.6
This work	Fitting to MP2 data	3.430	0.1164	2.685	0.0263	2.54	10.3	8.8
This work	Fitting to DFT-SAPT data [2]	3.372	0.1039	2.640	0.0256	2.24	34.2	8.2
This work	Fitting to RPA data [55]	3.436	0.0850	2.690	0.0383	2.26	42.4	7.1
This work	Fitting to CCSD(T) data [126]	3.126	0.1646	2.447	0.0246	2.84	<10	11.8

Table A.2: Summary of water-hBN force field parameters used in the literature and developed in this work. The force field parameters include the Lennard-Jones parameters $\sigma_{B\alpha}$, $\sigma_{N\alpha}$, $\epsilon_{B\alpha}$, and $\epsilon_{N\alpha}$ (α=O, H, or M), the partial charge q_B and q_N, and the partial charges for water. The partial charge values for water are specified by providing the type of the water model used. $\sigma_{B\alpha}$ and $\sigma_{N\alpha}$ are in Å, and $\epsilon_{B\alpha}$ and $\epsilon_{N\alpha}$ in kcal/mol.

Ref.	hBN-water model	α	$\sigma_{B\alpha}$	$\epsilon_{B\alpha}$	$\sigma_{N\alpha}$	$\epsilon_{N\alpha}$	q_B/q_N	water model
Won and Aluru [15]	Combine B-B, N-N from DREIDING [155] and O-O from SPC/E [115]	O	3.310	0.1214	3.266	0.1500	±0.37	SPC/E [115]
Gordillo and Martí [16]	Combine B-B, N-N from DREIDING [155], O-O from SPC-F2 [153], and H-H from Steele et al. [152]	O H	3.310 2.837	0.1214 0.0404	3.266 2.793	0.1500 0.0499	0.0	SPC-F2 [153]
Hilder et al.[17]	Fit to DFT-D data	O	3.265	0.2624	3.183	0.1757	±0.98	TIP3P [111]
This work	Fit to RPA data	M	3.322	0.0981	3.278	0.1213	±0.30	TIP4P [111]

Table A.3: Summary of water-MoS_2 force field parameters used in the literature and developed in this work. The force field parameters include the Lennard-Jones parameters σ_{MoO}, σ_{SO}, ϵ_{MoO}, and ϵ_{SO}, the partial charge q_{Mo} and q_S, and the partial charges for water. The partial charge values for water are specified by providing the type of the water model used. σ_{MoO} and σ_{SO} are in Å, and ϵ_{MoO} and ϵ_{SO} in kcal/mol.

Ref.	MoS_2-water model	σ_{MoO}	ϵ_{MoO}	σ_{SO}	ϵ_{SO}	q_{Mo}/q_S	water model
Heiranian et al. [22]	Combine Mo-Mo, S-S from Sinnot et al. [142] and O-O from SPC/E [115]	3.683	0.0458	3.148	0.2677	0.0	SPC/E [115]
Barati et al. [21]	Combine Mo-Mo, O-O from Stewart [156], O-O from TIP3P [153] [152]	3.683	0.0458	3.148	0.2228	0.0	TIP3P [115]
This work	Fit to RPA data	3.934	0.0458	3.362	0.2680	0.6/-0.3	SPC/E [111]

References

[1] E. M. Cabaleiro-Lago, J. A. Carrazana-García, and J. Rodríguez-Otero. Study of the interaction between water and hydrogen sulfide with polycyclic aromatic hydrocarbons. *J. Chem. Phys.*, 130(23):234307, 2009.

[2] G. R. Jenness, O. Karalti, and K. D. Jordan. Benchmark calculations of water-acene interaction energies: Extrapolation to the water-graphene limit and assessment of dispersion-corrected dft methods. *Phys Chem Chem Phys*, 12(24):6375–81, 2010.

[3] I. W. Sudiarta and D. J. Geldart. Interaction energy of a water molecule with a single-layer graphitic surface modeled by hydrogen- and fluorine-terminated clusters. *J. Phys. Chem. A*, 110(35):10501–6, 2006.

[4] M.E. Schrader. Ultrahigh vacuum techniques in the measurement of contact angles. iv. water on graphite (0001). *J. Phys. Chem.*, 79(23):2508–2515, 1975.

[5] M.E. Schrader. Ultrahigh-vacuum techniques in the measurement of contact angles. 5. leed study of the effect of structure on the wettability of graphite. *J. Phys. Chem.*, 84(21):2774–2779, 1980.

[6] N. Izard, D. Riehl, and E. Anglaret. Exfoliation of single-wall carbon nanotubes in aqueous surfactant suspensions: A raman study. *Phys. Rev. B*, 71(19):195417, 2005.

[7] F.M. Fowkes and W.D. Harkins. The state of monolayers adsorbed at the interface solid-aqueous solution. *J. Am. Chem. Soc.*, 62(12):3377–3386, 1940.

[8] I. Morcos. On contact angle and dispersion energy of the cleavage graphite/water system. *J. Colloid Interface Sci.*, 34(3):469–471, 1970.

[9] S. Wang, Y. Zhang, N. Abidi, and L. Cabrales. Wettability and surface free energy of graphene films. *Langmuir*, 25(18):11078–11081, 2009.

[10] Y.J. Shin, Y. Wang, H. Huang, G. Kalon, A.T.S. Wee, Z. Shen, C.S. Bhatia, and H. Yang. Surface-energy engineering of graphene. *Langmuir*, 26(6):3798–3802, 2010.

[11] Ali Ashraf, Yanbin Wu, Michael C. Wang, Narayana R. Aluru, Seyed A. Dastgheib, and SungWoo Nam. Spectroscopic investigation of the wettability of multilayer graphene using highly ordered pyrolytic graphite as a model material. *Langmuir*, 30(43):12827–12836, 2014.

[12] Zhiting Li, Yongjin Wang, Andrew Kozbial, Ganesh Shenoy, Feng Zhou, Rebecca McGinley, Patrick Ireland, Brittni Morganstein, Alyssa Kunkel, Sumedh P. Surwade, Lei Li, and Haitao Liu. Effect of airborne contaminants on the wettability of supported graphene and graphite. *Nat Mater*, 12(10):925–31, 2013.

[13] Yanbin Wu, Lucas K. Wagner, and Narayana R. Aluru. The interaction between hexagonal boron nitride and water from first principles. *The Journal of Chemical Physics*, 142(23):234702, 2015.

[14] Yasmine S. Al-Hamdani, Ming Ma, Dario Alfè, O. Anatole von Lilienfeld, and Angelos Michaelides. Communication: Water on hexagonal boron nitride from diffusion monte carlo. *The Journal of Chemical Physics*, 142(18):181101, 2015.

[15] C. Y. Won and N. R. Aluru. Water permeation through a subnanometer boron nitride nanotube. *Journal of the American Chemical Society*, 129(10):2748–+, 2007.

[16] M. C. Gordillo and J. Martí. Wetting and prewetting of water on top of a single sheet of hexagonal boron nitride. *Physical Review E*, 84(1), 2011.

[17] T. A. Hilder, R. Yang, V. Ganesh, D. Gordon, A. Bliznyuk, A. P. Rendell, and S. H. Chung. Validity of current force fields for simulations on boron nitride nanotubes. *Micro and Nano Letters*, 5(2):150, 2010.

[18] S. Grimme. Semiempirical gga-type density functional constructed with a long-range dispersion correction. *Journal of Computational Chemistry*, 27(15):1787–1799, 2006.

[19] Alexandre Tkatchenko and Matthias Scheffler. Accurate molecular van der waals interactions from ground-state electron density and free-atom reference data. *Physical Review Letters*, 102(7):073005, 2009.

[20] T. Werder, J. H. Walther, R. L. Jaffe, T. Halicioglu, and P. Koumoutsakos. On the water-carbon interaction for use in molecular dynamics simulations of graphite and carbon nanotubes. *The Journal of Physical Chemistry B*, 107(6):1345–1352, 2003.

[21] Amir Barati Farimani, Kyoungmin Min, and Narayana R. Aluru. Dna base detection using a single-layer mos2. *ACS Nano*, 8(8):7914–7922, 2014.

[22] Mohammad Heiranian, Amir Barati Farimani, and Narayana R. Aluru. Water desalination with a single-layer mos2 nanopore. *Nat Commun*, 6, 2015.

[23] J. K. Holt, H. G. Park, Y. M. Wang, M. Stadermann, A. B. Artyukhin, C. P. Grigoropoulos, A. Noy, and O. Bakajin. Fast mass transport through sub-2-nanometer carbon nanotubes. *Science*, 312(5776):1034–1037, 2006.

[24] S. Joseph and N. R. Aluru. Why are carbon nanotubes fast transporters of water? *Nano Lett*, 8(2):452–458, 2008.

[25] S. Joseph and N. R. Aluru. Pumping of confined water in carbon nanotubes by rotation-translation coupling. *Physical Review Letters*, 101(6):064502, 2008.

[26] Kei Kurotobi and Yasujiro Murata. A single molecule of water encapsulated in fullerene c-60. *Science*, 333(6042):613–616, 2011.

[27] A. Barati Farimani, Yanbin Wu, and N. R. Aluru. Rotational motion of a single water molecule in a buckyball. *Physical Chemistry Chemical Physics*, 15(41):17993–8000, 2013.

[28] Kevin T. He, Joshua D. Wood, Gregory P. Doidge, Eric Pop, and Joseph W. Lyding. Scanning tunneling microscopy study and nanomanipulation of graphene-coated water on mica. *Nano Lett.*, 12(6):2665–2672, 2012.

[29] Myung E. Suk and N. R. Aluru. Water transport through ultrathin graphene. *The Journal of Physical Chemistry Letters*, 1(10):1590–1594, 2010.

[30] David Cohen-Tanugi and Jeffrey C. Grossman. Water desalination across nanoporous graphene. *Nano Letters*, 12(7):3602–3608, 2012.

[31] Evelyn N. Wang and Rohit Karnik. Water desalination: Graphene cleans up water. *Nat Nano*, 7(9):552–554, 2012.

[32] Mi-Sun Lee, Kyongsoo Lee, So-Yun Kim, Heejoo Lee, Jihun Park, Kwang-Hyuk Choi, Han-Ki Kim, Dae-Gon Kim, Dae-Young Lee, SungWoo Nam, and Jang-Ung Park. High-performance, transparent, and stretchable electrodes using graphenemetal nanowire hybrid structures. *Nano Letters*, 13(6):2814–2821, 2013.

[33] Seung Kyu Min, Woo Youn Kim, Yeonchoo Cho, and Kwang S. Kim. Fast dna sequencing with a graphene-based nanochannel device. *Nat Nano*, 6(3):162–165, 2011.

[34] Deblina Sarkar, Wei Liu, Xuejun Xie, Aaron C. Anselmo, Samir Mitragotri, and Kaustav Banerjee. Mos2 field-effect transistor for next-generation label-free biosensors. *ACS Nano*, 8(4):3992–4003, 2014.

[35] Xing Chen, Peng Wu, Michael Rousseas, David Okawa, Zev Gartner, Alex Zettl, and Carolyn R. Bertozzi. Boron nitride nanotubes are noncytotoxic and can be functionalized for interaction with proteins and cells. *Journal of the American Chemical Society*, 131(3):890–891, 2009.

[36] X. Blase, A. Rubio, S. G. Louie, and M. L. Cohen. Stability and band-gap constancy of boron-nitride nanotubes. *Europhysics Letters*, 28(5):335–340, 1994.

[37] C. Y. Zhi, Y. Bando, C. C. Tang, and D. Golberg. Boron nitride nanotubes. *Materials Science and Engineering R-Reports*, 70(3-6):92–111, 2010.

[38] Alessandro Siria, Philippe Poncharal, Anne Laure Biance, Remy Fulcrand, Xavier Blase, Stephen T. Purcell, and Lyderic Bocquet. Giant osmotic energy conversion measured in a single transmembrane boron nitride nanotube. *Nature*, 494(7438):455–458, 2013.

[39] G. Hummer, J.C. Rasaiah, and J.P. Noworyta. Water conduction through the hydrophobic channel of a carbon nanotube. *Nature*, 414(6860):188–190, 2001.

[40] Chang Y. Won and N. R. Aluru. A chloride ion-selective boron nitride nanotube. *Chemical Physics Letters*, 478(4-6):185–190, 2009.

[41] T. A. Hilder, D. Gordon, and S. H. Chung. Salt rejection and water transport through boron nitride nanotubes. *Small*, 5(19):2183–2190, 2009.

[42] Jafar Azamat, Alireza Khataee, and Sang Woo Joo. Removal of heavy metals from water through armchair carbon and boron nitride nanotubes: a computer simulation study. *RSC Advances*, 5(32):25097–25104, 2015.

[43] Chang Y. Won and N. R. Aluru. Structure and dynamics of water confined in a boron nitride nanotube. *Journal of Physical Chemistry C*, 112(6):1812–1818, 2008.

[44] A. Waghe, J.C. Rasaiah, and G. Hummer. Filling and emptying kinetics of carbon nanotubes in water. *J. Chem. Phys.*, 117:10789–10795, 2002.

[45] C. Y. Won, S. Joseph, and N. R. Aluru. Effect of quantum partial charges on the structure and dynamics of water in single-walled carbon nanotubes. *J. Chem. Phys.*, 125(11):114701, 2006.

[46] W. H. Noon, K. D. Ausman, R. E. Smalley, and J. P. Ma. Helical ice-sheets inside carbon nanotubes in the physiological condition. *Chem. Phys. Lett.*, 355(5-6):445–448, 2002.

[47] M. C. Gordillo and J. Martí. Hydrogen bond structure of liquid water confined in nanotubes. *Chem. Phys. Lett.*, 329(5-6):341–345, 2000.

[48] G. Scocchi, D. Sergi, C. D'Angelo, and A. Ortona. Wetting and contact-line effects for spherical and cylindrical droplets on graphene layers: A comparative molecular-dynamics investigation. *Phys. Rev. E*, 84(6), 2011.

[49] Nikola Marković, Patrik U. Andersson, Mats B. Någård, and Jan B. C. Pettersson. Scattering of water from graphite: Simulations and experiments. *Chem. Phys.*, 247(3):413–430, 1999.

[50] R. Bukowski, K. Szalewicz, G.C. Groenenboom, and A. van der Avoird. Predictions of the properties of water from first principles. *Science*, 315(5816):1249, 2007.

[51] T.A. Pascal, N. Karasawa, and W.A. Goddard III. Quantum mechanics based force field for carbon (qmff-cx) validated to reproduce the mechanical and thermodynamics properties of graphite. *J. Chem. Phys.*, 133:134114, 2010.

[52] S.W. Chiu, S.A. Pandit, HL Scott, and E. Jakobsson. An improved united atom force field for simulation of mixed lipid bilayers. *J. Phys. Chem. B*, 113(9):2748–2763, 2009.

[53] Miguel A. Morales, John R. Gergely, Jeremy McMinis, Jeffrey M. McMahon, Jeongnim Kim, and David M. Ceperley. Quantum monte carlo benchmark of exchange-correlation functionals for bulk water. *Journal of Chemical Theory and Computation*, 10(6):2355–2362, 2014.

[54] Matus Dubecky, Rene Derian, Petr Jurecka, Lubos Mitas, Pavel Hobza, and Michal Otyepka. Quantum monte carlo for noncovalent interactions: An efficient protocol attaining benchmark accuracy. *Physical Chemistry Chemical Physics*, 16(38):20915–23, 2014.

[55] J. Ma, A. Michaelides, D. Alfè, L. Schimka, G. Kresse, and E. Wang. Adsorption and diffusion of water on graphene from first principles. *Physical Review B*, 84(3):033402, 2011.

[56] Hsing Cheng-Rong, Cheng Ching, Chou Jyh-Pin, Chang Chun-Ming, and Wei Ching-Ming. Van der waals interaction in a boron nitride bilayer. *New Journal of Physics*, 16(11):113015, 2014.

[57] Judith Harl and Georg Kresse. Accurate bulk properties from approximate many-body techniques. *Physical Review Letters*, 103(5):056401, 2009.

[58] S. Lebègue, J. Harl, Tim Gould, J. G. Ángyán, G. Kresse, and J. F. Dobson. Cohesive properties and asymptotics of the dispersion interaction in graphite by the random phase approximation. *Physical Review Letters*, 105(19):196401, 2010.

[59] Lucas K. Wagner and Lubos Mitas. Energetics and dipole moment of transition metal monoxides by quantum monte carlo. *Journal of Chemical Physics*, 126(3):034105, 2007.

[60] C. J. Umrigar, K. G. Wilson, and J. W. Wilkins. Optimized trial wave-functions for quantum monte-carlo calculations. *Physical Review Letters*, 60(17):1719–1722, 1988.

[61] O. Gunnarsson and B. I. Lundqvist. Exchange and correlation in atoms, molecules, and solids by the spin-density-functional formalism. *Physical Review B*, 13(10):4274–4298, 1976. PRB.

[62] David C. Langreth and John P. Perdew. Exchange-correlation energy of a metallic surface: Wave-vector analysis. *Physical Review B*, 15(6):2884–2901, 1977. PRB.

[63] J. P. Perdew, K. Burke, and M. Ernzerhof. Generalized gradient approximation made simple. *Physical Review Letters*, 77(18):3865–3868, 1996.

[64] Berk Hess, Carsten Kutzner, David van der Spoel, and Erik Lindahl. Gromacs 4: algorithms for highly efficient, load-balanced, and scalable molecular simulation. *Journal of Chemical Theory and Computation*, 4(3):435–447, 2008.

[65] R. W. Hockney, S. P. Goel, and J. W. Eastwood. Quiet high-resolution computer models of a plasma. *Journal of Computational Physics*, 14(2):148–158, 1974.

[66] S. Nos. A unified formulation of the constant temperature molecular-dynamics methods. *Journal of Chemical Physics*, 81(1):511–519, 1984.

[67] William G. Hoover. Canonical dynamics: Equilibrium phase-space distributions. *Physical Review A*, 31(3):1695–1697, 1985.

[68] S. J. Stuart, A. B. Tutein, and J. A. Harrison. A reactive potential for hydrocarbons with intermolecular interactions. *J. Chem. Phys.*, 112(14):6472–6486, 2000.

[69] H.J.C. Berendsen, J.R. Grigera, and T.P. Straatsma. The missing term in effective pair potentials. *J. Phys. Chem.*, 91(24):6269–6271, 1987.

[70] S. Plimpton. Fast parallel algorithms for short-range molecular-dynamics. *Journal of Computational Physics*, 117(1):1–19, 1995.

[71] L. Verlet. Computer experiments on classical fluids. i. thermodynamical properties of lennard-jones molecules. *Physical Review*, 159(1):98–103, 1967.

[72] S. Nosé. A molecular dynamics method for simulations in the canonical ensemble. *Mol. Phys.*, 100(1):191–198, 2002.

[73] William G. Hoover. Canonical dynamics: Equilibrium phase-space distributions. *Phys. Rev. A*, 31(3):1695–1697, Mar 1985.

[74] M. Parrinello and A. Rahman. Polymorphic transitions in single crystals: A new molecular dynamics method. *J. Appl. Phys.*, 52(12):7182–7190, 1981.

[75] MJ Longhurst and N. Quirke. The environmental effect on the radial breathing mode of carbon nanotubes in water. *J. Chem. Phys.*, 124:234708, 2006.

[76] MJ Longhurst and N. Quirke. The environmental effect on the radial breathing mode of carbon nanotubes. ii. shell model approximation for internally and externally adsorbed fluids. *J. Chem. Phys.*, 125:184705, 2006.

[77] A. Pertsin and M. Grunze. Water-graphite interaction and behavior of water near the graphite surface. *J. Phys. Chem. B*, 108(4):1357–1364, 2004.

[78] A. Pertsin and M. Grunze. Water as a lubricant for graphite: A computer simulation study. *J. Chem. Phys.*, 125:114707, 2006.

[79] H. Sun. Compass: An ab initio force-field optimized for condensed-phase applications-overview with details on alkane and benzene compounds. *J. Phys. Chem. B*, 102(38):7338–7364, 1998.

[80] J. R. Maple, U. Dinur, and A. T. Hagler. Derivation of force-fields for molecular mechanics and dynamics from ab initio energy surfaces. *Proc. Natl. Acad. Sci.*, 85(15):5350–5354, 1988.

[81] Hendrik Heinz, R. A. Vaia, B. L. Farmer, and R. R. Naik. Accurate simulation of surfaces and interfaces of face-centered cubic metals using 12-6 and 9-6 lennard-jones potentials. *J. Phys. Chem. C*, 112(44):17281–17290, 2008.

[82] B. R. Brooks, R. E. Bruccoleri, B. D. Olafson, D. J. States, S. Swaminathan, and M. Karplus. Charmm - a program for macromolecular energy, minimization, and dynamics calculations. *J. Comput. Chem.*, 4(2):187–217, 1983.

[83] W. D. Cornell, P. Cieplak, C. I. Bayly, I. R. Gould, K. M. Merz, D. M. Ferguson, D. C. Spellmeyer, T. Fox, J. W. Caldwell, and P. A. Kollman. A 2nd generation force-field for the simulation of proteins, nucleic-acids, and organic-molecules. *J. Am. Chem. Soc.*, 117(19):5179–5197, 1995.

[84] William L. Jorgensen, David S. Maxwell, and Julian Tirado-Rives. Development and testing of the opls all-atom force field on conformational energetics and properties of organic liquids. *J. Am. Chem. Soc.*, 118(45):11225–11236, 1996.

[85] WF van Gunsteren, SR Billeter, AA Eising, PH Hnenberger, P. Krger, AE Mark, WRP Scott, and IG Tironi. *The GROMOS Manual and User Guide*. vdf Hochschulverlag AG, Zürich, Switzerland, 1996.

[86] Yanbin Wu, S. Joseph, and N. R. Aluru. Effect of cross-linking on the diffusion of water, ions, and small molecules in hydrogels. *J Phys Chem B*, 113(11):3512–20, 2009.

[87] J.R. Taylor. *An Introduction to Error Analysis: the Study of Uncertainties in Physical Measurements*. University Science Books, 1997.

[88] F. Y. Hansen and L. W. Bruch. Molecular-dynamics study of the dynamical excitations in commensurate monolayer films of nitrogen molecules on graphite: A test of the corrugation in the nitrogen-graphite potential. *Physical Review B*, 51(4):2515–2536, 1995.

[89] R. A. Kendall, T. H. Dunning, and R. J. Harrison. Electron-affinities of the 1st-row atoms revisited - systematic basis-sets and wave-functions. *Journal of Chemical Physics*, 96(9):6796–6806, 1992.

[90] W. S. Benedict, N. Gailar, and E. K. Plyler. Rotation-vibration spectra of deuterated water vapor. *Journal of Chemical Physics*, 24(6):1139–1165, 1956.

[91] D. Pacilé, J. C. Meyer, Ç. Ö. Girit, and A. Zettl. The two-dimensional phase of boron nitride: Few-atomic-layer sheets and suspended membranes. *Applied Physics Letters*, 92(13):133107, 2008.

[92] M. J. Frisch, G. W. Trucks, H. B. Schlegel, G. E. Scuseria, M. A. Robb, J. R. Cheeseman, J. A. Montgomery, Jr., T. Vreven, K. N. Kudin, J. C. Burant, J. M. Millam, S. S. Iyengar, J. Tomasi, V. Barone, B. Mennucci, M. Cossi, G. Scalmani, N. Rega, G. A. Petersson, H. Nakatsuji, M. Hada, M. Ehara, K. Toyota, R. Fukuda, J. Hasegawa, M. Ishida, T. Nakajima, Y. Honda, O. Kitao, H. Nakai, M. Klene, X. Li, J. E. Knox, H. P. Hratchian, J. B. Cross, V. Bakken, C. Adamo, J. Jaramillo, R. Gomperts, R. E. Stratmann, O. Yazyev, A. J. Austin, R. Cammi, C. Pomelli, J. W. Ochterski, P. Y. Ayala, K. Morokuma, G. A. Voth, P. Salvador, J. J. Dannenberg, V. G. Zakrzewski, S. Dapprich, A. D. Daniels, M. C. Strain, O. Farkas, D. K. Malick, A. D. Rabuck, K. Raghavachari, J. B. Foresman, J. V. Ortiz, Q. Cui, A. G. Baboul, S. Clifford, J. Cioslowski, B. B. Stefanov, G. Liu, A. Liashenko, P. Piskorz, I. Komaromi, R. L. Martin, D. J. Fox, T. Keith, M. A. Al-Laham, C. Y. Peng, A. Nanayakkara, M. Challacombe, P. M. W. Gill, B. Johnson, W. Chen, M. W. Wong, C. Gonzalez, and J. A. Pople. Gaussian 03, revision c.02. *Gaussian, Inc., Wallingford, CT*, 2004.

[93] P. Jurečka, J. Šponer, J. Černy, and P. Hobza. Benchmark database of accurate (mp2 and ccsd(t) complete basis set limit) interaction energies of small model complexes, dna base pairs, and amino acid pairs. *Phys. Chem. Chem. Phys.*, 8(17):1985–93, 2006.

[94] Asger Halkier, Trygve Helgaker, Poul Jørgensen, Wim Klopper, and Jeppe Olsen. Basis-set convergence of the energy in molecular hartreefock calculations. *Chemical Physics Letters*, 302(5-6):437–446, 1999.

[95] Petr Jurečka and Pavel Hobza. On the convergence of the (deccsd(t)-demp2) term for complexes with multiple h-bonds. *Chem. Phys. Lett.*, 365(1-2):89–94, 2002.

[96] R Dovesi, VR Saunders, C Roetti, R Orlando, CM Zicovich-Wilson, F Pascale, B Civalleri, K Doll, NM Harrison, and IJ Bush. Crystal09 users manual (university of torino, torino), 2009.

[97] M. Burkatzki, C. Filippi, and M. Dolg. Energy-consistent pseudopotentials for quantum monte carlo calculations. *Journal of Chemical Physics*, 126(23):234105, 2007.

[98] F. R. Petruzielo, Julien Toulouse, and C. J. Umrigar. Basis set construction for molecular electronic structure theory: Natural orbital and gauss-slater basis for smooth pseudopotentials. *Journal of Chemical Physics*, 134(6):064104, 2011.

[99] Lucas K. Wagner, Michal Bajdich, and Lubos Mitas. Qwalk: A quantum monte carlo program for electronic structure. *Journal of Computational Physics*, 228(9):3390–3404, 2009.

[100] G. Kresse and J. Hafner. *Ab initio* molecular dynamics for open-shell transition metals. *Physical Review B*, 48(17):13115–13118, 1993.

[101] G. Kresse and J. Furthmller. Efficiency of ab-initio total energy calculations for metals and semiconductors using a plane-wave basis set. *Computational Materials Science*, 6(1):15–50, 1996.

[102] Hendrik J. Monkhorst and James D. Pack. Special points for brillouin-zone integrations. *Physical Review B*, 13(12):5188–5192, 1976.

[103] J. Grant Hill and James A. Platts. Spin-component scaling methods for weak and stacking interactions. *Journal of Chemical Theory and Computation*, 3(1):80–85, 2007.

[104] Michael J. Frisch, G. W. Trucks, H. Bernhard Schlegel, Gustavo E. Scuseria, Michael A. Robb, James R. Cheeseman, Giovanni Scalmani, Vincenzo Barone, Benedetta Mennucci, G. A. Petersson, H. Nakatsuji, M. Caricato, Xiaosong Li, H. P. Hratchian, Artur F. Izmaylov, Julien Bloino, G. Zheng, J. L. Sonnenberg, M. Hada, M. Ehara, K. Toyota, R. Fukuda, J. Hasegawa, M. Ishida, T. Nakajima, Y. Honda, O. Kitao, H. Nakai, T. Vreven, J. A. Montgomery Jr., J. E. Peralta, François Ogliaro, Michael J. Bearpark, Jochen Heyd, E. N. Brothers, K. N. Kudin, V. N. Staroverov, Rika Kobayashi, J. Normand, Krishnan Raghavachari, Alistair P. Rendell, J. C. Burant, S. S. Iyengar, Jacopo Tomasi, M. Cossi, N. Rega, N. J. Millam, M. Klene, J. E. Knox, J. B. Cross, V. Bakken, C. Adamo, J. Jaramillo, R. Gomperts, R. E. Stratmann, O. Yazyev, A. J. Austin, R. Cammi, C. Pomelli, J. W. Ochterski, R. L. Martin, K. Morokuma, V. G. Zakrzewski, G. A. Voth, P. Salvador, J. J. Dannenberg, S. Dapprich, A. D. Daniels, Ödön Farkas, J. B. Foresman, J. V. Ortiz, J. Cioslowski, and Douglas J. Fox. Gaussian 09, 2009.

[105] Anthony J. Stone. Distributed multipole analysis: Stability for large basis sets. *Journal of Chemical Theory and Computation*, 1(6):1128–1132, 2005.

[106] L. X. Dang and T. M. Chang. Molecular dynamics study of water clusters, liquid, and liquid-vapor interface of water with many-body potentials. *Journal of Chemical Physics*, 106(19):8149–8159, 1997.

[107] S. Murad and K. E. Gubbins. Molecular-dynamics simulation of methane using a singularity-free algorithm. *Abstracts of Papers of the American Chemical Society*, 175(MAR):3–3, 1978.

[108] A. Cheng and W. A. Steele. Computer-simulation of ammonia on graphite .1. low-temperature structure of monolayer and bilayer films. *Journal of Chemical Physics*, 92(6):3858–3866, 1990.

[109] D. Bedrov and G. D. Smith. Molecular dynamics simulations of 1,2-dimethoxyethane in aqueous solution: Influence of the water potential. *Journal of Physical Chemistry B*, 103(18):3791–3796, 1999.

[110] Yanbin Wu and N. R. Aluru. Graphitic carbonwater nonbonded interaction parameters. *The Journal of Physical Chemistry B*, 117(29):8802–8813, 2013.

[111] W. L. Jorgensen, J. Chandrasekhar, J. D. Madura, R. W. Impey, and M. L. Klein. Comparison of simple potential functions for simulating liquid water. *Journal of Chemical Physics*, 79(2):926–935, 1983.

[112] See `https://github.com/wuyb02/ff-bn-w` for example files for using the parameters in the GROMACS and LAMMPS packages.

[113] Frédéric Leroy, Shengyuan Liu, and Jianguo Zhang. Parameterizing non-bonded interactions from wetting experiments via the work of adhesion: The example of water on graphene surfaces. *The Journal of Physical Chemistry C*, 2015.

[114] C. Vega and E. de Miguel. Surface tension of the most popular models of water by using the test-area simulation method. *The Journal of Chemical Physics*, 126(15):154707, 2007.

[115] H. J. C. Berendsen, J. R. Grigera, and T. P. Straatsma. The missing term in effective pair potentials. *The Journal of Physical Chemistry*, 91(24):6269–6271, 1987.

[116] Michael W. Mahoney and William L. Jorgensen. A five-site model for liquid water and the reproduction of the density anomaly by rigid, nonpolarizable potential functions. *J Chem Phys*, 112(20):8910, 2000.

[117] Ludmila B. Boinovich, Alexandre M. Emelyanenko, Andrei S. Pashinin, Chee Huei Lee, Jaroslaw Drelich, and Yoke Khin Yap. Origins of thermodynamically stable superhydrophobicity of boron nitride nanotubes coatings. *Langmuir*, 28(2):1206–1216, 2011.

[118] Chee Huei Lee, Jaroslaw Drelich, and Yoke Khin Yap. Superhydrophobicity of boron nitride nanotubes grown on silicon substrates. *Langmuir*, 25(9):4853–4860, 2009.

[119] Jie Yu, Li Qin, Yufeng Hao, Shengyong Kuang, Xuedong Bai, Yat-Ming Chong, Wenjun Zhang, and Enge Wang. Vertically aligned boron nitride nanosheets: Chemical vapor synthesis, ultraviolet light emission, and superhydrophobicity. *ACS Nano*, 4(1):414–422, 2010.

[120] R. Bukowski, K. Szalewicz, G. C. Groenenboom, and A. van der Avoird. Predictions of the properties of water from first principles. *Science*, 315(5816):1249–52, 2007.

[121] R. Weast, M. Astle, and W. Beyer. *CRC Handbook of Chemistry and Physics*, volume 69. CRC Press: Boca Raton, FL, 1988.

[122] David Feller and K. D. Jordan. Estimating the strength of the water/single-layer graphite interaction. *The Journal of Physical Chemistry A*, 104(44):9971–9975, 2000.

[123] Glen R. Jenness and Kenneth D. Jordan. Df-dft-sapt investigation of the interaction of a water molecule to coronene and dodecabenzocoronene: Implications for the water-graphite interaction. *J. Phys. Chem. C*, 113(23):10242–10248, 2009.

[124] R.C. Weast, M.J. Astle, and W.H. Beyer. *CRC Handbook of Chemistry and Physics*, volume 69. CRC press Boca Raton, FL, 1988.

[125] Miroslav Ruběs, Petr Nachtigall, Jir?i? Vondrášek, and Ota Bludský. Structure and stability of the water?graphite complexes. *The Journal of Physical Chemistry C*, 113(19):8412–8419, 2009.

[126] E. Voloshina, D. Usvyat, M. Schütz, Y. Dedkov, and B. Paulus. On the physisorption of water on graphene: a ccsd(t) study. *Phys. Chem. Chem. Phys.*, 13(25):12041–7, 2011.

[127] V. Kairys and J. H. Jensen. Evaluation of the charge penetration energy between non-orthogonal molecular orbitals using the spherical gaussian overlap approximation. *Chem. Phys. Lett.*, 315(1-2):140–144, 1999.

[128] Patric Schyman and William L. Jorgensen. Exploring adsorption of water and ions on carbon surfaces using a polarizable force field. *J Phys. Chem. Lett.*, 4(3):468–474, 2013.

[129] E. Neria, S. Fischer, and M. Karplus. Simulation of activation free energies in molecular systems. *J. Chem. Phys.*, 105(5):1902–1921, 1996.

[130] G. Cicero, J. C. Grossman, E. Schwegler, F. Gygi, and G. Galli. Water confined in nanotubes and between graphene sheets: A first principle study. *J. Am. Chem. Soc.*, 130(6):1871–8, 2008.

[131] M. Kaukonen, A. Gulans, P. Havu, and E. Kauppinen. Lennard-jones parameters for small diameter carbon nanotubes and water for molecular mechanics simulations from van der waals density functional calculations. *J. Comput. Chem.*, 33(6):652–658, 2012.

[132] Mathias Lundgren, Neil L. Allan, Terence Cosgrove, and Neil George. Wetting of water and water/ethanol droplets on a non-polar surface: A molecular dynamics study. *Langmuir*, 18(26):10462–10466, 2002.

[133] F. Leroy and F. Müller-Plathe. Solid-liquid surface free energy of lennard-jones liquid on smooth and rough surfaces computed by molecular dynamics using the phantom-wall method. *J. Chem. Phys.*, 133:044110, 2010.

[134] C. Sendner, D. Horinek, L. Bocquet, and R. R. Netz. Interfacial water at hydrophobic and hydrophilic surfaces: Slip, viscosity, and diffusion. *Langmuir*, 25(18):10768–10781, 2009.

[135] J. Y. Wang, S. Betelu, and B. M. Law. Line tension approaching a first-order wetting transition: Experimental results from contact angle measurements. *Phys. Rev. E*, 63(3), 2001.

[136] Ronen Zangi and B. J. Berne. Temperature dependence of dimerization and dewetting of large-scale hydrophobes: A molecular dynamics study. *J. Phys. Chem. B*, 112(29):8634–8644, 2008.

[137] E. R. Cruz-Chu, A. Aksimentiev, and K. Schulten. Water-silica force field for simulating nanodevices. *J. Phys. Chem. B*, 110(43):21497–21508, 2006.

[138] J. I. Siepmann, S. Karaborni, and B. Smit. Simulating the critical-behavior of complex fluids. *Nature*, 365(6444):330–332, 1993.

[139] R. A. Jishi, L. Venkataraman, M. S. Dresselhaus, and G. Dresselhaus. Phonon modes in carbon nanotubules. *Chem. Phys. Lett.*, 209(1-2):77–82, 1993.

[140] S. Bandow, S. Asaka, Y. Saito, A. M. Rao, L. Grigorian, E. Richter, and P. C. Eklund. Effect of the growth temperature on the diameter distribution and chirality of single-wall carbon nanotubes. *Phys. Rev. Lett.*, 80(17):3779–3782, 1998.

[141] S. M. Bachilo, M. S. Strano, C. Kittrell, R. H. Hauge, R. E. Smalley, and R. B. Weisman. Structure-assigned optical spectra of single-walled carbon nanotubes. *Science*, 298(5602):2361–2366, 2002.

[142] Tao Liang, Simon R. Phillpot, and Susan B. Sinnott. Parametrization of a reactive many-body potential for mo-s systems. *Physical Review B*, 79(24), 2009.

[143] Andrew Kozbial, Xiao Gong, Haitao Liu, and Lei Li. Understanding the intrinsic water wettability of molybdenum disulfide (mos2). *Langmuir*, 31(30):8429–8435, 2015.

[144] Philippe K. Chow, Eklavya Singh, Bartolomeu Cruz Viana, Jian Gao, Jian Luo, Jing Li, Zhong Lin, Ana L. Elas, Yunfeng Shi, Zuankai Wang, Mauricio Terrones, and Nikhil Koratkar. Wetting of mono and few-layered ws2 and mos2 films supported on si/sio2 substrates. *ACS Nano*, 9(3):3023–3031, 2015.

[145] P. Navabpour, D. G. Teer, D. J. Hitt, and M. Gilbert. Evaluation of non-stick properties of magnetron-sputtered coatings for moulds used for the processing of polymers. *Surface and Coatings Technology*, 201(6):3802–3809, 2006.

[146] S. Zhang, X. T. Zeng, Z. G. Tang, and M. J. Tan. Exploring the antisticking properties of solid lubricant thin films in transfer molding. *International Journal of Modern Physics B*, 16(6-7):1080–1085, 2002.

[147] Udayabagya Halim, Chu Ran Zheng, Yu Chen, Zhaoyang Lin, Shan Jiang, Rui Cheng, Yu Huang, and Xiangfeng Duan. A rational design of cosolvent exfoliation of layered materials by directly probing liquid-solid interaction. *Nature Communications*, 4, 2013.

[148] Huogui Yu, Ping Hu, Ting Shang, Ming Jiang, and Qian Chen. Phase representation and property determination of raw materials of solid lubricant. *Journal of Wuhan University of Technology-Mater. Sci. Ed.*, 23(1):130–133, 2008.

[149] Anand P. S. Gaur, Satyaprakash Sahoo, Majid Ahmadi, Saroj P. Dash, Maxime J. F. Guinel, and Ram S. Katiyar. Surface energy engineering for tunable wettability through controlled synthesis of mos2. *Nano Letters*, 14(8):4314–4321, 2014.

[150] Yanbin Wu, Lucas K. Wagner, and Narayana R. Aluru. Hexagonal boron nitride and water interaction parameters. *The Journal of Chemical Physics*, 144(16):164118, 2016.

[151] M. Schluter, M. Lannoo, M. Needels, G. Baraff, and D. Tomnek. Electron-phonon coupling and superconductivity in alkali-intercalated c60 solid. *Phys. Rev. Lett.*, 68(4):526–529, 1992.

[152] W.A. ISteele. *The interaction of gases with solid surfaces*. Pergamon Press, Oxford, UK, 1974.

[153] J. Martí, E. Guàrdia, and J. A. Padró. Dielectric-properties and infrared-spectra of liquid water - influence of the dynamic cross correlations. *Journal of Chemical Physics*, 101(12):10883–10891, 1994.

[154] Mary J. Bojan and William A. Steele. Interactions of diatomic molecules with graphite. *Langmuir*, 3(6):1123–1127, 1987.

[155] Stephen L. Mayo, Barry D. Olafson, and William A. Goddard. Dreiding: a generic force field for molecular simulations. *The Journal of Physical Chemistry*, 94(26):8897–8909, 1990.

[156] J A Stewart and D E Spearot. Atomistic simulations of nanoindentation on the basal plane of crystalline molybdenum disulfide (mos 2). *Modelling and Simulation in Materials Science and Engineering*, 21(4):045003, 2013.